



National Library  
of Canada

Bibliothèque nationale  
du Canada

Canadian Theses Service

Services des thèses canadiennes

Ottawa, Canada  
K1A 0N4

## CANADIAN THESES

## THÈSES CANADIENNES

### NOTICE

The quality of this microfiche is heavily dependent upon the quality of the original thesis submitted for microfilming. Every effort has been made to ensure the highest quality of reproduction possible.

If pages are missing, contact the university which granted the degree.

Some pages may have indistinct print especially if the original pages were typed with a poor typewriter ribbon or if the university sent us an inferior photocopy.

Previously copyrighted materials (journal articles, published tests, etc.) are not filmed.

Reproduction in full or in part of this film is governed by the Canadian Copyright Act, R.S.C. 1970, c. C-30. Please read the authorization forms which accompany this thesis.

THIS DISSERTATION  
HAS BEEN MICROFILMED  
EXACTLY AS RECEIVED

### AVIS

La qualité de cette microfiche dépend grandement de la qualité de la thèse soumise au microfilmage. Nous avons tout fait pour assurer une qualité supérieure de reproduction.

S'il manque des pages, veuillez communiquer avec l'université qui a conféré le grade.

La qualité d'impression de certaines pages peut laisser à désirer, surtout si les pages originales ont été dactylographiées à l'aide d'un ruban usé ou si l'université nous a fait parvenir une photocopie de qualité inférieure.

Les documents qui font déjà l'objet d'un droit d'auteur (articles de revue, examens publiés, etc.) ne sont pas microfilmés.

La reproduction, même partielle, de ce microfilm est soumise à la Loi canadienne sur le droit d'auteur, SRC 1970, c. C-30. Veuillez prendre connaissance des formules d'autorisation qui accompagnent cette thèse.

LA THÈSE A ÉTÉ  
MICROFILMÉE TELLE QUE  
NOUS L'AVONS REÇUE

INFLUENCE OF PRESSURE ON THE CYCLOTRON MASS  
OF POTASSIUM AND HOLE FERMI SURFACE OF ANTIMONY

By

AFAF ABD EL-RAHMAN, M.Sc.

A Thesis

Submitted to the School of Graduate Studies

in Partial Fulfilment of the Requirements

for the Degree

Doctor of Philosophy

McMaster University

April 1985



DOCTOR OF PHILOSOPHY (1985)  
(Physics)

McMASTER UNIVERSITY  
Hamilton, Ontario

TITLE: Influence of Pressure on the Cyclotron Mass of Potassium  
and Hole Fermi Surface of Antimony

AUTHOR: Afaf Abd El-Rahman, M.Sc. (Al-Azhar University, Cairo)  
M.Sc. (McMaster University)

SUPERVISOR: Professor W.R. Datars (

NUMBER OF PAGES: xi, 125

## ABSTRACT

Detailed investigations of the hydrostatic pressure dependences of the hole Fermi surface of antimony and the cyclotron effective masses of antimony and potassium were made in the pressure range from 1 bar to 4.4 kbar, by means of the de Haas-van Alphen (dHvA) effect. Solid helium was used as a pressure transmitting medium. These measurements were made using the field modulation measuring technique, modified to optimize the sensitivity and selectivity of the dHvA spectrometer action. The effect of pressure on the anisotropy of the entire hole Fermi surface in the trigonal-bisectrix crystallographic plane was determined in detail. The pressure derivatives of the extremal cross-sectional areas of the surface were found to differ in sign and magnitude for various field directions. The total departure of the hole Fermi surface from a perfect ellipsoid in this crystallographic plane was accurately calculated at standard atmospheric pressure (1 bar) and at a pressure of 1.08 kbar, using the ellipsoidal-parabolic approximation. It was found that the anisotropy and shape of the surface are greatly influenced by pressure. The tilt angle was found to be insensitive to pressure within quoted experimental error.

The cyclotron effective masses were derived from the temperature dependence of the dHvA amplitude. In potassium, the logarithmic pressure derivative,  $(1/m^*)dm^*/dP$ , was found to be  $-(0.71 \pm 0.12) \times 10^{-2} \text{ kbar}^{-1}$ , and the standard atmospheric pressure cyclotron effective mass was determined

to be  $(1.211 \pm 0.005) m_0$ , where  $m_0$  is the free electron mass. The observed decrease of the quasiparticle mass with increasing pressure was analyzed and explained in terms of changes of the band structure effects and many-body effects with pressure. In antimony, the cyclotron effective mass associated with the minimum section of the hole Fermi surface was determined to be  $(0.0637 \pm 0.0005) m_0$  at standard atmospheric pressure, in agreement with the calculated band structure mass of Pospelov and Grachev of  $0.06 m_0$ . The cyclotron mass was found to be nearly insensitive to pressure with  $(1/m^*)dm^*/dP = + (0.16 \pm 0.39) \times 10^{-2} \text{ kbar}^{-1}$ . The study of the pressure dependence of  $m^*$  in these elements along with a theory proposed by Trofimenkoff and Carbotte for the pressure dependence of the electron-phonon mass enhancement parameter,  $\lambda_{ep}$ , permits the magnitudes of the changes of the band structure mass and  $\lambda_{ep}$  with pressure to be deduced in these elements.

## ACKNOWLEDGEMENTS

I wish to express my sincere appreciation to my supervisor, Dr. W.R. Datars for his encouragement, understanding, continued assistance, guidance and supervision during the course of this work. Several discussions with Dr. D.W. Taylor are gratefully acknowledged.

I acknowledge useful discussions with my former colleagues, Dr. P.G. Coulter of University of Toronto, Dr. M. Elliott of the University College of North Wales, Great Britain, and Dr. F.S. Razavi of Brock University and my present colleagues, H. Zaleski, P. Laroche, A. Weingartshofer, and J. Latkowski. Thanks to C. Verge for aid with technical details and to Mr. W. Scott for his effort in producing many litres of liquid helium.

Thanks are due to Mrs. Kennelly for her patience and efforts in the accurate typing of this thesis. Mr. George Wilton's excellent drawing is appreciated.

Financial support from the Natural Sciences and Engineering Research Council of Canada is gratefully acknowledged.

## TABLE OF CONTENTS

<u>Chapter</u>		<u>Page</u>
1	INTRODUCTION	1
2	PHYSICAL ASPECTS OF THE DE HAAS-VAN ALPHEN EFFECT	6
	1. Electrons in a uniform magnetic field	6
	2. Electronic density of states in a magnetic field and origin of the de Haas-van Alphen oscillation	13
	3. Lifshitz-Kosevich expression for the de Haas-van Alphen effect	16
3	CRYSTAL STRUCTURE AND FERMI SURFACE OF ANTIMONY	21
4	THEORY, METHODS AND APPARATUS FOR MEASURING THE DE HAAS-VAN ALPHEN EFFECT USING THE FIELD MODULATION MEASURING TECHNIQUE	30
	1. Theory of the field modulation technique	30
	2. De Haas-van Alphen experimental technique and sample preparation.	33
	2.1 Antimony	34
	2.1.a Methods of frequency distribution	34
	2.1.b Alignment and handling of sample	37
	2.1.c Detection system and generation of the modulation and dc fields	38
	2.2 Potassium	41
	2.2.a Sample preparation	41
	2.2.b Detection system and generation of the modulation and dc fields	42
	2.3 Field modulation experimental apparatus	44
	3. The solid helium high pressure technique	47
	3.1 High pressure system	47

<u>Chapter</u>		<u>Page</u>
	3.2 Method of applying hydrostatic pressure at liquid helium temperature	49
5	EXPERIMENTAL STUDIES OF THE INFLUENCE OF HYDROSTATIC PRESSURE ON THE ELECTRON CYCLOTRON EFFECTIVE MASS IN POTASSIUM	54
	1. Introduction	54
	2. Experimental results and analysis	56
	3. Discussion	60
6	EXPERIMENTAL RESULTS AND ANALYSIS OF THE PRESSURE DEPENDENCE OF THE HOLE FERMI SURFACE AND CYCLOTRON EFFECTIVE MASS OF ANTIMONY	70
	1. Pressure dependence of the hole Fermi surface	70
	2. Pressure dependence of the cyclotron effective mass	91
7	DISCUSSION: PRESSURE DEPENDENCE OF THE HOLE FERMI SURFACE AND CYCLOTRON EFFECTIVE MASS OF ANTIMONY	95
	1. Pressure dependence of the hole Fermi surface anisotropy and shape	95
	2. Pressure dependence of the minimum frequency	103
	3. Pressure dependence of the cyclotron effective mass	109
8	CONCLUSION	117
	REFERENCES	122



## LIST OF FIGURES

<u>Figure</u>	<u>Description</u>	<u>Page</u>
2-1	Quantization scheme for free electrons in a magnetic field.	12
2-2	The origin of the dHvA effect	15
3-1	The Brillouin zone of antimony	24
4-1	The geometry of the experimental arrangement for measuring the dHvA effect in antimony	36
4-2	The modulation and pick-up coils assembly for the field modulation apparatus used in detecting the dHvA effect in antimony	39
4-3	A schematic diagram of the high pressure cell and dHvA detection system	43
4-4	A schematic diagram for the field modulating measuring apparatus	46
4-5	Block diagram for the high pressure system	48
4-6	A schematic diagram of the high pressure electrical feedthrough and dHvA pick-up coil assembly	50
4-7	Pressure-temperature diagram for He <sup>4</sup>	52
5-1	Logarithmic plot for the determination of the cyclotron effective mass in potassium	58
5-2	A plot of the cyclotron effective mass of potassium <u>versus</u> pressure up to 4.4 kbar	59
5-3	A plot of the measured and calculated cyclotron effective mass normalized to its value at standard atmospheric pressure <u>versus</u> pressure up to 4.4 kbar in potassium.	67
6-1	A recorder trace of the quantum oscillation of the dHvA effect, associated with the hole branch, as a function of the direction of the magnetic field as it was rotated in the trigonal-bisectrix plane of antimony	72

<u>Figure</u>	<u>Description</u>	<u>Page</u>
6-2	A recorder trace of the dHvA oscillation associated with the minimum section of the hole Fermi surface <u>versus</u> magnetic field strength	74
6-3	A plot of the number of the dHvA oscillations <u>versus</u> the reciprocal of magnetic field strength along the minimum section of the hole Fermi surface	75
6-4	A plot of the angular dependences of the dHvA frequencies of the hole branch in the trigonal-bisectrix plane at pressures of 1 bar and 1.08 kbar	78
6-5	A plot of the angular dependences of the dHvA frequencies of the hole branch in the trigonal-bisectrix plane at pressures of 1 bar and 3.89 kbar	79
6-6	A plot of the angular dependences of the rate of change of the extremal frequencies of the hole branch in the trigonal-bisectrix plane at a pressure of 1.08 kbar	81
6-7	A plot of the angular dependences of the rate of change of the extremal frequencies of the hole branch in the trigonal-bisectrix plane at a pressure of 2.44 kbar	82
6-8	A plot of the angular dependences of the rate of change of the extremal frequencies of the hole branch in the trigonal-bisectrix plane at pressures of 3.15 and 3.56 kbar	83
6-9	A plot of the angular dependences of the rate of change of the extremal frequencies of the principal hole branch in the trigonal-bisectrix plane at pressures of 3.89 and 4.19 kbar	84
6-10	A plot of the tilt angle of the hole branch in the trigonal-bisectrix plane <u>versus</u> pressure up to 4.5 kbar	86
6-11	A plot of the minimum frequency of the hole branch <u>versus</u> pressure up to 4.3 kbar	88
6-12	A plot of the dHvA frequency at $11^{\circ}$ from the maximum of the hole branch in the trigonal-bisectrix plane <u>versus</u> pressure	90

<u>Figure</u>	<u>Description</u>	<u>Page</u>
6-13	Logarithmic plots for the determination of the cyclotron effective mass in antimony	93
6-14	A plot of the cyclotron effective mass of antimony <u>versus</u> pressure up to 3.7 kbar	94
7-1	Influence of pressure on the deviation of the observed frequencies of the hole branch from an ellipsoidal model.	98

## LIST OF TABLES

<u>Table</u>	<u>Description</u>	<u>Page</u>
3-1	Crystal structure parameters for arsenic, antimony and bismuth	23
5-1	Reported values of the electron cyclotron effective mass of potassium at standard atmospheric pressure	61
5-2	Calculated pressure dependences of $\Delta V/V_0$ , $\lambda_G$ and $\lambda_{ep}$	66
6-1	Absolute and relative frequency measurements of the principal hole branch at various angles in the trigonal-bisectrix plane at pressures of 1 bar and 1.08 kbar	77
7-1	Calculated values of $(\pi^2 S / 2\pi m^*)$	101
7-2	Summary of results of the pressure dependence of the anisotropy of the hole Fermi surface in the trigonal-bisectrix plane of antimony	104
7-3	Comparison of the reported values of the pressure derivative of the minimum frequency $(1/F)dF/dP$ , of the hole Fermi surface in the trigonal-bisectrix plane of antimony	107
7-4	Calculated values of the pressure dependence of the hole Fermi energy based on the ellipsoidal-parabolic approximation	110
7-5	Reported values of the calculated and experimental cyclotron effective mass associated with the minimum section of the hole Fermi surface of antimony in the trigonal-bisectrix plane at standard atmospheric pressure	111

## CHAPTER 1

### INTRODUCTION

The de Haas-van Alphen effect (hereafter called the dHvA effect) is a quantum oscillation of the magnetization of the conduction electrons as a function of the magnetic field,  $\vec{H}$ . It is one of the most powerful methods for the determination of the geometric structure of the Fermi surfaces of pure metals, semimetals, intermetallic compounds and dilute alloys. The effect appears as small amplitude quantum oscillations, periodic in  $H^{-1}$ , in the magnetization of sufficiently pure metallic single crystals. The frequency,  $F_i$ , of the oscillatory magnetization is directly proportional to an extremal cross-sectional area,  $S_i$ , of the Fermi surface normal to the magnetic field;  $F_i = (\hbar c/2\pi e)S_i$ . These oscillations can be observed either by changing the magnitude of the dc magnetic field keeping its direction fixed or by changing the dHvA frequency through rotating  $\vec{H}$  while keeping its magnitude constant. Measurements of the angular variations of the dHvA frequencies have proved to be quite useful for obtaining accurate information on the shapes and sizes of the Fermi surfaces, and was used to obtain most of the final results for pure antimony. These measurements have had a great influence on understanding the electronic band structures of metals (see for example: Ashcroft 1963). The precision of the electronic band structure deduced from the dHvA measurements, depends on both the completeness and accuracy with which the measurements are

recorded. Therefore, it is important that complete and precise dHvA data be obtained for each metal. The temperature dependence of the dHvA oscillation amplitude contains the gradient on the Fermi surface, that is, the cyclotron effective mass, whereas its magnetic field dependence determines the Dingle temperature which is a measure of the scattering of the conduction electrons at defects.

Two characteristic features of the dHvA effect should be emphasized. First, only the electronic states at the Fermi level and in its immediate vicinity can be studied by the dHvA effect. This is true since only these states are influenced by the depletion of Landau levels when a cylinder leaves the Fermi surface (see section 2 of Chapter 2). The second feature is that all physical parameters derived from the dHvA effect are averages over the extremal cross-section of the Fermi surface for the field direction under consideration. Thus, the dHvA frequency is an orbital average over the extremal cross-section. The cyclotron masses are orbital averages of the Fermi velocities and the Dingle temperatures are orbital averages of the electron scattering rates.

The investigation of the influence of hydrostatic pressure on the dHvA effect in a metal, which is the primary concern of the present studies, yields valuable information on the corresponding changes of the geometric structure of the Fermi surface. This information can serve as a useful tool in determining the validity of band structure calculations (Harrison, 1965). Since the dHvA frequency is directly proportional to the cross-sectional area of the Fermi surface, the

pressure derivatives of the Fermi surface cross-sections can be derived from the pressure dependences of the dHvA frequencies. The magnitude of the cyclotron effective mass obtainable from the dHvA effect is expected to differ from the band structure mass predicted in the one-electron model because of mass enhancement due to many-body interactions, that is, electron-electron and electron-phonon interactions. The application of pressure influences the magnitudes of the band structure mass and the many-body mass enhancement parameters and allows one to test many-body and band theories. The magnitude of each parameter and its corresponding pressure dependence is generally not accessible experimentally for one metal, since experimental evidence for such mass enhancements has so far been limited to noting the differences between the measured masses and calculated band masses. However, it is possible to separate the effect of each individual parameter by choosing two different metals with negligible and dominant many-body effects, especially the electron-phonon interaction. Antimony (a semimetal) and potassium (a simple alkali metal) fulfill these criteria and we have chosen them to identify separately the influences of pressure on the band structure mass and the many-body mass enhancement parameters with pressure, respectively.

The present experimental studies have been undertaken for two reasons:

- i) To provide precise measurements of the hydrostatic pressure dependences of the cyclotron effective masses in pure potassium and antimony up to 4.4 kbar using the helium freezing method. In addition,

accurate determinations of cyclotron masses at standard atmospheric pressure (1 bar), were obtained for both elements. The masses were derived from the temperature dependence of the dHvA oscillatory magnetization amplitude. The cyclotron effective mass of pure potassium at standard atmospheric pressure has been used recently by Dunifer et al (1984) in the analysis of spin waves in potassium. Sodium has been studied previously for the pressure dependence of the cyclotron effective mass by Elliott and Datars (1982). This was followed by theoretical calculations of the electron quasiparticle masses for the alkali metals (lithium, sodium, and potassium) that took into consideration the volume dependence of the band mass as well as electron-phonon and electron-electron mass enhancement parameters (Leavens et al 1983).

ii) To provide precise information on the influence of hydrostatic pressure on the hole Fermi surface anisotropy of pure antimony up to 4.4 kbar and to extend experimentally the results on the pressure dependences of a few selected sections of the Fermi surface. In no previous measurements has the pressure dependence of the anisotropy of the entire hole Fermi surface been treated specifically in the pressure region covered in the present investigation. However, there exists experimental information on the responses of the minimum and maximum sections of the hole surface, to pressure (see for example: Schirber and O'Sullivan 1970, and Brandt et al 1978).

This thesis is organized as follows. In chapter 2, the dHvA effect is explained and the Lifshitz-Kosevich expression for the oscil-



latory magnetization is presented. Chapter 3 gives a description of the crystal structure and Fermi surface of pure antimony. Also a brief review of the previous investigations made on antimony is included in this chapter. In chapter 4, details of the field modulation measuring technique and how it can be used to optimize the selectivity and sensitivity of the dHvA experiment are given in some detail. This includes theory, methods, apparatus for measuring the effect, preparation, alignment and handling of samples and finally the solid helium high pressure technique. Chapter 5 presents results and discussion of the hydrostatic pressure dependence of the cyclotron effective mass in potassium. The influence of the band structure effects and many-body effects (especially the electron-phonon interaction) on the enhancement of  $m^*$  with pressure are treated at some length. The experimental results and analysis of the pressure dependence of the hole Fermi surface anisotropy and cyclotron effective mass, are given in chapter 6. The discussion and final analysis of these results are given in chapter 7. Finally, in chapter 8, conclusions of this work are presented.

## CHAPTER 2

### PHYSICAL ASPECTS OF THE DE HAAS-VAN ALPHEN EFFECT

#### 1. Electrons in a uniform magnetic field

In the absence of a magnetic field, the conduction electrons in a metal have a continuous range of energies up to the Fermi energy  $E_F$ , and all states with energies up to  $E_F$  are occupied at absolute zero temperature. The Fermi surface separates the occupied and unoccupied states. The different electronic states are characterized by the wave vectors  $\tilde{k}$ , and the spin quantum numbers  $s$ . According to the Pauli principle each state  $(\tilde{k}, s)$  can be occupied only once.

When a magnetic field  $\tilde{H}$  is applied to an electron, its motion takes on certain characteristic features. By studying the changes which occur in a magnetic field, it is possible to deduce important information about the electronic properties of metals. In such a field, the electron experiences the Lorentz force perpendicular to its velocity  $\tilde{v}$ , and perpendicular to the magnetic field  $\tilde{H}$ , so that the semiclassical equations of motion are

$$\hbar \frac{d\tilde{k}}{dt} = \left(\frac{-e}{c}\right) \tilde{v}_F(\tilde{k}) \times \tilde{H} \quad , \quad (2.1)$$

$$\tilde{v}_F(\tilde{k}) = \frac{d\tilde{r}}{dt} = \frac{1}{\hbar} \nabla_{\tilde{k}} E(\tilde{k}) \Big|_{E_F} \quad (2.2)$$

where  $E(\tilde{k})$  is the energy as determined in the absence of the magnetic field. The Lorentz force causes the wave vector of the electron to change only along the curve of constant energy (the cyclotron orbit)

formed by the intersection of the constant energy surface with a plane perpendicular to  $\tilde{H}$ . The corresponding motion of the electrons in real space can be obtained by integrating equation (2.1) with respect to time. This gives

$$\tilde{k} = \left( \frac{-e}{\hbar c} \right) \tilde{r} \cdot \tilde{H} \quad (2.3)$$

Thus, the projection of the real space orbit on a plane perpendicular to  $\tilde{H}$  has the same shape as the reciprocal space orbit but is rotated by  $90^\circ$  and scaled by a factor  $(\hbar/eH)$ .

The cyclotron frequency  $\omega_c$  at which the electrons move on the cyclotron orbit, is given by

$$\omega_c = \frac{eH}{m_c^* c} \quad (2.4)$$

where  $m_c^*$  is the cyclotron effective mass, and  $c$  is the velocity of light. A useful geometrical definition of  $m_c^*$  can be obtained in the following manner. According to equations (2.1) and (2.4), the cyclotron period  $T_c$  is

$$\begin{aligned} T_c &= \frac{2\pi}{\omega_c} = \frac{2\pi c m_c^*}{eH} \\ &= \oint dt = \left( \frac{\hbar c}{eH} \right) \oint \frac{dk}{v_{\perp}} \end{aligned} \quad (2.5)$$

Hence

$$m_c^* = \frac{\hbar}{2\pi} \oint \frac{dk}{v_{\perp}} \quad (2.6)$$

where  $v_{\perp}$  is the component of  $\tilde{v}$  in a plane normal to  $\tilde{H}$  at the point  $k$ .

It is given by

$$v_{\perp} = \frac{1}{\hbar} \nabla_{k_{\perp}} E(\tilde{k}) . \quad (2.7)$$

Therefore

$$\begin{aligned} m_c^* &= \frac{\hbar^2}{2\pi} \int_0^1 \frac{d\tilde{k}}{\nabla_{k_{\perp}} E(\tilde{k})} \\ &= \frac{\hbar^2}{2\pi} \frac{1}{\delta E} \int_0^1 \Delta k_{\perp} dk \\ &= \frac{\hbar^2}{2\pi} \left. \frac{\partial S}{\partial E} \right|_{E_F} \end{aligned} \quad (2.8)$$

where  $\partial S$  is the area between two orbits of energy  $E$  and  $E+\delta E$ . Thus,  $m_c^*$  is a measure of the rate of change of cross-sectional area with energy at the Fermi surface and  $S$  is the area in  $\tilde{k}$ -space enclosed by the cyclotron orbit in the plane normal to  $\tilde{H}$ .

The area enclosed by the cyclotron orbit can be obtained from the Bohr-Sommerfeld quantization formula

$$\int_0^1 \tilde{P} \cdot d\tilde{r} = \int_0^1 \left( \hbar \tilde{k} - \frac{e\tilde{A}}{c} \right) \cdot d\tilde{r} = 2\pi\hbar(n+\gamma) \quad (2.9)$$

where  $n$  is an integer,  $\gamma$  is a phase factor ( $\frac{1}{2}$  for free electron) and  $\tilde{r}$  and  $\tilde{k}$  specify the position of the electron in real and reciprocal space, respectively.  $\tilde{P}$  is the momentum operator and  $\tilde{A}$  is the vector potential  $\tilde{A}(0, Hx, 0)$  whose curl gives the field  $\tilde{H}$  in the  $z$  direction. With the aid of equation (2.1) and by using Stokes theorem, the quantum condition (2.9)

may be rewritten as

$$\begin{aligned}
 \oint \tilde{\mathbf{P}} \cdot d\tilde{\mathbf{r}} &= \frac{e}{c} \left\{ \oint \tilde{\mathbf{r}} \times \tilde{\mathbf{H}} \cdot d\tilde{\mathbf{r}} - \oint \tilde{\mathbf{A}} \cdot d\tilde{\mathbf{r}} \right\} \\
 &= \frac{e}{c} \left\{ H \oint \tilde{\mathbf{r}} \cdot d\tilde{\mathbf{r}} - \oint \nabla \times \tilde{\mathbf{A}} \cdot d\tilde{\mathbf{a}} \right\} \\
 &= \frac{e}{c} \{ 2\phi - \phi \} = \frac{e}{c} \phi
 \end{aligned} \tag{2.10}$$

where  $\phi$  is the product of  $H$  and the projected area of the real space orbit on a plane normal to  $H$ . Thus, the quantum condition becomes

$$\frac{eH}{c} A_n = 2\pi\hbar(n+\gamma) \tag{2.11}$$

It is apparent that the areas of the cyclotron orbits in real space are quantized. The corresponding areas in  $\tilde{\mathbf{k}}$ -space can be obtained by multiplying equation (2.11) by the area scaling factor  $e^2 H^2 / c^2 \hbar^2$ . Therefore, the quantization condition for the allowed areas  $S$  in  $\tilde{\mathbf{k}}$ -space is

$$S_n = \Delta S (n + \gamma)$$

with

$$\Delta S = \frac{2\pi eH}{\hbar c} \tag{2.12}$$

This is Onsager's famous result (Onsager, 1952). It is of primary importance for the de Haas-van Alphen effect. It indicates that the cyclotron orbits in  $\tilde{\mathbf{k}}$ -space are quantized and expand with the field so that the areas enclosed by them increase linearly with  $H$ . It also states that cyclotron orbits at adjacent allowed energies enclose areas that differ by the fixed amount,  $\Delta S$ .

For a magnetic field  $\vec{H}$  directed along the z-axis, the Hamiltonian for free electrons of mass,  $m$ , neglecting spin is

$$H = \frac{1}{2m} \left( \vec{p} - \frac{e\vec{A}}{c} \right)^2$$

$$= \frac{1}{2m} \{ p_x^2 + p_z^2 + (p_y - m\omega_c x)^2 \} \quad (2.13)$$

If  $x_0 = p_y/m\omega_c$  equation (2.13) can be rewritten as

$$H = \frac{1}{2m} \{ p_x^2 + m^2 \omega_c^2 (x - x_0)^2 \} + \frac{\hbar^2 k_z^2}{2m} \quad (2.14)$$

which is the Hamiltonian for a harmonic oscillator of frequency  $\omega_c$  centred at  $x_0$ , plus an energy term varying with  $k_z$ , the component of the momentum along the magnetic field. The eigen values are therefore

$$E(n, k_z) = (n+1/2)\hbar\omega_c + \frac{\hbar^2 k_z^2}{2m} \quad n = 0, 1, 2, \dots \quad (2.15)$$

When the spin of the electron is taken into account the expression for the energy contains an additional term,  $gSH\sigma_z$ , where  $g$  is the effective  $g$  factor,  $\beta = e\hbar/2mc$  is the Bohr magneton, and  $\sigma_z = \pm 1/2$  is the  $z$  component of the spin angular momentum

$$E(n, k_z, \pm \frac{1}{2}) = (n+1/2)\hbar\omega_c + \frac{\hbar^2 k_z^2}{2m} \pm \frac{1}{2} gSH \quad (2.16)$$

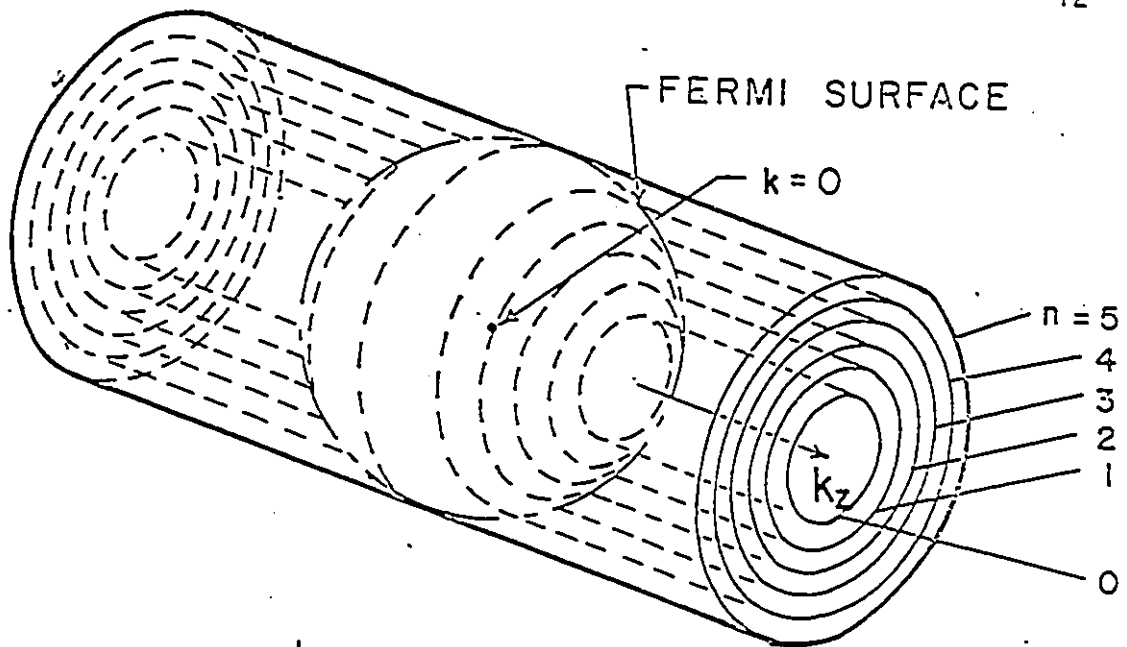
Thus, the energy of the electron states is expressed as the sum of a translational energy along the magnetic field, together with the quantized energy of the cyclotron motion in the plane normal to the field. In physical terms, the magnetic field has redistributed the zero field

parabolic band structure,  $E(k) = \hbar^2 k^2 / 2m$ , into a series of quantized states arranged on a system of cylinders, the Landau cylinders (figure 2.1). For free electrons these are concentric cylinders with circular cross-sections and axis parallel to the magnetic field. For arbitrary energy surfaces, these cylinders need not be parallel to  $\vec{H}$ . For example, for an ellipsoidal Fermi surface, the cylinder axis only coincides with the field direction, when a principal axis of the ellipsoid is parallel to the field direction (Gold, 1968).

The degeneracy of the electronic states is also changed by the magnetic field. In the absence of a field, a state  $\vec{k}$  can be occupied twice. With a magnetic field  $\vec{H}$  parallel to  $\vec{k}_z$ , the degeneracy of the Landau levels was found (Ziman, 1968) to be

$$\frac{eH}{4\pi^2 \hbar c} \Delta k_z, \quad (2.17)$$

for states of each spin, per Landau level, for a slice of thickness  $\Delta k_z$  of  $\vec{k}$ -space normal to  $\vec{H}$ , when the cylinder has a unit volume. Thus, the degeneracy increases linearly with the field. This is a consequence of the localization of the charge in the field. Whereas a conduction electron in state  $\vec{k}$  is spread out through the whole crystal, it is localized on a cylinder with radius  $v/\omega_c$  in the state  $(n, k_z)$ . At increasing field, the effect of decreasing the number of Landau cylinders and increasing degeneracy compensate, so that the number of electrons can be accommodated inside the Fermi surface as at zero field, considering that the Fermi energy is field independent.



k-SPACE

FREE ELECTRON LANDAU LEVELS

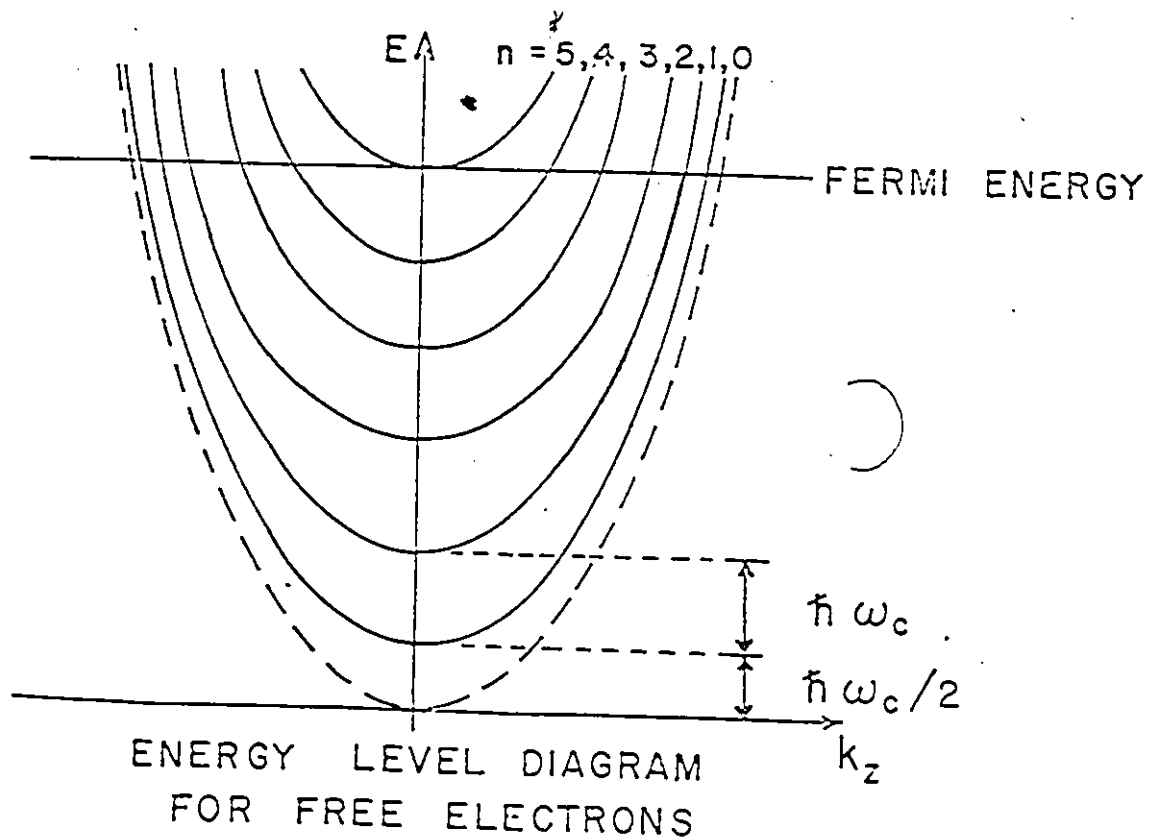


FIGURE 2-1



## 2. Density of electronic states and origin of the de Haas-van Alphen oscillations

The quantization condition given by equation (2.13) imposes large oscillatory structure in the electronic density of states right at the Fermi energy and in its immediate vicinity. The total density of states for free electrons in the magnetic field (Ziman 1972) per unit energy and unit volume is given by

$$N_H(E) = \frac{eH}{(2\pi c)^2} \left(\frac{2m^*}{\hbar^2}\right)^{3/2} \sum_n \left(E - \left(n + \frac{1}{2}\right)\hbar\omega\right)^{1/2} \quad (2.18)$$

The summation over  $n$  contains all occupied quantum states. Whenever the energy coincides with that of a Landau level, the density of states diverges. Essentially this is due to oversimplification which neglects the finite width of the Landau levels. If collision broadening is taken into account, the divergence disappears (Landwehr, 1969). Thus  $N_H(E)$  will drop abruptly each time a Landau cylinder leaves the Fermi surface. Basically, this will occur each time the value of the magnetic field causes an extremal orbit on the Fermi surface to satisfy the periodic condition

$$\left(\frac{c\hbar}{2\pi e}\right) \frac{S_{ex}}{H} = n \quad (2.19)$$

where  $S_{ex}$  is the cross-sectional area of the Fermi surface. With increasing field, the Landau cylinders expand and leave the Fermi surface one by one. As a result, the electronic density of states at the Fermi level changes periodically with the field. At this point it should be noted that the discrete nature of the Landau cylinders is smeared out

unless their energy separation  $\hbar\omega$  is larger than  $kT$ , where  $k$  is Boltzmann's constant. Another requirement for the observation of quantum effects is that a complete orbit in  $\tilde{k}$ -space be performed by the electrons before they are scattered. This can be formulated by the condition  $\omega\tau > 1$  ( $\tau$  is the relaxation time). The quantum oscillations will occur in all physical quantities which contain the density of states and in particular the free energy of the conduction electrons (i.e. the de Haas-van Alphen effect).

Figure 2.2 illustrates the origin of the de Haas-van Alphen oscillations. The periodic change in the electronic density of states gives rise to changes in the free energy which are periodic in reciprocal magnetic field. The contributions to the free energy from different slices of  $\tilde{k}$ -space normal to  $\tilde{H}$  vary in phase, however, and are additive only for regions of the Fermi surface cross sectional areas normal to  $\tilde{H}$  are stationary as a function of the components  $k_H$  of  $\tilde{k}$  along  $\tilde{H}$ . Whenever the Landau cylinder is tangent to the Fermi surface at a certain magnetic field strength e.g.  $H_1$ , the free energy of the conduction electrons will reach its maximum value because the states on the equator at the Fermi surface are occupied and have the highest energy of all occupied states. When the field increases from  $H_1$  to  $H_2$ , the  $n$ th Landau cylinder leaves the Fermi surface. The states on the equator of the Fermi surface are depleted and the corresponding electrons are redistributed, on lower energy states. Thus, the free energy decreases to a minimum in a small field interval. With further increases in field, the Landau cylinders further expand, the free energy increases again and reaches another maximum when the  $(n-1)$ th cylinder is tangent to the Fermi surface. This completes a cycle of an oscillation of the free energy of the conduction electrons.

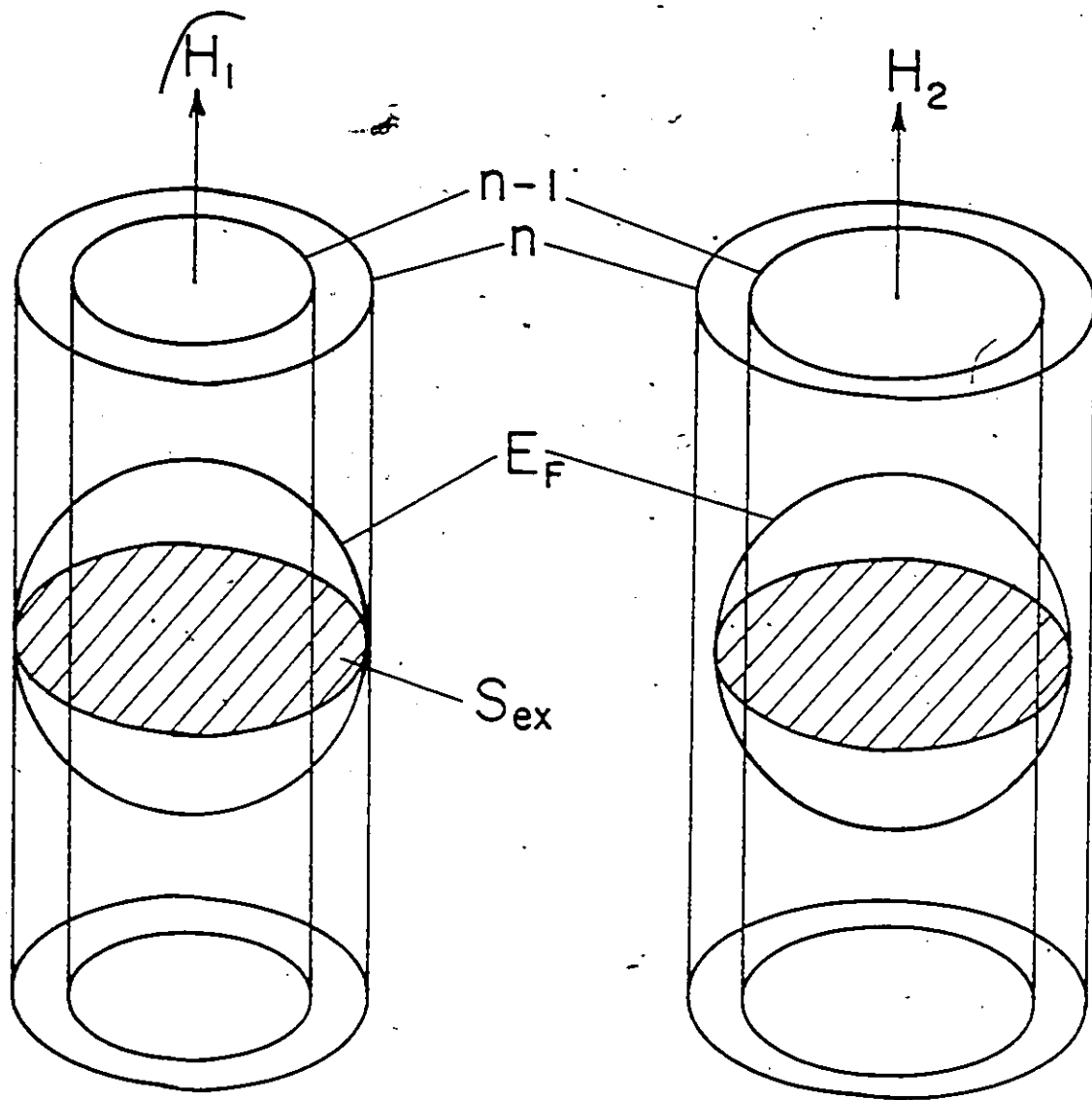


FIGURE 2-2  
THE ORIGIN OF THE  
DHVA EFFECT

### 3. Lifshitz-Kosevich expression for the de Haas-van Alphen effect

The theory of the de Haas-van Alphen effect is described quantitatively by Lifshitz and Kosevich (1955). In this theory, the free energy of the conduction electrons is calculated for arbitrary energy surfaces as a function of the magnetic field  $\tilde{H}$ . The expression of the oscillatory magnetization of the conduction electrons in a single crystal at temperature  $T$ , in spherical polar coordinates, is determined from the gradient of the oscillatory part of the free energy with respect to  $\tilde{H}$ .

It is given by

$$\begin{aligned} \tilde{M}_i(H, \theta, \phi, T) = & \sum_i \sum_{r=1}^{\infty} \left\{ \tilde{H} - \frac{1}{F_i(\theta, \phi)} \frac{\partial F_i(\theta, \phi)}{\partial \theta} \hat{\theta} - \frac{1}{F_i(\theta, \phi) \sin \theta} \frac{\partial F_i(\theta, \phi)}{\partial \phi} \hat{\phi} \right\} \\ & \times \{ A_i(H, \theta, \phi, T) \sin[2\pi r \left( \frac{F_i(\theta, \phi)}{H} - \gamma_i \right) \mp \frac{\pi}{4}] \} ; \end{aligned}$$

At  $r$ th harmonic

$$\begin{aligned} A_i(H, \theta, \phi, T) = & D_i(H, \theta, \phi) r^{-3/2} (2\pi^2 r m_i^*(\theta, \phi) k_B T / e\hbar H) \\ & \times \exp(-2\pi^2 r m_i^*(\theta, \phi) k_B T_D / e\hbar H) \\ & \times [\sinh(2\pi^2 r m_i^*(\theta, \phi) k_B T / e\hbar H)]^{-1} \\ & \times \cos\left(\frac{\pi}{2} r g_i(\theta, \phi) \frac{m_i^*}{m_0}\right) \end{aligned} \quad (2.20)$$

In this equation the summation over  $i$  contains all external cross-sectional areas of the Fermi surface for given  $(\theta, \phi)$ ;  $\theta$  is the angle between  $k_z$  and  $\tilde{H}$ , and  $\phi$  measures the angle between  $k_x$  and the projection of  $\tilde{H}$  in the  $k_x$ - $k_y$  plane.  $A(H, \theta, \phi, T)$  and  $2\pi r \left\{ (F_i(\theta, \phi)/H) - \gamma_i \right\} \mp \frac{\pi}{4}$  are the amplitude and phase, respectively of the quantum oscillations with frequency  $F_i(\theta, \phi)$ , for a given temperature  $T$ , magnetic field strength  $H$ , and mag-

netic field orientation  $(\theta, \phi)$  with respect to the crystallographic axes.. The - and + are used for a maximum or minimum section, respectively.  $F_i(\theta, \phi)$  is related to the  $i$ th extremal cross sectional area  $S_i(\theta, \phi)$  of the Fermi surface in the plane normal to  $\vec{H}$  by Onsager's relation (Onsager 1952)

$$F_i(\theta, \phi) = \frac{\hbar c}{2\pi e} S_i(\theta, \phi) . \quad (2.21)$$

When only one of the frequency components of equation (2.20) is considered, it is clear that the magnetization associated with it will show sinusoidal variations periodic in  $1/H$  and with the de Haas-van Alphen frequency  $F(\theta, \phi)$ . These oscillations are caused by a variation in the part of the phase

$$\phi_i = \frac{2\pi F_i(\theta, \phi)}{H} = 2\pi n . \quad (2.22)$$

Here,  $n$  is a large number for most metals even with the highest magnetic field strength which is normally used to observe the effect. Physically,  $n$  is the number of contours of constant phase (i.e. the number of occupied Landau levels) just below the Fermi level. For example, in a monovalent alkali metal the frequency  $F = 5 \times 10^8$  Gauss. Thus,  $n = 5000$  in a magnetic field of  $10^5$  Gauss. The fact that  $n \gg 1$  makes the effect a very sensitive tool for studying relative changes in the extremal cross-sectional areas of the Fermi surface. For if the magnitude of  $\vec{H}$  is kept constant and its direction is varied, then a change in  $F$  of only one part in a large number  $n$  can be easily detected, since it will cause the magnetization to go through one complete cycle.

Based on equation (2.20) the factors which contribute to determining the de Haas-van Alphen are as follows:

(1) The curvature  $\partial^2 S_i(\theta, \phi) / \partial k_H^2$  at the extremum: At  $T=0$ , the Fermi surface is sharp, and if the electrons are not scattered at defects, the Landau cylinder is sharp as well, and the expression for the amplitude  $A(H, \theta, \phi, T)$ , equation (2.20), reduces to

$$A_i(H, \theta, \phi, T) = D_i(H, \theta, \phi) = - \frac{e\hbar S_i(\theta, \phi)}{4\pi^4 m_i^* (\theta, \phi)} \left( \frac{2\pi eH}{\hbar} \right)^{1/2} \left| \frac{\partial^2 S_i(\theta, \phi)}{\partial k_H^2} \right|^{-1/2} \quad (2.23)$$

This is the maximum value of the amplitude and can only be realized at  $T=0$  for a sharp Landau cylinder. The term  $\left| \partial^2 S_i(\theta, \phi) / \partial k_H^2 \right|$  is the curvature of the Fermi surface at the extremum. It effectively determines the number of electrons that will contribute in phase to produce the de Haas-van Alphen signal. If the curvature is small, many electrons will have similar orbits and the resulting de Haas-van Alphen amplitude is large. If the curvature is large, the amplitude is correspondingly small.

(2) The temperature: At finite temperatures, the Fermi surface becomes slightly diffuse and the depletion of the states associated with the outermost Landau cylinders becomes gradual leading to a thermal damping of the oscillations (Gold, 1968). Thus the magnetization is reduced in amplitude. The damping depends on the ratio  $\hbar\omega/k_B T$ , where  $k_B$  is the Boltzmann's constant. The quantum oscillations are only observable if  $k_B T / \hbar\omega \ll 1$ . Thus, a field of the order of  $10^4$  Gauss and temperatures as

low as a few degrees Kelvin are required to detect the de Haas-van Alphen oscillations. The hyperbolic sine term in equation (2.20) contains the main temperature effect on the amplitude. The cyclotron effective mass,  $m^*$ , is derived from the temperature dependence of the oscillation amplitude.

(3) Collision broadening of the levels: Electron scattering at defects can cause similar problems. According to the uncertainty principle, if the relaxation time of the electron is  $\tau$ , then its energy can be defined only to within  $\Delta E \sim \hbar/\tau$ . If  $\Delta E > \hbar\omega$ , the oscillatory structure will be appreciably diminished. Thus the scattering broadens the Landau levels. In a phenomenological approach Dingle (1952) described this broadening by a Lorentzian of width  $2\pi k_B T_D$ , where  $T_D$  is the Dingle temperature. It is related to the relaxation time  $\tau$  by

$$T_D = \frac{\hbar}{2\pi k_B} \langle \tau \rangle^{-1} \quad (2.24)$$

The damping in the amplitude due to scattering depends on the ratio  $k_B T_D / \hbar\omega$  mentioned above.  $\langle \tau \rangle^{-1}$  is the reciprocal of the relaxation time,  $\tau$ , averaged around the cyclotron orbit. The relaxation time may be determined by studying the field dependence of the de Haas-van Alphen amplitudes. However, these measurements may be complicated by field dependences due to other causes such as crystal imperfection or field inhomogeneity (Shoenberg, 1969).

(4) Electron spin: The effect arises from the lifting of spin degeneracy by the magnetic field has been incorporated (Dingle, 1952, and Cohen and Blount, 1960) into equation (2.20) by multiplying each term by

the factor  $\cos(\pi r g_i m_i^*/2m_0)$ . The electron spin splits the Landau level into systems of Landau levels shifted in energy by an amount,  $\pm(gm^*/2m_0)\hbar\omega$ , where  $g$  is the electron spin splitting factor and  $m_0$  is the free electron mass. According to equation (2.16), an electron in state  $(n, k_z = 0, \sigma_z)$  has the energy

$$E = \hbar\omega\left(n + \frac{1}{2} \pm \frac{1}{2} (gm^*/2m_0)\right). \quad (2.25)$$

Thus, there are two sets of levels with the same spacing but shifted in phase by  $2\pi(gm^*/2m_0)$ . The spin splitting reduces the de Haas-van Alphen amplitude according to the factor  $\cos(\pi r g_i m_i^*/2m_0)$ . For appropriate field directions this shift causes the oscillations in the two terms of equation (2.25) to fall  $180^\circ$  out of phase, yielding zero amplitude. These are the principal theoretical contributions to the amplitude, so far as is known. There are also experimental influences which tend to reduce the amplitude, such as mosaic structure of the specimen and inhomogeneity of the magnetic field. However this does not prevent the temperature dependence from being used to determine the cyclotron effective mass.

The summation over  $r$  in equation (2.20) contains the harmonic content of the oscillations. The first;  $r=1$ ; is the largest unless the term  $\cos(\pi r g_i m_i^*/2m_0)$  interferes by giving a spin splitting zero. Note that the direction of the oscillatory magnetization,  $\tilde{M}_i$ , is not always in the direction of the magnetic field but it deviates to some extent by the shape of the Fermi surface as indicated by the coefficients  $\partial F_i(\theta, \phi)/\partial \theta$  and  $\partial F_i(\theta, \phi)/\partial \phi$ . When these coefficients are zero (i.e. for spherical Fermi surface),  $\tilde{M}_i$  is parallel to the field direction.



CHAPTER 3  
CRYSTAL STRUCTURE AND FERMI  
SURFACE OF ANTIMONY

Antimony is a semimetal which crystallizes into a lattice with rhombohedral symmetry of the A7 classification similar to bismuth and arsenic (Dresselhaus 1970). This structure can be obtained from a simple cubic structure by performing two independent distortions: an internal displacement and a rhombohedral shear along the body diagonal. The first distortion can be visualized if the simple cubic lattice is thought of as being composed of two interpenetrating face-centered cubic sublattices, where the two sublattices are related by a translation along the body diagonal of the original simple cube. The origins of the two sublattices are taken at  $(0,0,0)$  and  $(2u,2u,2u)$ . Here,  $u$  is half of the distance between the atoms. The A7 structure is generated by performing a slight displacement of one face-centred cubic lattice relative to the other along the body diagonal of the cube. This displacement results in a small reduction in the value of  $u = (1/4)a$  for the undistorted simple cubic lattice. The second distortion of the lattice is a shear along the same body diagonal that is involved in the displacement which yields a small reduction in the angle,  $\alpha = 60^\circ$ , between the unit vectors  $\tilde{a}_1$ ,  $\tilde{a}_2$  and  $\tilde{a}_3$  of the undistorted simple cubic structures. The body diagonal retains its 3-fold symmetry and becomes the trigonal axis of the A7 structure. A summary of the parameters specifying the crystal structure of bismuth,

antimony and arsenic are listed in Table 3-1.

Since the rhombohedral primitive cell is closely related to the face-centred cubic lattice, the Brillouin zone of the A7 structure is nearly identical to that of a face-centred cubic lattice but is compressed along  $\Gamma T$ , the cube body diagonal. The Brillouin zone of the A7 structure along with its cross-section is shown in figure 3-1 with important symmetry points marked with standard symbols. The slight distortion from the cubic structure causes the L points to be centers of pseudo-hexagonal faces. The T points, however, remain centers of hexagonal faces. There now remain the following elements of the cubic symmetry: The 3-fold axis  $\Gamma T$  (trigonal axis), the three binary axes,  $\Gamma K$  perpendicular to  $\Gamma T$ , and the three mirror planes  $120^\circ$  apart intersecting parallel to the trigonal axis. A third axis perpendicular to both the binary and trigonal is usually defined and called the bisectrix axis. These three crystallographic axes (trigonal, binary and bisectrix), which are mutually orthogonal, are the axes to which experimental data are most frequently related. It should be pointed out that, in the mirror plane  $\sigma(\Gamma TXL$  in figure 3-1) rotations from the trigonal axis  $\Gamma T$  by equal amounts in opposite senses are not equivalent. The A7 crystal structure has been described by Falicov and Golin (1965) in some detail.

In all semimetals, including antimony, there are two atoms per unit cell, and five valence electrons per atom. Therefore, the electron volume in reciprocal space is five Brillouin zones. However, due to a small overlap between the fifth and sixth zones, an equal number of holes (in the fifth zone) and electrons (in the sixth zone) are formed

Table 3-1  
 Crystal structure parameters for arsenic, antimony and bismuth

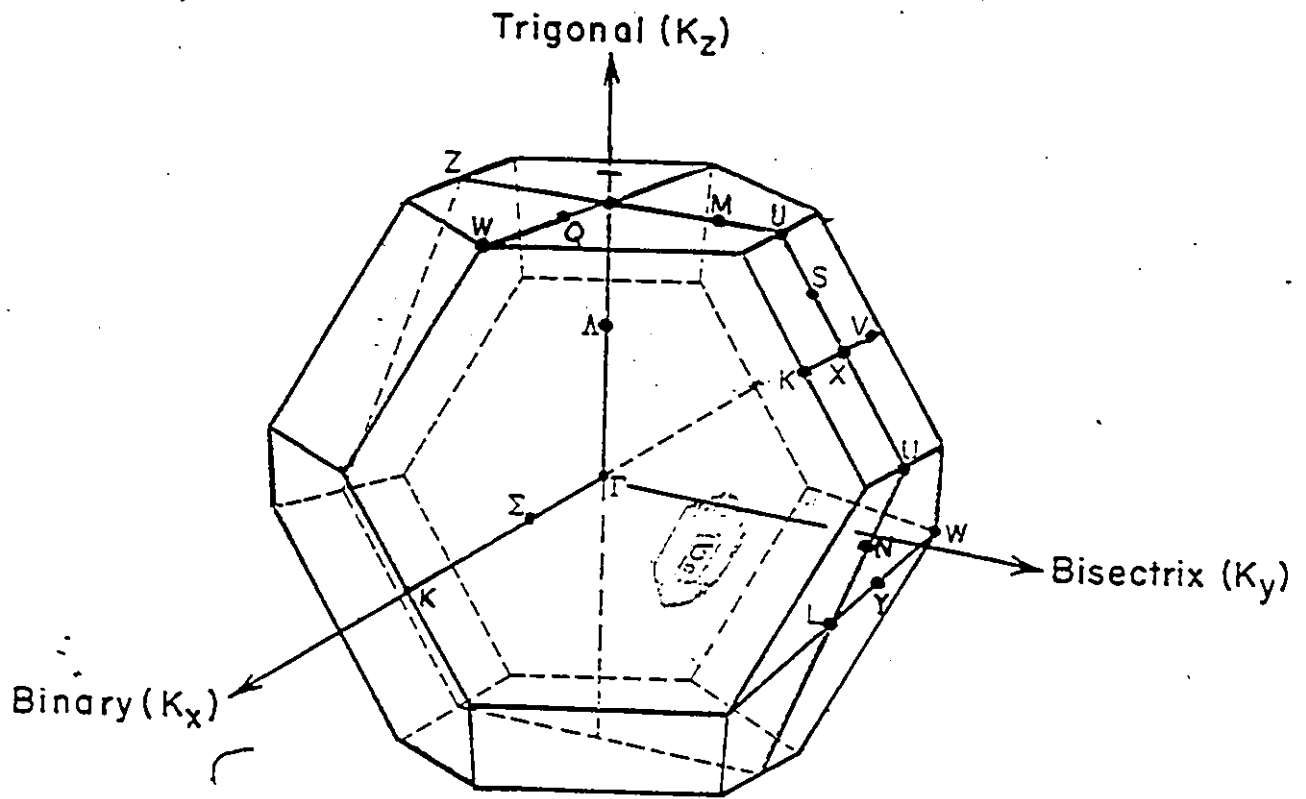
Structure	$a(\text{\AA})^{\dagger}$	$\alpha$	$u/a$	Source <sup>††</sup>
Arsenic	4.12	$54^{\circ} 10'$	0.226	Falicov and Golin (1965)
Antimony	4.50	$57^{\circ} 14'$	0.234	Falicov and Lin (1966)
Bismuth	4.74	$57^{\circ} 14'$	0.237	Abrikosov <u>et al</u> (1963)
Simple cubic	-	$60^{\circ}$	0.250	Falicov and Golin (1965)

<sup>†</sup>These values are quoted from Cracknell and Wong (1973).

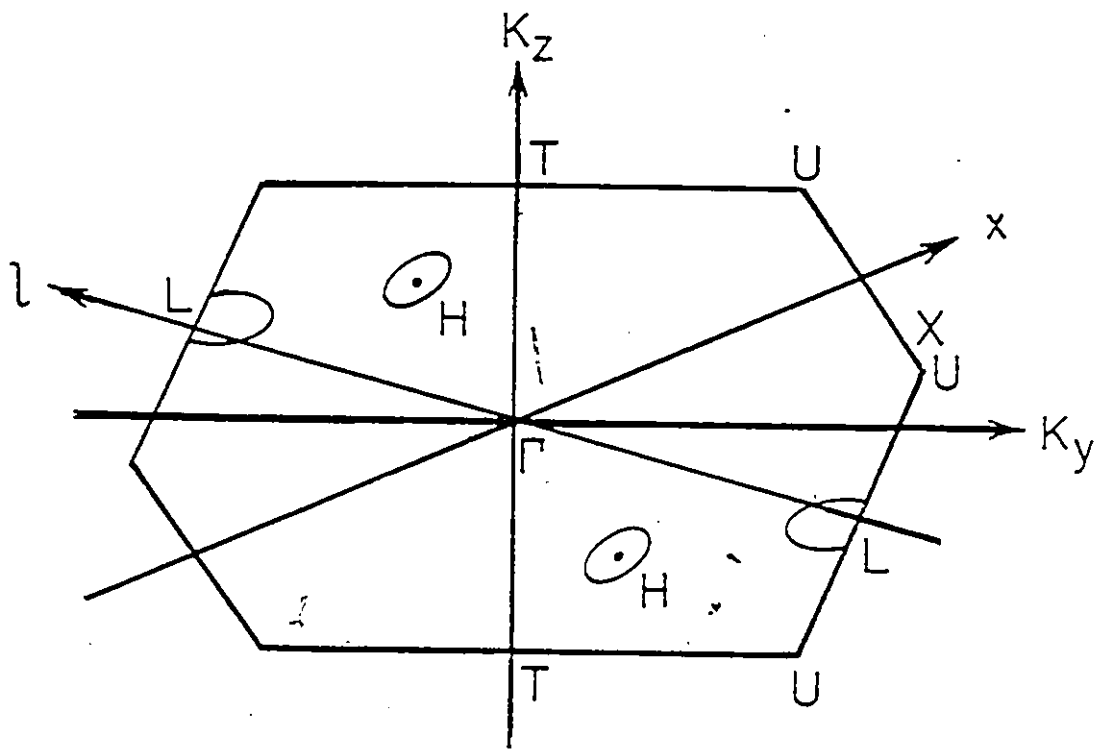
<sup>††</sup>The original sources are quoted in the references indicated.

Figure 3-1. a) The Brillouin zone of antimony showing the points, lines and planes of symmetry.  $\Gamma T$  is in the direction of the trigonal-axis ( $k_z$ ).  $\Gamma K$  is in the direction of the binary axis ( $K_x$ ). A bisectrix-axis ( $K_y$ ) in the mirror plane completes a right-handed coordinate system. Angles in the  $yz$ -plane are measured from the  $z$ -axis and are positive toward  $\Gamma X$  in the first quadrant of the coordinate system.  $\Gamma T$  is at  $0^\circ$ ,  $\Gamma X$  is at  $+58^\circ 17'$ ,  $\Gamma U$  is at  $+75^\circ 27'$ , and  $\Gamma L$  is at  $+107^\circ 10'$ .

b) Cross-section of the Brillouin zone of antimony corresponding to  $K_x = 0$ . At the points H there are holes (six pockets) and at L there are electrons (three pockets).



(a)



(b)

in small pockets, giving rise to semimetallic behaviour. It has been established with a good degree of certainty both experimentally (see for example Windmiller, 1966) and theoretically (Falicov and Lin, 1966 and Rose and Schuchardt, 1983) that the Fermi surface of antimony consists of two sets of small pockets whose dimensions are of the order of  $10^{-2}$  of the size of the Brillouin zone: the electron set having a tilt angle of  $87.7^\circ$  (Windmiller 1966) and the hole set having a tilt angle of  $53^\circ$ . The tilt angles are defined by the minimum cross-sectional area of the Fermi surfaces in the trigonal-bisectrix plane ( $\sigma$  TXL). The angles are measured from  $\Gamma$ T in the sense toward  $\Gamma$ X. The electron set consists of three equivalent closed pockets located about L points of the Brillouin zone and the hole set consists of six equivalent closed pockets located symmetrically about the T points (see figure 3-1b). The electron and hole pockets have one principal axis parallel to twofold (binary) axes of symmetry, while their other two axes are tilted away from the trigonal axis. The electron pockets enclose a volume in reciprocal space that is twice as large as the volume of the hole pockets. These pockets can be roughly approximated by a tilted ellipsoid. However, departure from ellipsoidal shape is large enough to be measured experimentally.

The Fermi surface of antimony at standard atmospheric pressure has been investigated by many workers using various techniques. Some of these studies are briefly listed below. Brandt (1967), Ishizawa (1968), and in particular Windmiller (1966), have made a complete study of the Fermi surface of antimony by means of the de Haas-van Alphen effect. The radio frequency size effect measurements of Herrod et al (1971) have pro-

vided precise determination of the dimensions and shapes of the electron and hole Fermi surfaces. Their results are in good agreement with de Haas-van Alphen measurements. Cyclotron resonance experiments have been made in antimony (Datars and Vanderkooy, 1964) which gave information about the electron and hole cyclotron masses. The measurements mentioned above have been compared with the theoretical band structure and Fermi surface determined by means of a local pseudopotential approach<sup>6</sup> (Falicov and Lin, 1966). The agreement between experiment and theory seems generally satisfactory regarding the shape and location of the energy surfaces. However, there are still discrepancies between the calculated and measured values of cross sections and for the exact orientations of the energy surfaces in the Brillouin zone. Recently, theoretical calculations of the band structure and Fermi surface of antimony have been carried out by Rose and Schuchardt (1983). They tested four different types of semi-empirical pseudopotentials. Their investigation showed that the Golin type pseudopotential screened by the dielectric function used by Heine and Abarenkov gave better agreement with the available experimental Fermi surface data than that of Falicov and Lin (1966).

Experimental studies of the changes in the Fermi surface cross-sectional areas caused by the application of hydrostatic pressure up to  $14 \text{ kbar}^{-1}$  have been made with three pressure media: fluid helium, frozen helium and frozen kerosene oil. Schirber and O'Sullivan (1969 and 1970) have determined the pressure derivatives of the de Haas-van Alphen frequencies associated with the minimum sections of the hole and electron Fermi surfaces and the maximum section of the hole surface in the trigonal-bisectrix plane. They used the fluid helium phase shift (up to 24 bar) and

the helium freezing (up to 8 kbar) techniques. The solid helium technique has been also used by Tay and Priestly (1970), who studied the change in the minimum section of the hole Fermi surface with pressure up to approximately 2.5 kbar. In the work of Tanuma et al (1970), a pressure of up to 6 kbar was produced in a kerosene-oil mixture at room temperature, with subsequent slow cooling down to below liquid helium temperature, at which the frequency of the quantum oscillations of the susceptibility were measured. Brandt et al (1978) also studied the effect of hydrostatic pressure on pure antimony using the frozen kerosene-oil method in the pressure range from 5-14 kbar by means of the Shubnikov-de Haas effect. Finally, there have been a number of galvanomagnetic studies done on antimony (under pressure) (Brandt et al 1969, Kechin 1968, and Rakmanina et al 1978). These galvanomagnetic experiments yield direct information on the value of the carrier concentration, by a study of the resistivity and the Hall coefficient as a function of magnetic field. These measurements serve as an independent check on the results of the quantum oscillation measurements. The results obtained from the above mentioned experiments will be discussed in chapter 7 in connection with the present measurements.

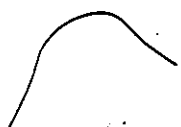
Although all semimetals exhibit strong similarities between their crystal lattices, band structures, and most of the transport properties, the pressure dependence of antimony behaves in an unexpected manner, compared with that of bismuth (Brandt et al, 1969) and arsenic (Schirber and Dyke, 1971). The hydrostatic pressure derivatives of the total number of carriers have been found to be positive in antimony (Brandt et al, 1969, and Rokmanina et al, 1978), but negative in bismuth and arsenic. The ef-



fect of hydrostatic pressure on the atomic positional parameters of antimony, bismuth (Morosin and Schirber, 1969), and arsenic (Morosin and Schirber, 1972) have been determined at room temperature by single crystal x-ray diffraction under hydrostatic pressures of up to 3 kbar. These investigations have revealed that the pressure dependences of the structural parameters of these metals have the same sign. Thus, differences in the behaviour of these materials with pressure can not be attributed to the changes in the positional parameters.

The influence of hydrostatic pressure on the cyclotron effective mass,  $m^*$ , associated with the minimum section of the hole Fermi surface has been studied by Brandt et al (1978) using the Shubnikov-de Haas effect. They have reported four measurements at pressures of 0.4, 4.5, 7.6 and 10.9 kbars. From their tabulated values we have found that  $m^*$  increased by approximately 8% at 4.5 kbar and by 23% at 10.9 kbar from its value at 0.4 kbar. This indicates that  $m^*$  changes rapidly in a nonlinear fashion with pressure. Their tabulated data showed rather poor precision (in determining the cyclotron effective masses) in comparison with the accuracy achieved in the present measurements. A comparison between the two sets of experiments will be discussed in chapter 7.

The present experiments on pure antimony have been carried out to investigate specifically the effect of hydrostatic pressure on the hole Fermi surface anisotropy up to 4.3 kbar, and to extend experimentally the results available on the pressure dependence of a few selected sections of the Fermi surface. On the other hand, on the basis of the present studies of the pressure dependence of the cyclotron effective mass in potassium, we have found that it is possible to obtain a quantitatively



accurate description of the response of the band structure mass to pressure, by choosing a metal with negligible many-body effects, especially the electron-phonon interaction. Antimony satisfies these criteria and we have chosen it to identify separately, the influence of pressure on the band structure mass.

C

## CHAPTER 4

### THEORY, METHODS, AND APPARATUS FOR MEASURING THE DE-HAAS-VAN ALPHEN EFFECT USING THE FIELD MODULATION MEASURING TECHNIQUE

#### 1. Theory of the field modulation technique

The field modulation technique, introduced by Shoenberg and Stiles (1964) was used for studying the de Haas-van Alphen effect under hydrostatic pressure up to 4.5 kbar for pure antimony and potassium. The theory of this measuring technique and how it can be applied to increase the selectivity and sensitivity of the de Haas-van Alphen experiment has been reviewed by Stark and Windmiller (1968) and will be briefly summarized below.

When a small alternating field,  $\tilde{h} \cos \omega t$ , is superimposed on a large dc magnetic field,  $H$ , the time dependence of the total magnetic field is

$$\tilde{H}(t) = \tilde{H} + \tilde{h} \cos \omega t \quad (4-1)$$

Correspondingly, the phase of the de Haas-van Alphen oscillation will change by a small amount,  $\delta\phi_i$ . The time dependence of  $\delta\phi_i$  is

$$\delta\phi_i(t) = \nabla_{\tilde{H}}\phi_i \cdot \tilde{h} \cos \omega t \quad (4-2)$$

The total field  $\tilde{H}(t)$  creates an oscillatory magnetization,  $\tilde{M}_i$ , in a single crystal sample. Referring back to equation (2-20),  $\tilde{M}_i$  can be written in an abbreviated form as

$$\tilde{M}_i(H, \theta, \phi, T) \approx D_i \hat{M}_i(H, \theta, \phi) \sin\{\phi_i + \nabla_{\tilde{H}}\phi_i \cdot \tilde{h} \cos \omega t + \psi_i\} \quad (4-3)$$

In this equation  $\psi_i$  is an additive phase factor and  $D_i \hat{M}_i$  is determined by the Fermi surface geometry near the  $i$ th extremal; it is proportional to the extremal cross sectional area  $S_i$  and inversely proportional to the square root of the Fermi surface curvature  $\partial^2 S_i(\theta, \phi) / \partial k_H^2$ , and is in the direction

$$\begin{aligned} \hat{M}_i &= \frac{\tilde{M}_i}{|\tilde{M}_i|} = \frac{\nabla_{\tilde{H}} \phi_i}{|\nabla_{\tilde{H}} \phi_i|} \\ &= -\hat{H} + \frac{1}{F_i(\theta, \phi)} \frac{\partial F_i(\theta, \phi)}{\partial \theta} \hat{H}_\theta \\ &\quad + \frac{1}{F_i(\theta, \phi) \sin \theta} \frac{\partial F_i(\theta, \phi)}{\partial \phi} \hat{H}_\phi \end{aligned} \quad (4-4)$$

where  $\phi_i = 2\pi F_i(\theta, \phi) / \tilde{H}$  and  $\hat{H}$  is a unit vector along  $H$ . The direction of the oscillatory magnetization,  $\hat{M}_i$ , can often be determined by inspection, since it is often nearly parallel to the direction of the minimum frequency.

Fourier analysis of the time-dependent wave form of equation (4-3) yields (Stark and Windmiller, 1968)

$$\begin{aligned} \tilde{M}_i(t) &= J_0(\delta\phi_i) A_i \hat{M}_i \sin(\phi_i + \psi_i) \\ &\quad + 2 \sum_{n=1}^{\infty} J_n(\delta\phi_i) A_i \hat{M}_i \sin(\phi_i + \psi_i + \frac{n\pi}{2}) \cos(n\omega t) \end{aligned} \quad (4-5)$$

In the field modulation measuring technique for measuring the de Haas-van Alphen effect, the sample is placed at low temperatures in a modulated magnetic field  $\tilde{H} + \tilde{h} \cos \omega t$ , and the voltage induced by the resulting time rate of change of  $\tilde{M}_i(H, \theta, \phi, T)$  in a pick-up coil around the sample is measured. The voltage induced due to the  $i$ th oscillatory magnetization

is given by

$$V_i(t) = \sum_{n=1}^{\infty} n\omega J_n(\delta\phi_i) A_i(\hat{M}_i \cdot \hat{P}) \sin(\phi_i + \psi_i + \frac{n\pi}{2}) \sin(n\omega t) \quad (4-6)$$

Thus,  $V_i(t)$  induced in the pick-up coil contains harmonic contributions of the modulation frequency,  $\omega$ , which are weighted by a Bessel function  $J_n(\delta\phi_i)$  of the first kind of order  $n$ , and by the multiplicative geometrical factor  $\hat{M}_i \cdot \hat{P}$ , where  $\hat{M}_i$  and  $\hat{P}$  are unit vectors along the directions of the  $i$ th oscillatory component and the pick-up coil axis, respectively. At this point it should be noted that for a small modulation field, i.e.  $\delta\phi_i \ll 1$

$$J_n(\delta\phi_i) \approx \delta\phi_i^n = (\nabla_{\vec{H}} \phi_i \cdot \vec{h} \cos \omega t)^n \approx (\hat{M}_i \cdot \hat{h})^n \quad (4-7)$$

The total voltage at the output of the phase-sensitive detector tuned to the  $n$ th harmonic  $n\omega$  is,

$$V_n(H, \theta, \phi, T) = \sum_i n\omega J_n(\delta\phi_i) A_i(H, \theta, \phi, T) (\hat{M}_i \cdot \hat{P}) \times \sin(\phi_i + \psi_i + \frac{n\pi}{2}) \quad (4-8)$$

where the sum is over all extremal cross-sections of the Fermi surface. The dependence of  $V_n(H, \theta, \phi, T)$  on  $J_n(\delta\phi_i)$  and  $\hat{M}_i \cdot \hat{P}$  manifests itself as a

technique for discriminating between different oscillatory components. This is true since  $J_n(\delta\phi_i)$  and  $\hat{M}_i \cdot \hat{P}$  are generally different for different components. Thus, by choosing the direction of the modulation field  $\hat{h}$ , and the axis of the pick-up coil  $\hat{P}$ , such that

$$\hat{M}_i \cdot \hat{P} = \hat{M}_j \cdot \hat{P} = \hat{M}_k \cdot \hat{h} = \hat{M}_L \cdot \hat{h} = 0 \quad (4-9)$$

the de Haas-van Alphen signals corresponding to the  $i, j, k$ , and  $L$  Fermi surface extrema can simultaneously be rejected. The present studies of the Fermi surface and cyclotron effective mass in pure antimony made use of these discrimination techniques.

## 2. De Haas-van Alphen experimental technique and sample preparation

The experimental instrumentation for studying the de Haas-van Alphen effect using the field modulation measuring technique can be grouped into three elements; the large dc magnetic field along the small modulation field, the detection system and the associated detection electronics. The experimental measuring apparatus used for detecting the de Haas-van Alphen effect in antimony and potassium were basically identical. However, in antimony, the dc magnetic field was horizontal and could be rotated uniformly around a vertical axis and was provided by

an electromagnet. In potassium, the dc field was vertical and generated by a superconducting magnet. Modulation and detection coils were constructed for each magnet.

## 2.1 Antimony

### 2.1.a) Methods of frequency discrimination

The major experimental problem in making de Haas-van Alphen measurements in antimony is the simultaneous occurrence of more than one periodic term in the oscillatory magnetization. It is due to the fact that the Fermi surface crosses the fifth Brillouin zone boundaries in a number of regions and is broken up into two sets of nearly ellipsoid closed surfaces of holes and electrons. For a given field direction, each of these closed surfaces will in general give rise to its own oscillatory term. The situation is made complex since the amplitudes of the individual periodic terms are very different; they can differ by many orders of magnitude and only some parts of the oscillatory terms can be observed easily. Thus, for complete, accurate de Haas-van Alphen measurements, it was necessary to use a technique for sorting out and recording separately each oscillatory component.

In the present experiment the de Haas-van Alphen oscillations were studied as a function of the direction of the magnetic field as it was rotated in the trigonal-bisectrix crystallographic plane. In this plane, there are four distinct oscillatory components. Two of them are associated with the principal and nonprincipal electron branches having a tilt angle of approximately  $90^{\circ}$  from the trigonal axis (the tilt angle

is defined by the minimum frequency of the branch). The other two correspond to the principal and nonprincipal hole branches. Their minimum frequencies occur at  $53^\circ$  and  $140^\circ$  from the trigonal axis, respectively. The techniques of discrimination presented in section 1 were used effectively for separating the frequencies coming from various pieces of the Fermi surface.

The electron frequencies were eliminated by arranging to have their oscillatory magnetization vectors,  $\vec{M}_i$ , nearly perpendicular to the axis of the pick-up coil, i.e. by setting the geometrical factor  $\hat{M}_i \cdot \hat{P}$  in equation (4-8) to nearly zero for the electrons but nonzero for the holes. This was done by cutting the crystal along an axis perpendicular to their  $\vec{M}_i$ , i.e. along the trigonal axis of the antimony structure. Thus, the principal and nonprincipal hole frequencies in the entire plane were detected without interference from the presence of the electrons. Next, the nonprincipal hole branch was rejected by utilizing the vector direction of the modulation field  $\vec{h}$ . This was achieved by setting the term  $J_n(\delta\phi_i) \propto \hat{M}_i \cdot \hat{h} \approx 0$  for the nonprincipal branch and nearly a maximum for the other. Thus, the principal hole branch was recorded and studied separately.

Figure 4-1 shows the present experimental geometry used for observing the de Haas-van Alphen effect in pure antimony. The plane of the paper contains the magnetic field direction  $\vec{H}$ , its plane of rotation, the modulation field  $\vec{h}$ , its plane of rotation, the axis of the pick-up coil  $\vec{P}$ , and the projection of the oscillatory magnetization  $\vec{M}_{proj}$ . In the present experimental set-up at least two different oscil-



latory components, in principle, can be rejected simultaneously because  $\tilde{h}$  and  $\tilde{P}$  are confined in the rotation plane of  $\tilde{H}$ . In this plane, the differential change in the de Haas-van Alphen phase  $\delta\phi_i$  can be expressed in terms of the angle  $\theta$  (the angle between  $\tilde{H}$  and  $\tilde{P}$ ) and  $x_i$  (the angle between  $\tilde{H}$  and  $\tilde{h}$ ) as

$$\delta\phi_i = \frac{\tilde{h}}{H} \phi_i \cdot \tilde{h} = \frac{2\pi h F_i(\theta)}{H^2} \times \left\{ F_i(\theta) \frac{dF(\theta)}{d\theta} \sin x_i + \cos x_i \right\} \quad (4-10)$$

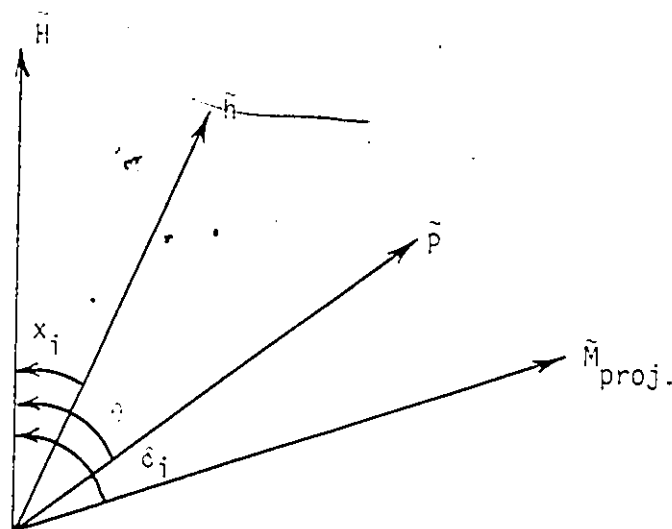


Fig. 4-1 Experimental arrangement

### 2.1.b) Alignment and handling of sample

An antimony single crystal with a purity of 99.999% was cut with its axis along the trigonal crystallographic axis, into a cylindrical form of approximately 4 mm length and 1.5 mm diameter. Antimony used in the present experiment was supplied by the Consolidated Smelting and Mining Company. The presence of the prominent trigonal cleavage plane and binary slip lines on its surface enabled us to determine easily the crystallographic directions; the trigonal axis is orthogonal to the cleavage plane, the binary axis is parallel to each slip line, and the bisectrix axis bisects two adjacent binary directions. The sample was etched with a dilute solution of nitric and hydrofluoric acids, washed with distilled water, and then fitted precisely and glued carefully inside a cylindrical thin walled sample holder. The sample holder was made from Kel-F to fit closely into the experimental pick-up coil. Under a microscope the crystal was oriented in the trigonal-bisectrix crystallographic plane, in which the trigonal axis was aligned horizontally (i.e. along the pick-up coil axis), while the binary axis was aligned vertically. After a satisfactory alignment had been achieved, the sample holder was glued uniformly with a thin layer of General Electric Glyptal Glue to ensure proper rigidity of the detection system and avoid any relative movement between the sample and detection coils which could lead to alignment change, particularly under the application of high pressure. Furthermore, x-ray photographs were taken, primarily to determine more precisely the crystal orientation. The results however, were only

consistent within 4 or 5°, which was not sufficiently precise. Therefore, the final, most accurate alignment was determined from the symmetry of the de Haas-van Alphen frequencies. The principal and non-principal hole branches intersect at the trigonal axis to form a single de Haas-van Alphen oscillation. This intersection point was used as a sensitive indicator of the trigonal direction.

### 2.1.c) Detection system and generation of the modulation and dc fields

Experiments were performed in dc magnetic fields up to 1.9 Tesla and a temperature down to 1.2 K. The dc magnetic field was provided by an electromagnet with a gap of 5.08 cm. The magnetic field intensity was determined to an accuracy of < .2% with a Gaussmeter which was calibrated by nuclear magnetic resonance up to approximately 1 Tesla. An electronic attachment for the Gaussmeter gave an electric signal at 1 kilogauss intervals of magnetic field. This signal pulse was added in series with the de Haas-van Alphen signal and the resulting pips were used as accurate field markers. Measurements were performed as a function of magnetic field intensity and as a function of the direction of the magnetic field while keeping its magnitude fixed. A motor and chain drive was used to rotate the magnet uniformly in a horizontal plane.

Figure 4-2 presents schematically the modulation and pick-up coils assembly for the field modulation apparatus. Two sets of modulation coils were constructed and used to generate x and y components of the modulation field. The direction of the resultant field could be adjusted along any desired direction by varying the relative amplitude and phase of an ac current passing through each set. Each pair had 200 turns of

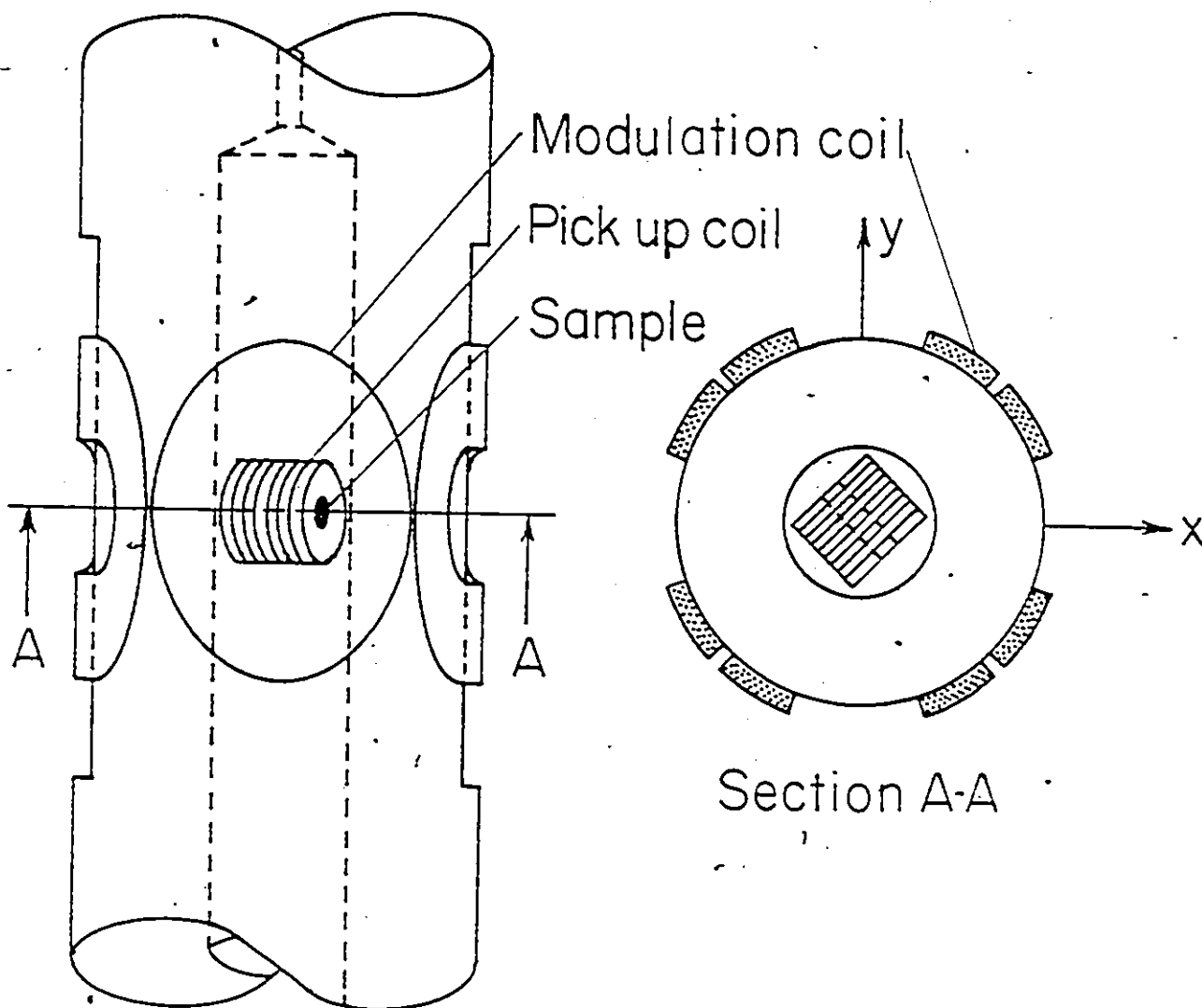


Figure 4-2 Modulation and pick-up coils assembly for the field modulation apparatus.

number 30 copper wire and was fixed rigidly in an orthogonal configuration on the outside of the pressure cell. It should be noted that, mechanically firm and regular winding coils are of critical importance to obtain optimum signal-to-noise ratio. Thus, considerable care was taken in constructing the coils by carefully winding and gluing them layer by layer with General Electric Glyptal Glue to minimize any possible vibrations of individual turns which can generate a great deal of noise.

The de Haas-van Alphen oscillations were detected by measuring in a pick-coil wound around the sample the voltage induced by the time rate of change of the sample's magnetization. The detection coils consisted of a pick-up coil of  $N_1$  turns and radius  $R_1$  closely coupled to the sample, and a compensation coil of  $N_2$  turns and radius  $R_2$ . The pick-up and compensation coils were connected in series opposition with  $N_1 + N_2 = 1000$  turns of number 45 copper wire,  $N_1 > N_2$ ,  $R_1 < R_2$  and  $R_1^2 N_1 = R_2^2 N_2$ . In constructing the coils care was taken to avoid any irregularity in windings. Furthermore, proper rigidity of the design was achieved by gluing them uniformly layer by layer using General Electric Glyptal Glue. The coils were mounted firmly, concentrically and properly compensated. The leads of the coils were tightly twisted together, well shielded and made as short as possible, to minimize further pick-up noise.

## 2.2 Potassium

### 2.2.a) Sample preparation

Accurate amplitude measurements are obtainable if the sample satisfies the criteria of sufficiently high purity and of being almost strain free. Thus, considerable care was required in preparation and handling of a sample. This is particularly important for delicate metals such as the alkalis because of their extreme softness and their chemical activity with the atmospheric environment and water. Indeed, if the crystal is composed of two or more subcrystals, which can be possible for samples which have not been carefully handled, the de Haas-van Alphen amplitude will be reduced. In addition, if the purity of the crystal is not sufficiently high, the oscillatory structure will be appreciably diminished.

Potassium used in the present experiment was 99.97% pure source material obtained from Mine Safety Appliances, Callery, Pennsylvania. Spherical single crystals of pure potassium were grown under dry degassed mineral oil. Single crystals were left under the oil which was allowed to cool slowly from just above the melting point ( $62^{\circ}\text{C}$ ) to room temperature over a period of several hours. A sample of unknown random orientation and a diameter of approximately 2 mm was chosen from the crystals that were made. Excess oil on the sample surface was drained by capillary action using soft paper tissue. At this point, the sample was shiny, visually uniform and had a very thin film of oil on its surface. The sample holder was then fitted precisely inside the pick-up coil for insertion in the pressure cell. Finally, the pressure cell was close-

ly fitted into the cryostat for subsequent pressurization. Air in the cell was replaced immediately by helium gas to protect the sample from oxidation.

2.2.b) Detection system and generation of the modulation and dc field

The Westinghouse superconducting magnet system, used in investigating the influence of hydrostatic pressure on the cyclotron effective mass of potassium, has been described by Moss (1968). It generates a magnetic field up to 5.54 Tesla that is uniform to 1 part in  $10^4$  in 1.3 cm. sphere. Since potassium has a de Haas-van Alphen phase,  $2\pi F/H$ , of about  $2 \times 10^4$  at 5.54 Tesla, the period of the oscillation at this field,  $H^2/F$ , is about  $17 \times 10^{-4}$  Tesla. This small period imposes strict requirements on the homogeneity of the magnetic field over the volume of the sample. A homogeneity better than a few parts in  $10^4$  is required in order not to smear out the oscillation appreciably. If different parts of the crystal experience slightly different magnetic fields, the signal will be shifted in phase from one part to the next with a resultant signal reduced in amplitude. This problem was avoided by placing the sample accurately at the center of uniformity of the magnetic field.

The pressure cell along with the detection and modulation coils used in the present experiment are shown schematically in figure 4-3. The detection coils consisted of two colinear coils; pick-up and compensation, each having 600 turns of number 40 copper wire. The induced voltage in the pick-up coil was detected at the second harmonic of the modulation frequency. The modulation coil consisted of two layers with a total of 280 turns of number 34 copper wire wound directly on the exterior of the pressure coil.

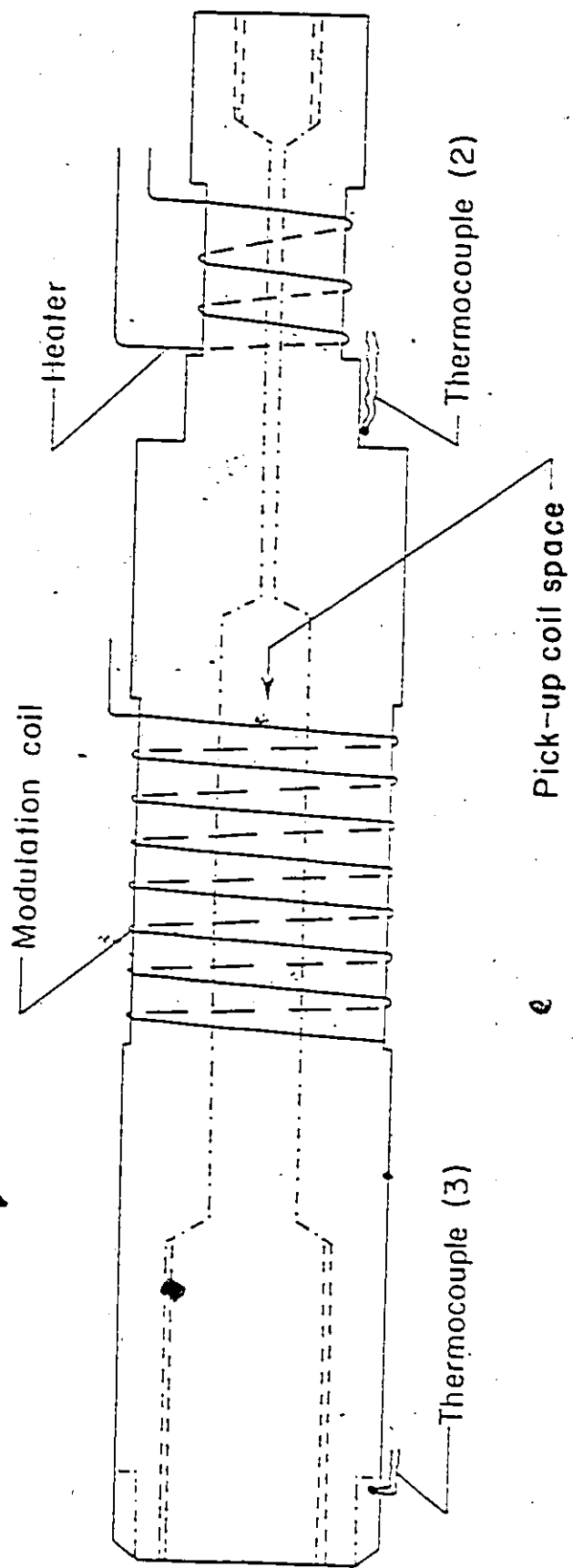


Figure 4-3 Schematic diagram of the high pressure cell and the dHVA detection system.



Accurate amplitude measurements are possible only if the modulation field  $\tilde{h}$ , penetrates homogeneously into the sample. For reasons of signal-to-noise ratio it was not possible to use modulation frequencies below 8 Hertz. The use of a low modulation frequency helped avoid (to some extent) skin depth problems in order to make the measured de Haas-van Alphen amplitude representative of the bulk of the sample. If the skin depth is smaller than the sample dimension, then the Bessel function  $J_n(\delta\phi_i)$  (it is a function of the phase change  $\delta\phi_i = \pi r h F / H^2$  where  $F$  is the de Haas-van Alphen frequency, and  $h$  is the amplitude of the modulation field applied along the direction of the dc magnetic field) that enters the expression for the measured de Haas-van Alphen amplitudes will not have the same value of  $h$  in all parts of the sample and consequently the measured de Haas-van Alphen amplitude will be reduced and have an extra field dependence which can introduce error in the results.

### 2.3 Field modulation experimental apparatus

Figure 4-4 shows schematically the field modulation experimental apparatus used to observe the de Haas-van Alphen effect. The de Haas-van Alphen signal from the pick-up coil, which contains in it all the harmonic contributions of the modulation frequency  $\omega$ , was fed into a Princeton Applied Research Corporation, model 124A lock-in amplifier. The lock-in amplifier electronic circuit and the principle of operation of this circuit will be stated briefly. Essentially the electronic circuit consists of three major elements; the signal channel, the reference channel, and the synchronous detector (or phase sensitive detector). The signal

channel amplifies the input signal through a model 116 differential pre-amplifier which was operated in a transformer coupled mode for optimum low noise performance. The amplified signal was then fed into a selective amplifier which functions as a variable Q filter. It was operated in a band pass mode, and tuned to the second harmonic  $2\omega$ . The sharpness of the selective amplifier was achieved by selecting the appropriate Q value. In this stage, much of the noise and odd harmonics were rejected by filtering out all but the band containing the wanted signal before passing it to the synchronous detector.

The reference signal at the modulation frequency  $\omega$ , was sent to the reference channel from an oscillator. Essentially, the reference channel is composed of two elements; a voltage controlled oscillator, (VCO), and phase controls. The VCO automatically phase-locks to the second harmonic of the reference signal and drives the synchronous detector so that the output from the signal and reference channels is properly synchronized. The RC filter that follows the synchronous detector, was used to optimize the signal-to-noise ratio. This signal from the output of the lock-in amplifier was then plotted on a chart recorder versus angle for rotation diagrams or versus magnetic field intensity, for field sweeps.

The two orthogonal modulation coils, used in the de Haas-van Alphen measurements of antimony, were driven at 517 Hertz. These signals were provided by two identical ac power amplifiers through an oscillator. The oscillator output was split into three simultaneous outputs; one of them was fed to the reference channel of the lock-in amplifier as mentioned above, while the other two were passed through the ac power amplifiers stabilized to compensate for gain changes of the oscillator output voltage.

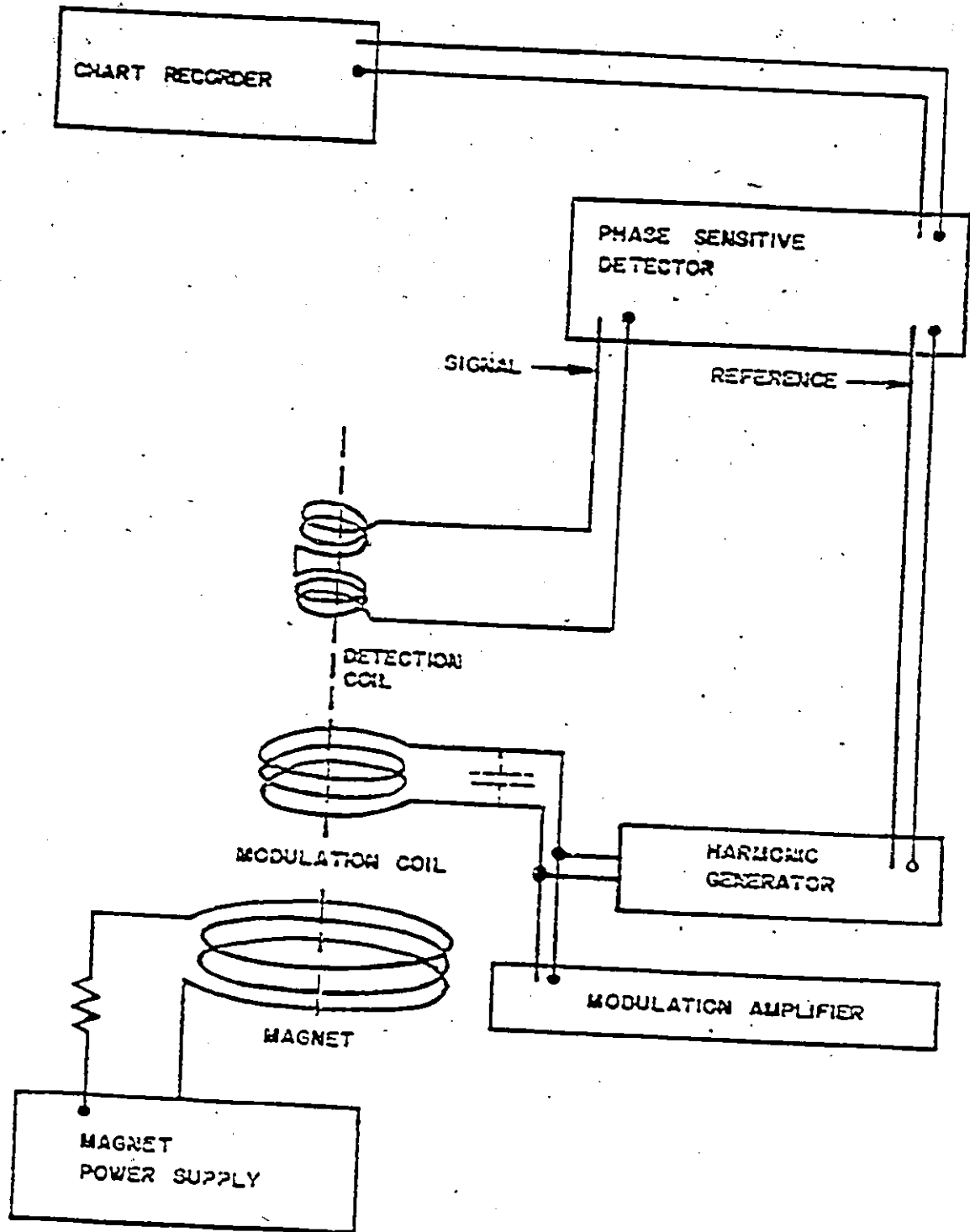


Figure 4-4 Block diagram for the field modulation apparatus.

### 3. The solid helium high pressure technique






#### 3.1. High pressure system

Pressures of up to 5 kbar were obtained using a Harwood Engineering Portable Pressure Generating system. It is presented schematically in figure 4-5. Compressed helium gas, that was used as the pressure transmitting medium, was transmitted from the pressure generating system to the pressure cell via a stainless steel capillary line (3.2 mm OD x 0.4 mm ID). The pressure system consists of a two stage gas compressor; a 1:1 gas to oil separator (INT.1) and a 14.5:1 gas to oil intensifier (INT.2). The separator acts as a charge pump for the intensifier. The principle of operation of the high pressure system was described by Slavin and Datars (1974) and Altounian and Datars (1980), and will only be summarized briefly here.

A commercially bottled supply of helium gas was used to produce a charge pressure of about 0.08 kbar. The air compressor provides a continuous air pressure of the air to oil booster pump (P1). Pressure gauges G1 and GA are provided to record the oil and air pressures, respectively. The air pressure can be pumped to a maximum of 1.38 kbar. This pressure is transmitted to the charge helium gas through the 1:1 gas to oil separator. Higher pressures, up to 5 kbar, were generated in a 14.5:1 gas to oil intensifier. The maximum pressure obtainable from the pressure system is 7 kbar. The pressure in the cell is determined with a manganin resistance gauge MG. The details of the constituents of the pressure apparatus are given in the caption of figure 4-5.

The pressure cell and the high pressure electrical feedthrough are

Key to Figure 4-5

-  manually operated needle valve
-  filter
-  pressure gauge
-  check valve:
-  pressure release rupture valve
- FH - oil filter
- AS - air supply.
- FA - air filter
- AR - air regulator
- GA - air pressure gauge
- AT - air throttle used to regulate pumping rate of intensifier
- Pl - air-to-oil booster pump
- G1 - oil Heise gauge on front panel
- GH - helium pressure gauge at the helium cylinder
- MG - manganin pressure gauge
- INT.1 One-to-one oil to gas intensifier
- INT.2 14.5 to 1 oil to gas intensifier
- SV High pressure safety valve.

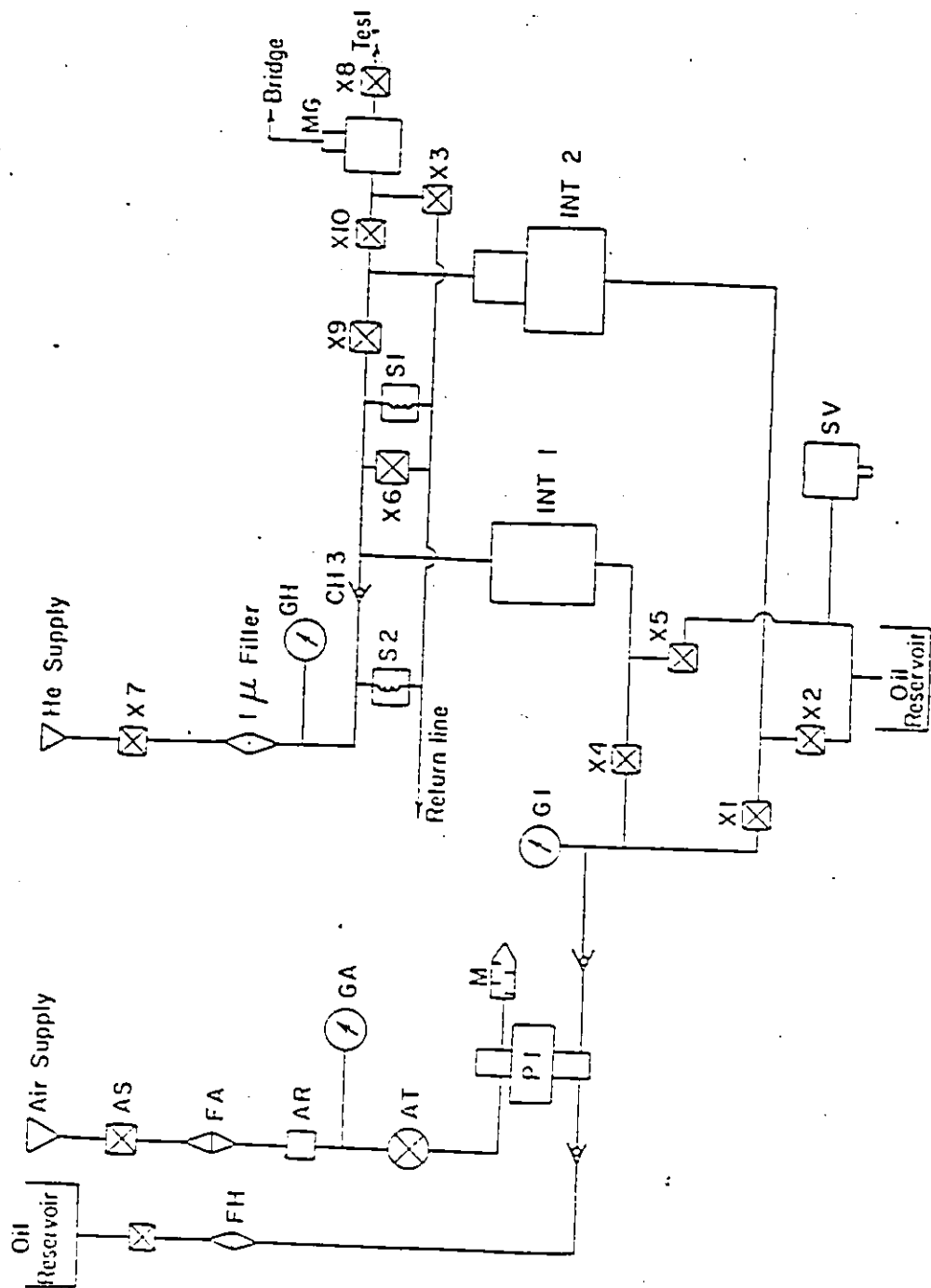


Figure 4-5 Block diagram for the high pressure system.

"

presented in figures 4-3 and 4-5, respectively. The pressure cell was made of beryllium copper heat treated (2 hrs and 25 minutes at 315°C) to a Rockwell hardness of RC 42. The plug and high pressure electrical feedthrough assembly were made of 316 stainless steel (Schirber and Shanfeld, 1968). They were made to fit precisely into the pressure cell. The plug was sealed against gas leaks by tightening a beryllium copper screw inside the central lower end of the pressure cell. The screw also provided a solid support for the plug. The high pressure seal between the feedthrough and the plug was made with a Kel-F washer immersed in heavy silicone oil which provided a tight, good seal up to approximately 5 kbar. The Kel-F washer was also used for insulating the electrical feedthrough and the plug.

### 3.2 Method of applying hydrostatic pressure at liquid helium temperature

All the measurements were performed under hydrostatic pressures using the helium freezing method, and at low temperatures necessary to observe the de Haas-van Alphen effect. At these temperatures,  $\leq 4.2$  K, the helium gas solidifies at pressures above 25 bars. Since all experiments were carried out at pressures greater than 25 bars, solid helium was used for transmitting of pressure to a specimen. The technique of applying hydrostatic pressure consists essentially of generating the desired pressure in helium gas, as explained in section 4-1, and maintaining this pressure as the helium solidifies slowly from the bottom of the pressure cell towards its top. With the desired pressure of helium gas on the sample, the temperature of the cell at this stage was between 80 - 100 K. The pressure cell was then cooled to liquid helium temperature, resulting in freezing of the helium, about the sample. The cooling process was performed slowly

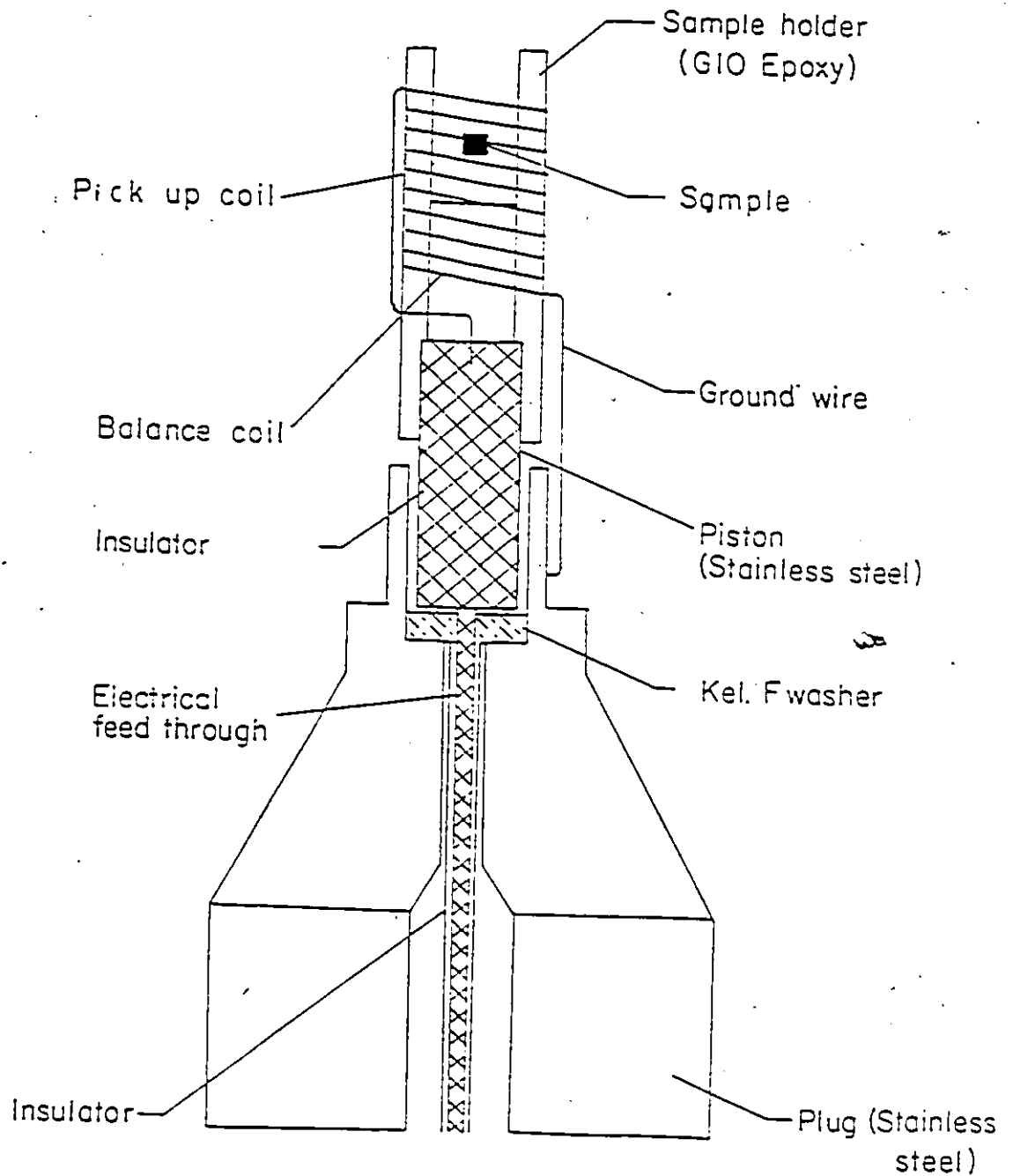


Figure 4-6 Schematic diagram of the high pressure electrical feed-through and dHvA pick-up coil.



and controlled so that helium solidified from the bottom of the cell towards the capillary inlet at the top. This was achieved by heating the top of the cell while transferring liquid helium to the vicinity of the bottom of the cell. In this way the deviation from hydrostaticity was greatly minimized (Spain and Segall, 1971). The temperatures of both ends of the cell were continuously monitored with thermocouples during cooling and a temperature gradient of about 3 K was maintained. Solidification of the helium was completed at some freezing temperature  $T_m$  and pressure  $P_m$ , figure 4-7 (Spain and Segall, 1971), further cooling occurring at essentially constant volume. This resulted in a decrease in the freezing pressure  $P_m$  due to contraction of the solid helium. Loss in pressure in the solid helium upon cooling due to contraction was estimated from the data of Spain and Segall (1971). From their measurements, a plot of the pressure loss,  $(P_m - P_0)/P_0$  against the freezing pressure  $P_m$  was obtained, and was used to find the final pressure  $P_0$  on the sample. For example, applied pressures of 1 and 5 kbar were corrected to be 0.95 and 4.63 kbar, respectively.

The freezing pressure  $P_m$  was read by the manganin resistance gauge supplied and calibrated by Harwood Engineering. A test of this gauge calibration against a Bourdon type pressure gauge showed consistency to within 2% up to 5 kbar. Measurement of the pressure derivative,  $dT_c/dP$  of a tin sample, over the pressure range from 0 - 11 kbar was performed, in order to check that the determined  $P_0$  in the cell was correct. A linear fit to  $T_c$  against  $P$  gave a value of  $dT_c/dP$  of  $(4.63 \pm 0.10) \times 10^{-2} \text{ kbar}^{-1}$ , which was in agreement with the value  $(4.73 \pm 0.10) \times 10^{-2} \text{ K kbar}^{-1}$  obtained by Jennings and Swenson (1958) over the same pressure range. Another test of the esti-

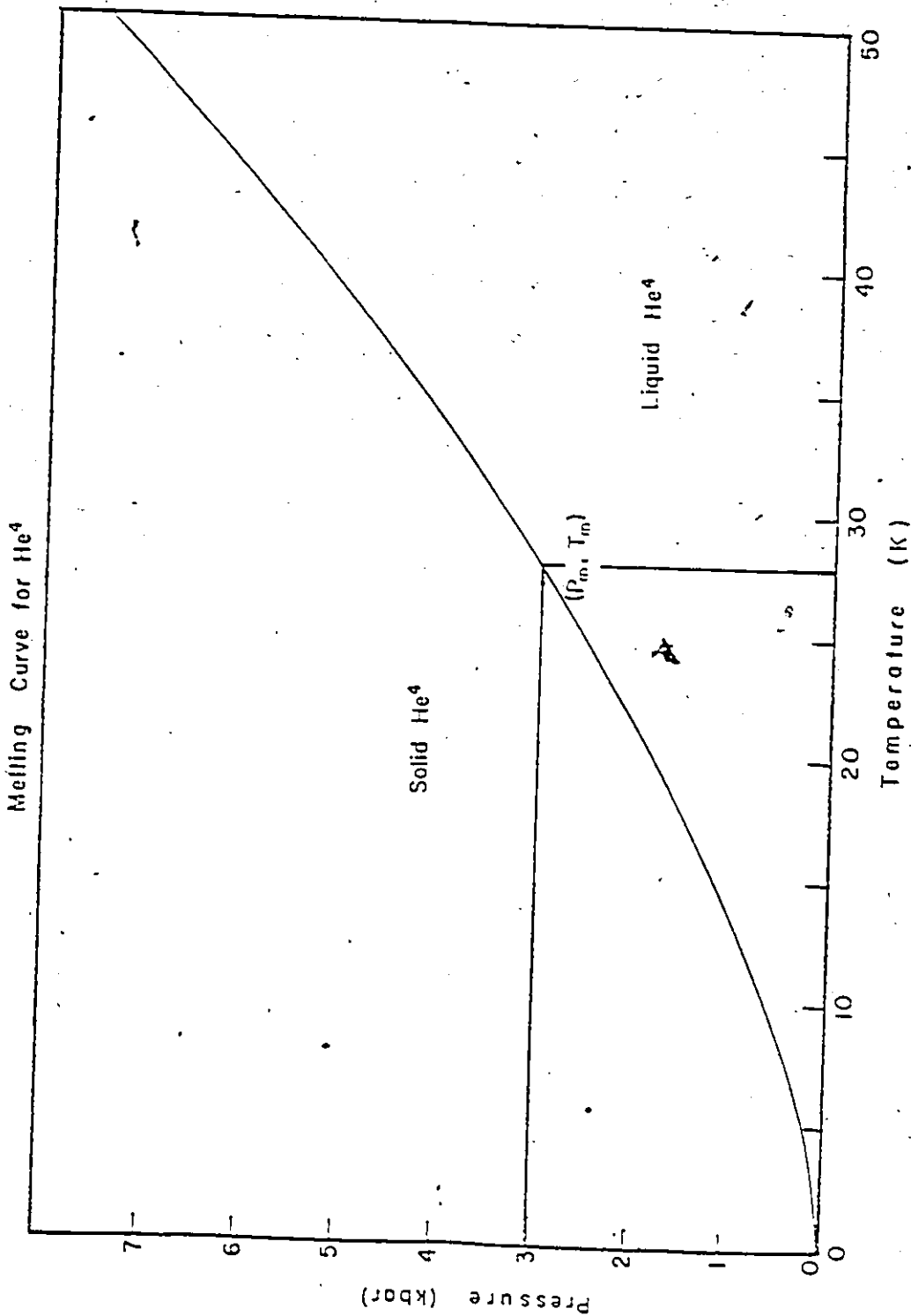


Figure 4-7  $P_m$ - $T_m$  diagram for He<sup>4</sup>

estimated final pressure  $P_0$  was also made by measuring the pressure dependence of the ratio of the belly to neck frequencies,  $f_B/f_N$ , for copper in the  $\langle 111 \rangle$  direction, using the de Haas-van Alphen effect. This yielded a value of  $(\alpha_N - \alpha_B)$  of  $(15.3 \pm 0.4) \times 10^{-4} \text{ kbar}^{-1}$  over the pressure range from 0.5 kbar. Here  $\alpha_N$  and  $\alpha_B$  are the logarithmic pressure derivatives of the neck and belly de Haas-van Alphen frequencies, respectively. The pressure dependence of  $f_B/f_N$  is accurately known from the low pressure work of Tempelton (1974), using a fluid helium phase shift method. From his results, it was found that  $\alpha_N - \alpha_B = (15.6 \pm 0.5) \times 10^{-4} \text{ kbar}^{-1}$  which agrees with the estimated value quoted above. It should be noted that  $(\alpha_N - \alpha_B)$  was expected to be constant up to  $\approx 40 \text{ kbar}$  (Davis *et al.*, 1968). Based on the above calibration results, a maximum uncertainty in the pressure reading was less than 3%.

## CHAPTER 5

### EXPERIMENTAL STUDIES OF THE INFLUENCE OF HYDROSTATIC PRESSURE ON THE ELECTRON CYCLOTRON EFFECTIVE MASS IN POTASSIUM

#### I. Introduction

Precise measurement of the cyclotron effective mass is possible from the temperature dependence of the amplitude of the de Haas-van Alphen (dHvA) effect (Gold 1968). This is particularly suitable for potassium with only one dHvA oscillation (Shoenberg and Stiles 1964). The measurement is of interest because the cyclotron mass is the band mass renormalized by many-body effects, especially the electron-phonon interaction. The application of pressure changes the magnitude of the terms and allows one to test many-body and band theories. In this chapter we provide precise experimental measurements of the hydrostatic pressure dependence of the cyclotron effective mass,  $m^*$ , in pure potassium up to 4.4 kbar. In addition, accurate determination of  $m^*$  at standard atmospheric pressure was obtained which has been used recently by Dunifer *et al* (1984) in the analysis of spin waves in potassium. The cyclotron effective mass was derived from the temperature dependence of the dHvA oscillation amplitude. Sodium was studied previously for the pressure dependence of the cyclotron effective mass by Elliott and Datars (1982). They explained their measurements in terms of changes in the band mass and the electron-phonon mass enhancement parameter with pressure. This was followed by calculations of the electron quasiparticle mass for the alkali metals that took into account

the volume dependence of the band mass as well as electron-phonon and electron-electron mass enhancement parameters (Leavens et al 1983). The calculations made use of the volume dependence of the band mass determined by Wilk et al (1979). The inclusion of the three terms gave reasonable agreement with the measured pressure dependence of the mass in the limit of standard atmospheric pressure. We discuss first the variations of the electron-phonon mass enhancement with pressure since it is the largest term. Contributions to the pressure dependence of the effective mass from the band mass and electron-electron interaction are also considered. Finally, we compare our results with predictions of the theory of Leavens et al (1983).

## 2. Experimental results and analysis

The electron cyclotron effective mass measurements of randomly oriented pure potassium samples were performed using the field modulation measuring technique described in chapter 4. The induced voltage in the pick-up coil was detected at the second harmonic ( $2\omega$ ) of the 8 Hz modulation frequency. Referring back to equation (4.8), it is clear that the de Haas-van Alphen signal associated with the second harmonic after phase sensitive detection can be expressed as

$$V(2\omega) = 2\omega A(T, H, T_D) J_2(\delta\phi) \sin\left(\frac{2\pi F}{H} + \psi\right) \quad (5.1)$$

where  $A(T, H, T_D)$  is the dHvA amplitude and  $\psi$  is a phase constant. Here,  $J_2$ , the second order Bessel function, is a function of the phase change  $\delta\phi = 2\pi h F / H^2$  where  $F$  is the dHvA frequency and  $h$  is the amplitude of the modulating field applied along the direction of the dc magnetic field  $H$ . The amplitude of the modulating field was chosen so that  $J_2$  was at its first maximum.

Experimental measurements of the cyclotron effective mass derived from the temperature dependence of the dHvA amplitude were performed with four samples at the highest available field of 5.54 T provided by a Westinghouse superconducting magnet. The temperature was controlled and measured between 1.2 and 2.1 K by regulating the vapour pressure of helium with a precision pressure gauge. The accuracy of the gauge was checked by measuring the vapour pressure at the  $\lambda$  point of helium. The measurement corresponded to a temperature that was within 0.15% of the accepted value of 2.172 K.

The expression of the de Haas-van Alphen amplitude (equation 2.20) may be rewritten as

$$A(T, H, T_D) = (D(H)T/\sqrt{H}) \exp(-14.69 m^* T_D / m_0 H) \cos(\pi g m^* / 2 m_0) \times (\sinh 14.69 m^* T / m_0 H)^{-1} \quad (5.2)$$

where  $D(H)$  is the maximum value of the amplitude which can only be realized at  $T=0$  for sharp Landau levels,  $T_D$  is the Dingle temperature and  $g$  is the spin splitting factor. In the case of potassium for which  $(m^*/m_0) > 1$ , the approximation  $\sinh(x) = e^x/2$  can be made with an error of less than 0.25% if  $x \geq 3$ . Therefore a plot of the dHVA amplitude versus temperature  $T$  according to

$$\ln(A/T) = \ln(A_0) - (14.69 m^* T / m_0 H) \quad (5.3)$$

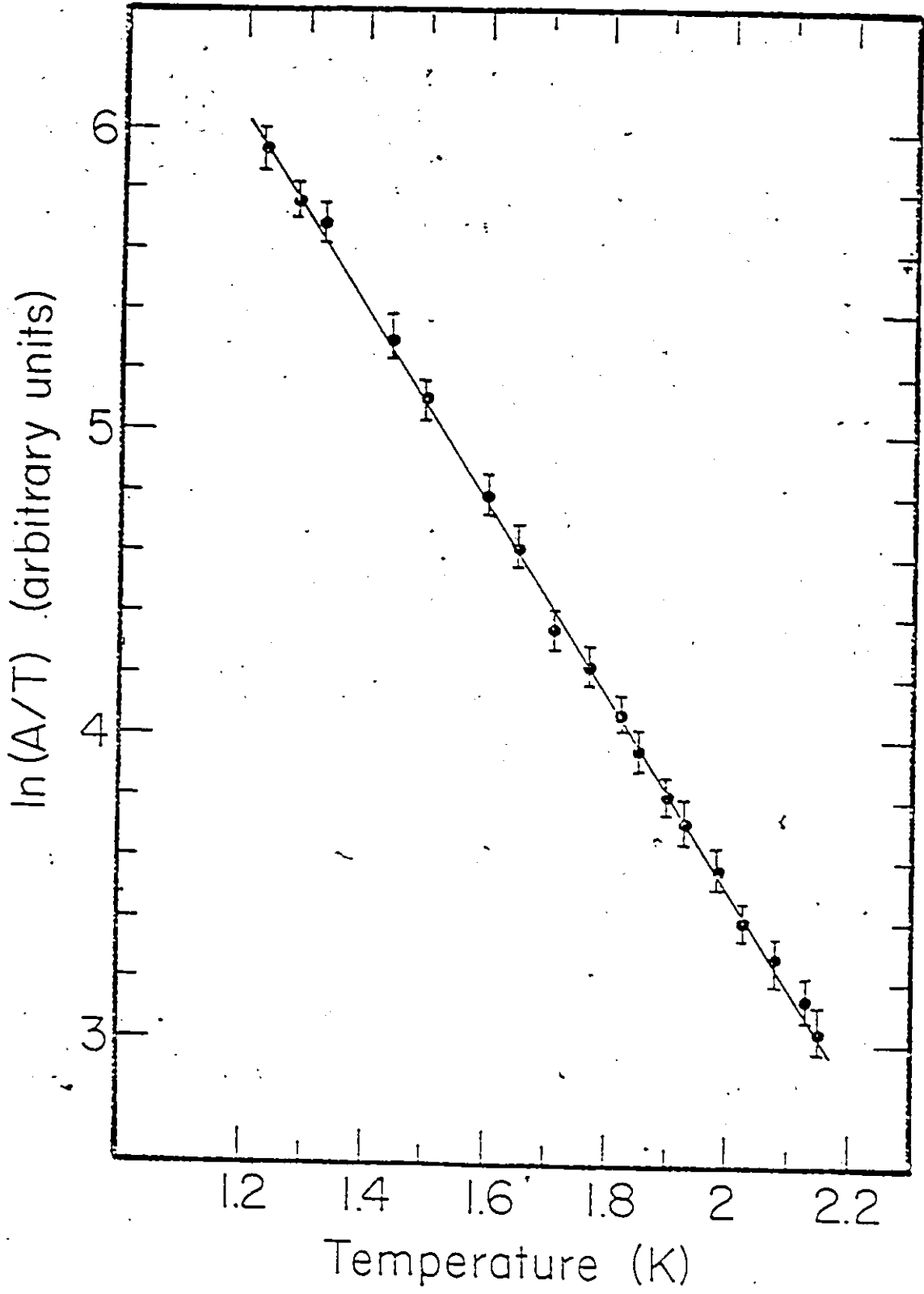
gives a straight line with a slope of  $(-14.69 m^* / m_0 H)$ , where  $(m^*/m_0)$  is the cyclotron effective mass normalized to the free electron mass. The slope was determined by the method of least squares. An example of a least squares fit to all data points of  $\ln(A/T)$  versus  $T$  for a magnetic field of 5.54 T and pressure of 2.56 kbar is shown in figure 5-1 with  $m^* = (1.191 \pm 0.007)m_0$ .

The measured hydrostatic pressure dependence of the cyclotron effective mass for three potassium samples in the pressure range 0 - 4.4 kbar is shown in Figure 5-2. The weighted least squares fit to all data points yields

$$1/m^* (dm^*/dP) = - (0.71 \pm 0.12) \times 10^{-2} \text{ kbar}^{-1}$$

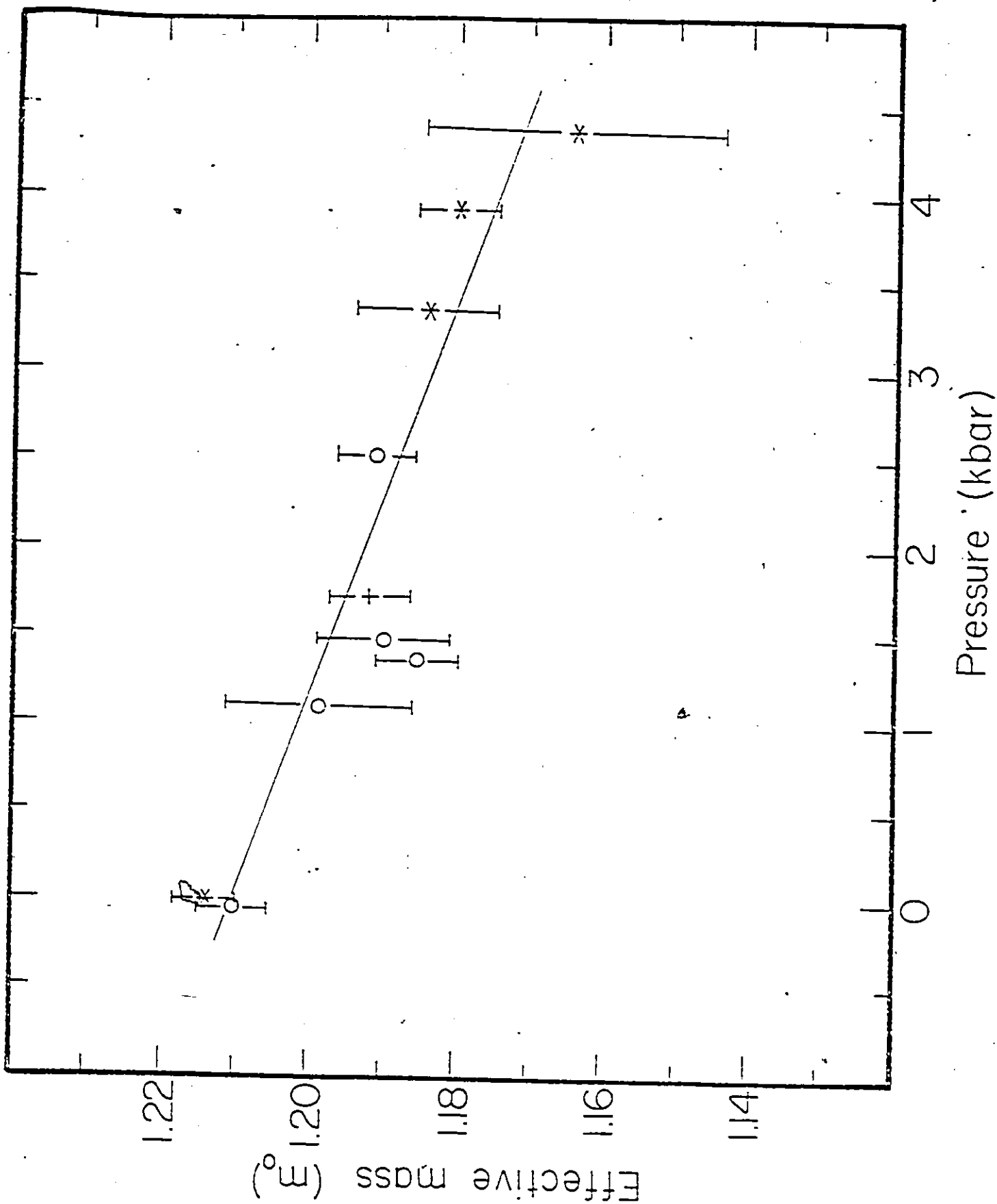
Figure 5-1 Logarithmic plot for the determination of the cyclotron effective mass in potassium at a pressure of 2.56 kbar. The line is a linear least squares fit to the data points.





C

Figure 5-2 A plot of the cyclotron effective mass ( $m^*/m_0$ ) of potassium versus pressure up to 4.4 kbar. The line is a least squares linear fit. The different symbols refer to different samples.



The intercept of  $m^*$  versus  $P$  graph corresponds to a standard atmospheric pressure (1 bar) mass of  $(1.209 \pm 0.003) m_0$ . The cyclotron effective mass of two samples was measured at a pressure of 1 bar. The measured values were  $(1.210 \pm 0.005) m_0$  and  $(1.214 \pm 0.004) m_0$ . An average of these two values along with the intercept at  $P = 1$  bar gives

$$m^* = (1.211 \pm 0.005) m_0 .$$

This value was used by Dunifer et al (1984) to analyze spin waves in potassium.

### 3. Discussion

A comparison of values of the cyclotron effective mass at standard atmospheric pressure measured by various workers using different methods is given in Table 5-1. Values by Grimes and Kip (1963) and Walsh (unpublished) were obtained by Azbel-Kaner cyclotron resonance. Elliott and Datars (1982) and Knecht (1975) measured the cyclotron mass in pure potassium from the dHvA effect. Paul and Springford (1978) also used the dHvA effect but measured the mass in samples of potassium alloyed with 0.147% and 0.327% sodium. The effective mass from a specific heat measurement was obtained by Martin (1970).

Our present result is in agreement with other measurements within combined experimental errors except for the mass reported by Paul and Springford (1978). The difference between our result and Paul and Springford's value might not be significant because they are just outside ~~Quoted~~ experimental errors. However, there are considerable differences between the two experiments: different modulation frequencies,

Table 5-1

Reported values of the electron cyclotron mass of potassium at standard atmospheric pressures.

Source	$m^*/m_0$
Grimes and Kip (1963)	$1.21 \pm 0.02$
Walsh (unpublished)	$1.217 \pm 0.002$
Knecht (1975)	$1.22 \pm 0.02$
Elliott and Datars (1982) <sup>2</sup>	$1.215 \pm 0.005$
Paul and Springford (1978)	$1.230 \pm 0.013$
Martin (1975)	$1.24 \pm 0.05$
Present work	$1.211 \pm 0.005$

potassium alloy and pure potassium samples, an attempt to measure anisotropy in their work, a weighted average of all measurements made for a large number of orbits over the Fermi surface in their work and an average of several standard atmospheric pressure measurements with randomly oriented samples in our work. The last difference may be the most important because their weighted average is higher by approximately 0.4% than the average of the values that are shown. Thus, an unweighted average of their mass measurements yields a value closer to, and not outside experimental error from, the value found in the present work.

The electron quasiparticle mass of a simple metal can be expressed as

$$m^* = m_b(1 + \lambda_{ep})(1 + \lambda_{ee}) \quad (5.3)$$

where  $m_b$ ,  $\lambda_{ep}$  and  $\lambda_{ee}$  are band structure mass, electron-phonon and electron-electron mass renormalization parameters, respectively. Since potassium has almost a free electron nature, the band structure mass,  $m_b$ , is expected to be almost the same as the free electron mass. A calculation by Timbie and White (1970) indicates that  $m_b = 1.01 m_0$  in potassium and experimental measurements of the spin splitting factor  $g$  made by Knecht (1975) reveals that  $m_b$  is about  $1.0 m_0$ . The contribution from the electron-electron interaction is also small according to Rice (1968) who pointed out that Coulomb shifts in the energy spectrum of a single particle are small and nearly constant yielding a mass change of the order of 5% (i.e.  $\lambda_{ee} = 0.06$ ). On the other hand, the contribution due to the electron-phonon interaction has a greater influence on the magnitude of the cyclotron effective mass. The appropriate orbital averages of the local interaction parameter  $\lambda_{ep}$  in potassium was estimated at the three principal symmetry directions  $\langle 100 \rangle$ ,  $\langle 110 \rangle$  and  $\langle 111 \rangle$  to be 0.135, 0.134 and 0.135 by Paul and Springford (1978). Their estimation was based on calculated values of the electron-phonon mass enhancement parameters derived by Leavens and Carbotte (1973). The orbital average of the local interaction parameter  $\lambda_{ep}$  is particularly suitable for dHvA measurements, since dHvA gives a value of  $m^*$  which is averaged over an extremal orbit. The values of  $\lambda_{ep} = 0.135$ ,  $\lambda_{ee} = 0.06$  and  $m_b = 1.01$  in equation (5.3) predict  $m^* = 1.215 m_0$  which is in good agreement with our measured value.

We now examine to what extent the changes of many body effects and band structure effects with pressure influence the variation of the cyclotron effective mass as a function of pressure by first considering

the pressure dependence of the electron-phonon mass enhancement parameter. Studies by Trofimenkoff and Carbotte (1970) have demonstrated that, when a metal is subjected to a hydrostatic pressure, the electron-phonon enhancement ( $\lambda_{ep}$ ) decreases significantly as a result of general stiffening of the lattice. The parameter  $\lambda_{ep}$  is related to the  $\alpha^2(\omega)F(\omega)$  spectrum by

$$\lambda_{ep} = 2 \int_0^{\infty} \alpha^2(\omega)F(\omega)/\omega \, d\omega \quad (5.4)$$

where  $F(\omega)$  is the phonon density of states as a function of energy and  $\alpha^2(\omega)$  is the electron-phonon coupling parameter. The expression derived by Trofimenkoff and Carbotte (1970) for the pressure dependence of  $\alpha^2(\omega)F(\omega)$  has the form

$$\alpha^2(\beta\omega)F(\beta\omega) = (B/\beta^2)\alpha_0^2(\omega)F_0(\omega) \quad (5.5)$$

where  $\beta$  is related to the volume change under pressure and the average Grüneisen parameter  $\gamma_G$  by

$$\beta = 1 - (\Delta V/V_0)\gamma_G \quad (5.6)$$

$B$  is a measure of the change of the pseudopotential with pressure and is assumed to be 1 since deviation from this value is calculated to be small. The electron-phonon mass renormalization parameter at zero pressure,  $\lambda_0$ , is taken to be 0.135 in this discussion (i.e. the average value estimated by Paul and Springford 1978). It should be noted, however, that this parameter is insignificantly affected by crystal orientation (Paul and Springford 1978 and Trofimenkoff and Carbotte 1970). From

equations (5.4) and (5.5) the electron-phonon renormalization parameter at finite pressure is expressed in terms of its value at zero pressure,  $\lambda_0$ , by

$$\lambda_{ep} = \lambda_0 / \beta^2 \quad (5.7)$$

The pressure derivative of the cyclotron effective mass is

$$(1/m^*) dm^*/dp = (1/(1+\lambda_{ep})) d\lambda_{ep}/dP \quad (5.8)$$

To calculate  $d\lambda_{ep}/dP$ , we need to know the pressure dependences of the volume  $V$  and  $\gamma_G$ . The variation of the volume  $V$  in potassium up to 10 kbar from 4.2 to 300 K has been determined recently by Anderson and Swenson (1983) using the piston-displacement method. They represented their volume-pressure results with a reduced equation of state (second order Murnaghan relation) which is based on a Taylor's expansion of the isothermal bulk modulus ( $B_T$ ) in terms of pressure,

$$B_T(P,T) = B_0(T) \{1 + B'_0(P/B_0) + 1/2 B''_0 (P/B_0)^2 + \dots\} \quad (5.9)$$

The above equation is integrated to give

$$\frac{V}{V_0} = \left[ \frac{2 + (B'_0 - \Gamma)(P/B_0)}{2 + (B'_0 + \Gamma)(P/B_0)} \right]^{1/\Gamma} \quad (5.10)$$

where  $V_0$  (297 K,  $P=0$ ) = 45.557 cm<sup>3</sup>/mole and  $\Gamma^2 = (B'_0 - 2B''_0) > 0$  with  $B'_0 = 37.03 \pm 0.06$  kbar at  $T = 4.2$  K. The parameters  $B'_0 = (\partial B_T / \partial P)_T$  and  $B''_0 = (\partial^2 B_T / \partial P^2)_T$  were evaluated at  $T = 4.2$  K to be  $4.06 \pm 0.03$  and  $-0.041 \pm 0.006$  kbar<sup>-1</sup>, respectively. These parameters were used in equation (5.8) to obtain the change of  $(\Delta V/V_0)$  with pressure up to 5 kbar. The



pressure dependence of  $\gamma_G$  up to 32 kbar for potassium has been determined by Boehler (1983) through measurements of the adiabatic pressure derivatives with temperature. They concluded that  $\gamma_G = \gamma_0 (V/V_0)^q$  with  $q = 1$  and  $\gamma_0 = 1.27$  at a pressure of 1 bar and a temperature of  $25^\circ\text{C}$ . Based on their results, the pressure dependence of  $\gamma_G$  was calculated up to 5 kbar.

The pressure dependence of  $\Delta V/V_0$ ,  $\gamma_G$  and  $\gamma_{ep}$  determined in the above way are presented in table 5-2 for the pressure range 0-5 kbar. A plot of the calculated electron-phonon mass, normalized to its value at a pressure of 1 bar,  $m_{ep}^*(P)/m_{ep}^*(0) = [(1+\lambda_{ep})/(1+\lambda_0)]$ , along with the measured  $m^*(P)/m^*(0)$  versus pressure is shown in Figure 5-3. The calculated plot indicates a departure from linearity. This basically results from the functional form of  $\lambda_{ep}$  given by equation 5-7. Such deviation from linearity cannot be distinguished due to the experimental uncertainties shown in Figure 5-3. The gradient of the tangent of the calculated plot in Figure 5-3 at 2 kbar yields  $d\lambda_{ep}/dP$  and we find that

$$(1/(1+\lambda_0))(d\lambda_{ep}/dP) = -0.62 \times 10^{-2} \text{ kbar}^{-1} \quad (5.11)$$

This calculated value agrees within experimental uncertainty with our measured value for  $(1/m^*)dm^*/dP$  of  $-(0.71 \pm 0.12) \times 10^{-2} \text{ kbar}^{-1}$ . The small difference between the observed and predicted pressure derivatives of  $(m^*/m_0)$ , particularly at pressures greater than 2 kbar, is attributed to changes of electron-electron and band structure effects with pressure.

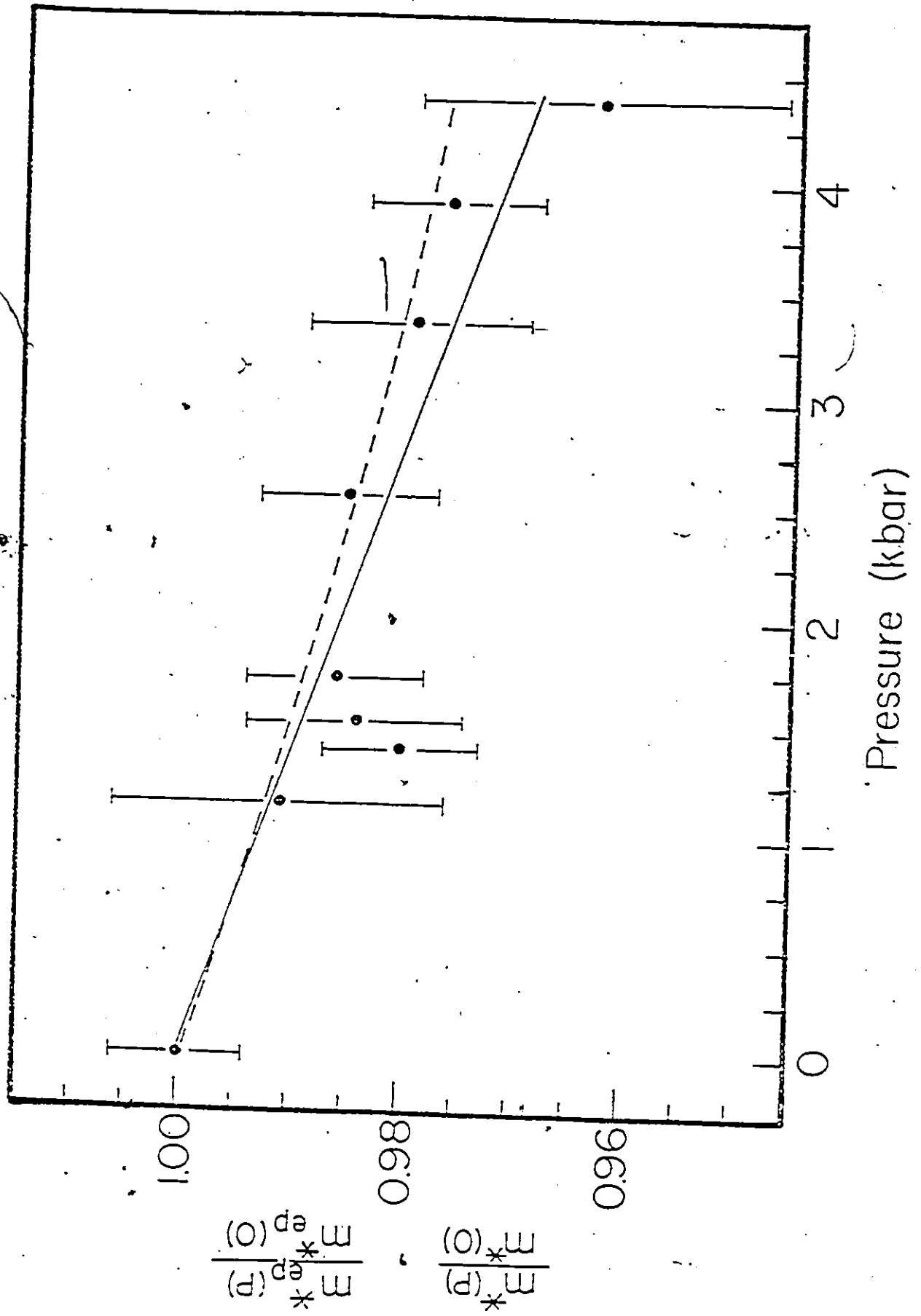
Table 5-2

Calculated pressure dependences of  $\Delta V/V_0$ ,  $\gamma_G$  and  $\gamma_{ep}$ 

Pressure (kbar)	$\Delta V/V_0\%$	$\gamma_G$	$\gamma_{ep}$
0		1.27	.135
.5	1.31	1.25	.131
1.0	2.53	1.24	.127
1.5	3.68	1.22	.124
2.0	4.77	1.21	.121
2.5	5.81	1.19	.118
3.0	6.77	1.18	.116
3.5	7.71	1.17	.114
4.0	8.58	1.16	.112
4.5	9.43	1.15	.110
5.0	10.23	1.14	.108

The satisfactory agreement between the measured and calculated pressure dependence of the cyclotron effective mass suggests that any change in the band mass with pressure should be compensated by an opposite change in the electron-electron enhancement parameter with pressure or that the pressure dependence of both are small. Indeed, studies by Trofimenkoff and Carbotte (1970) and Seiden (1969) have demonstrated that the Coulomb interaction term is nearly insensitive to pressure and can be considered as a constant. On the other hand, calculation of the volume

Figure 5-3 A plot of the cyclotron effective mass normalized to its value at standard atmospheric pressure  $m^*(P)/m^*(0)$  versus pressure up to 4.4 kbar. The solid line is a weighted least squares linear fit to the experimental data points. The dotted line presents the calculated  $m_{ep}^*(P)/m_{ep}^*(0)$  values versus pressure.



dependence of the band mass in potassium by Wilk et al (1979) indicates that  $m_b$  increases from  $1.086 m_0$  to  $1.118 m_0$  between 0 and 4 kbar. This change along with the change in electron-phonon mass enhancement yields  $(1/m^*)dm^*/dP = + 0.27 \times 10^{-2} \text{ kbar}^{-1}$ . This value is in definite contrast with the observed experimental value. It should be noted however that the calculated value of  $m_b$  at standard atmospheric pressure is higher than that expected from the Fermi surface of potassium which is free electron like to within 0.2% (Lee and Falicov 1968 and Lee 1970) and is greater than the value measured by Knecht (1975).

The influence of pressure on the band mass can be studied in a metal with negligible many body effects, especially the electron-phonon interaction. Antimony satisfies these criteria and we have completed measurements on the hydrostatic pressure dependence of the cyclotron effective mass in antimony (will be presented in the next chapter). The results obtained indicate that  $m^*/m_0$  is nearly independent of pressure within the quoted experimental error. Thus the pressure dependence of the band mass in antimony with nearly ellipsoidal Fermi surface is small as predicted from band theory and it is reasonable that the band mass in potassium is insignificantly influenced by pressure.

The pressure dependence of the electron quasiparticle mass in potassium has been studied recently by Leavens et al (1983) in which the pressure variations of the band mass,  $\lambda_{ep}$  and  $\lambda_{ee}$  renormalization parameters have been taken into consideration. The pressure derivative of  $\lambda_{ep}$  was determined from a first principle nonlocal pseudopotential scheme with  $B=1$ , while the pressure dependences of the band mass and  $\lambda_{ee}$  were

estimated from the theory of Wilk et al (1979) and MacDonald et al (1980), respectively. The compressibility  $K = 2.7\%$  was taken from the experiment of Monfort and Swensen (1965) and their calculated Grüneisen parameter was  $\gamma_G = 1.4$ . According to their theory  $\{1/(1+\lambda_{ep})\}(d\lambda_{ep}/dP)_{p=0}$  was determined to be  $-1.134 \times 10^{-2} \text{ kbar}^{-1}$ . If we take  $\gamma_G = 1.4$  and use equation (5.4) we find that  $\{1/(1+\lambda_{ep})\}(d\lambda_{ep}/dP) = -0.97 \times 10^{-2} \text{ kbar}^{-1}$  which is about 17% lower than their calculated value. They also estimated  $(1/m_b)dm_b/dP$  and  $\{1/(1+\lambda_{ee})\}(d\lambda_{ee}/dP)$  to be  $0.648 \times 10^{-2}$  and  $-0.27 \times 10^{-2} \text{ kbar}^{-1}$ , respectively. Thus the changes in band mass and the electron-electron renormalization are of opposite sign. It should be noted that the large contribution calculated for  $(d\lambda_{ee}/dP)$  is due to considering  $m_b > 1$ . These three contributions yielded  $(1/m^*)(dm^*/dP)_{p=0} = 0.76 \times 10^{-2} \text{ kbar}^{-1}$ , which is in agreement with our measured value. However, a large departure of  $m^*/m_0$  versus pressure from linearity was reported by them. The value of  $(1/m^*)dm^*/dP$  at 2 kbar was calculated to be  $-0.4 \times 10^{-2} \text{ kbar}^{-1}$ , which is in lower by about 40% from our average value of  $-0.71 \times 10^{-2} \text{ kbar}^{-1}$ .

In conclusion, the present experimental results provide evidence for the mass enhancement due to many body electron-phonon interactions, since it was found that the pressure dependence of the cyclotron effective mass is significantly influenced by the pressure dependence of the electron-phonon renormalization parameter. The changes in the band structure mass and electron-electron mass enhancement with pressure are small and are of opposite sign.

## CHAPTER 6

### EXPERIMENTAL RESULTS AND ANALYSIS OF THE PRESSURE DEPENDENCE OF THE HOLE FERMI SURFACE AND CYCLOTRON EFFECTIVE MASS OF PURE ANTIMONY

#### 1. Pressure dependence of the hole Fermi surface

The influence of hydrostatic pressure up to 4.3 kbar on the geometric structure of the hole Fermi surface was investigated in the trigonal-bisectrix crystallographic plane of pure antimony. Four oscillatory components exist simultaneously in this plane. Two of them are associated with the principal and nonprincipal electron branches, while the other two correspond to the principal and nonprincipal hole branches. The oscillatory component associated with the principal hole branch was isolated and recorded separately, while the others were rejected by the use of the spectrometer techniques explained in chapter 4.

Since the influence of pressure in the pressure region investigated was expected to be small, special care was taken to account for the effect of possible change of sample orientation due to the application of pressure. This was done by performing rotation experiments before applying pressure, during compression and after removal of pressure. Figure 6-1 shows an example of a recorder trace of the quantum oscillation of the de Haas-van Alphen effect (dHvA) associated with the principal hole branch as a function of the direction of the magnetic field as it was rotated in the trigonal-bisectrix crystallographic plane at a pressure of 1.08 kbar. Rotation measurements were taken at a temperature of 1.2 K

and a magnetic field of approximately 1 Tesla. The strength of the magnetic field at which the rotation experiments were performed was set as low as possible but such that the desired oscillations could be easily followed. The primary reason for working at low magnetic fields was to eliminate problems associated with possible changes of sample orientation with respect to field caused by the torque at high field. Also, working at low field gave a higher number of oscillations in the rotation diagrams and consequently a higher density of points on the graph of the angular dependence of the dHvA frequency, which was the end product of the rotation diagram. As can be seen from the rotation diagram presented in figure 6-1, the effect of mixing between different oscillatory components of the Fermi surface is of no consequence. This demonstrates the effectiveness of the spectrometer techniques used which provided a good quality single de Haas-van Alphen oscillation resulting in no ambiguity or complication in the analysis.

The field rotation diagrams map out directly the relative changes of the phase of the de Haas-van Alphen oscillations with respect to some reference point. Each recorded oscillation means that the phase of the dHvA signal has changed by  $2\pi$ . If  $n$  oscillations occur, the dHvA frequency,  $F$ , at the new crystallographic orientation is related to the reference frequency,  $F_r$ , by the equation

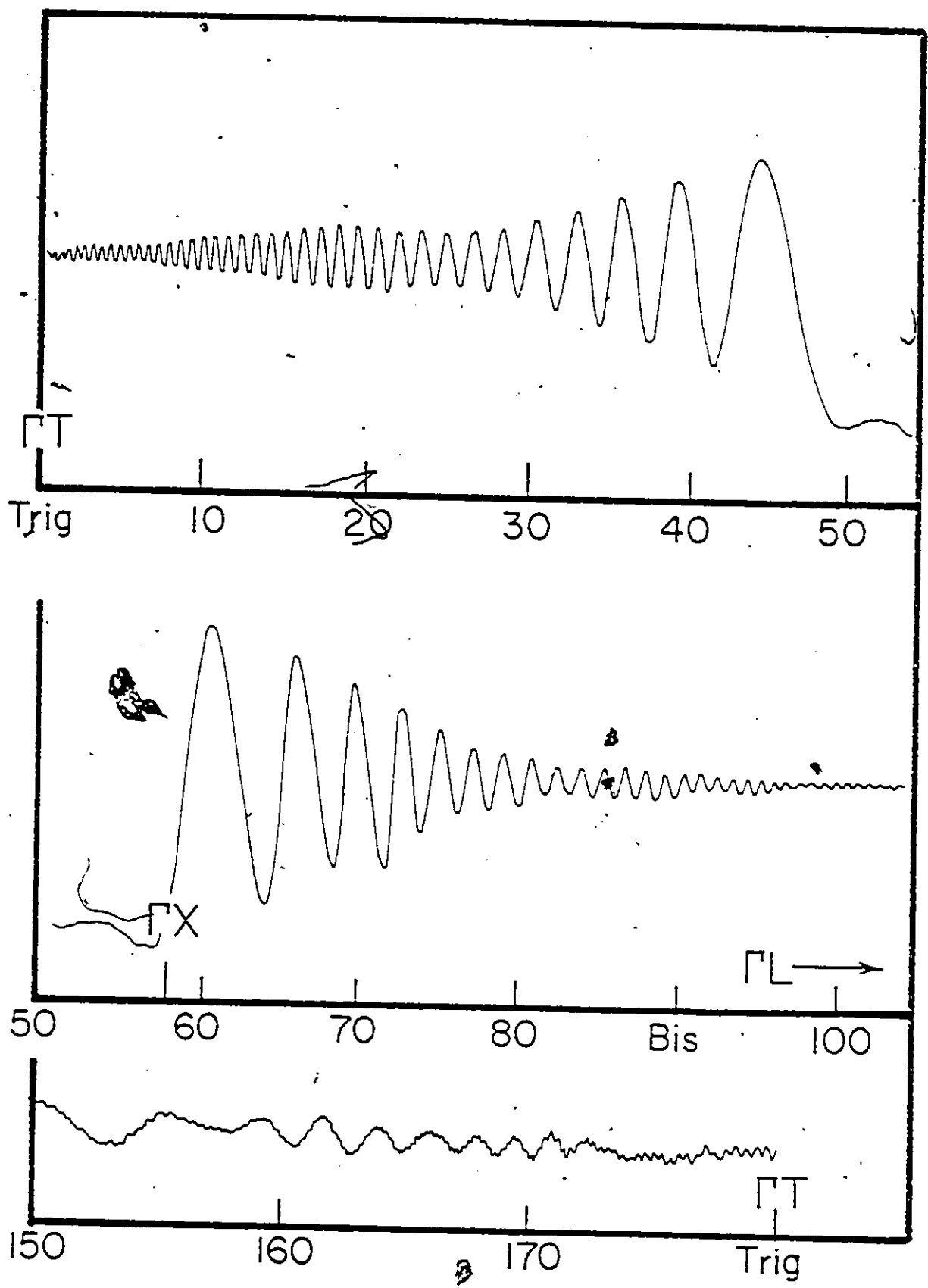
$$F(\theta) - F_r(\theta) = nH$$

where  $H$  is the strength of the magnetic field. The reference frequency was chosen to be the one at the minimum cross-sectional area of the hole



Figure 6-1 A recorder trace of the quantum oscillation of the de Haas-van Alphen effect associated with the principal hole branch as a function of the direction of the magnetic field as it was rotated in the trigonal-bisectrix plane at pressure and magnetic field strength of 1.08 kbar and  $\approx 1$  Tesla, respectively. The size of the dHvA signal in the first two and the third traces was reduced by approximately factors of 6 and 4, respectively.

De Haas - van Alphen signal (arbitrary units)

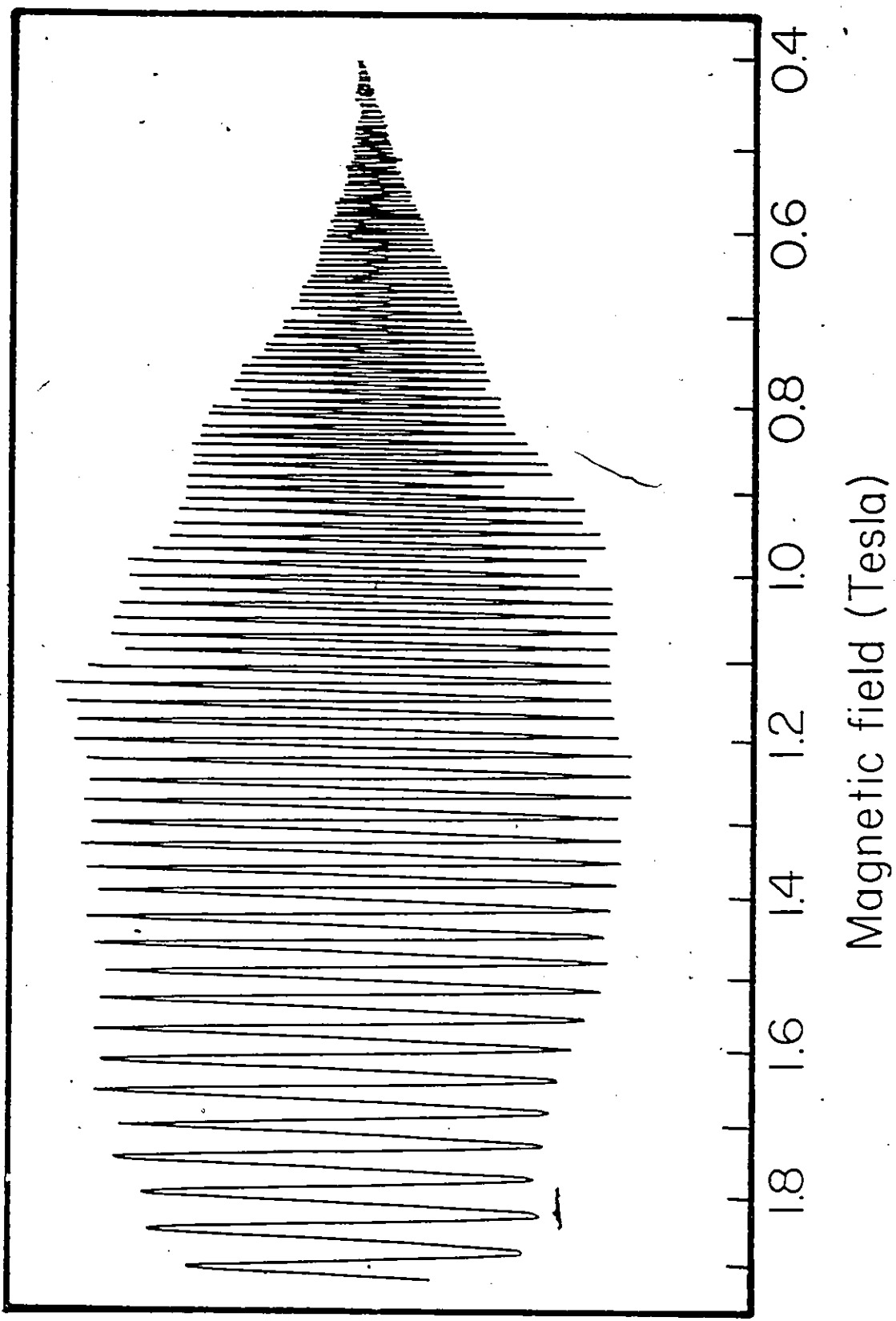


Magnetic field direction (degree)

Fermi surface. The advantage of taking this reference frequency is that the effect of angular uncertainties is minimized because the phase of the oscillations in the close neighborhood of this direction is a slowly varying function of angle with  $dF/d\theta = 0$  right at the minimum section of the branch. Also, the accuracy in measuring the reference frequency is optimized because the amplitude of the oscillation at that particular direction is the largest and its damping with decreasing field is relatively small because of its small effective mass.

The reference frequency was measured by counting the number of oscillations as the magnetic field was swept over the widest available range of 1.9-0.4 Tesla. The frequency is defined as;  $F = m\{1/|H_1| - 1/|H_2|\}^{-1}$  units of Tesla, where  $m$  is the observed number of oscillations between magnetic fields  $H_1$  and  $H_2$ . Therefore, a plot of  $m$  against  $1/H$  yields a straight line with slope  $F$ . The accuracy of the measured frequency was limited by the number of oscillations and the accuracy of the magnetic field readings which were calibrated by nuclear magnetic resonance to within  $< 0.2\%$  up to 1 Tesla. Figure 6-2 shows an example of a recorder trace of the quantum oscillations of the magnetic susceptibility as a function of magnetic field strength with the magnetic field along the minimum section of the branch at a pressure of 1.08 kbar. In figure 6-3, the observed number of oscillations was plotted as a function of reciprocal magnetic field strength. All data points were fitted by a least squares method. The absolute frequency measurements were made at various pressures up to 4.3 kbar. All measurements were accurate to within  $< 0.3\%$  determined by the method of least squares.

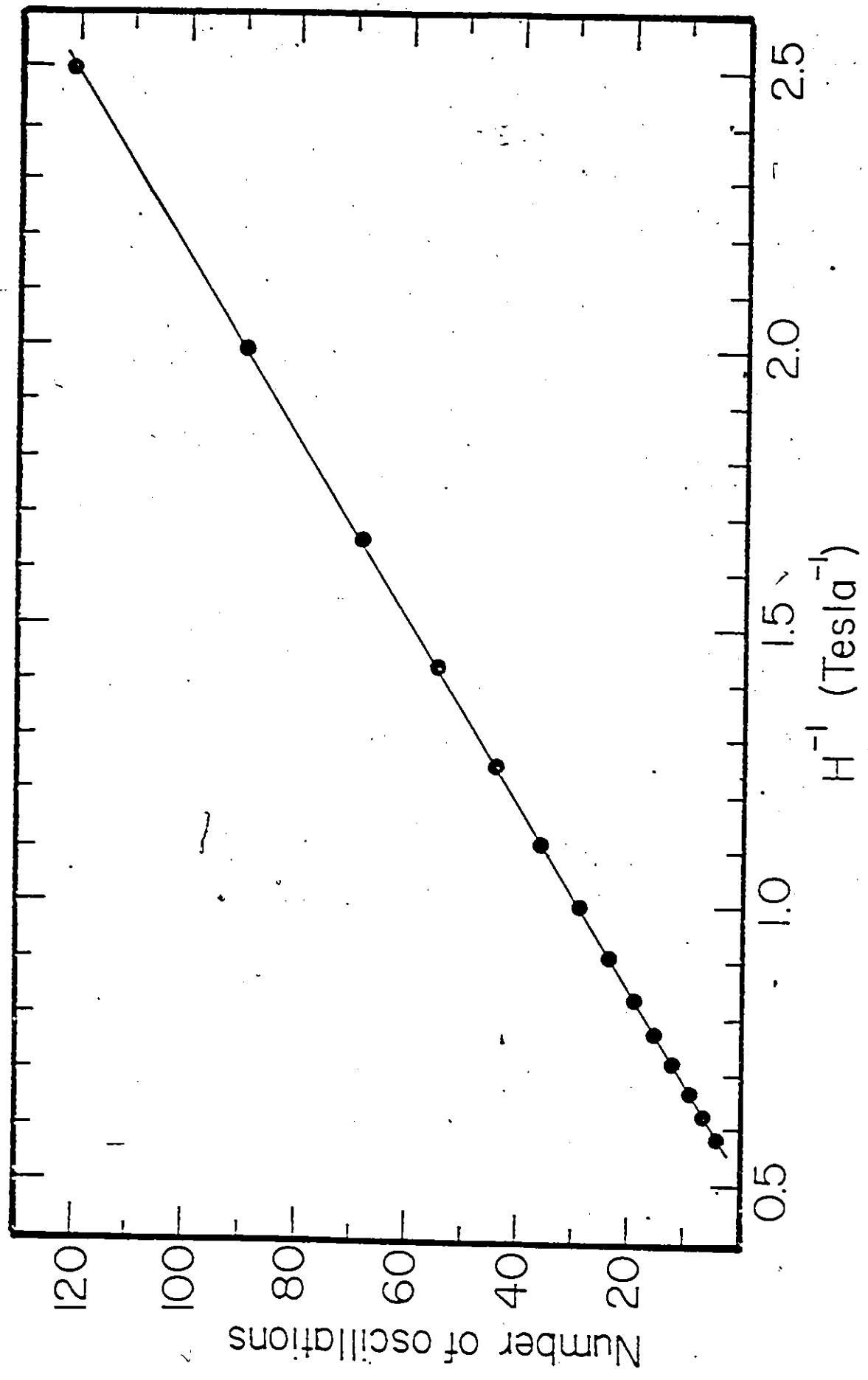
Figure 6-2. A recorder trace of the quantum oscillation of the magnetic susceptibility as a function of magnetic field strength with the magnetic field direction along the minimum section of the hole Fermi surface at a pressure of 1.08 kbar.



DHVA signal (arbitrary units)

Magnetic field (Tesla)

Figure 6-3 A plot of the number of the de Haas-van Alphen oscillations versus the reciprocal of magnetic field strength,  $H^{-1}$ , along the minimum cross-sectional area of the principal hole branch in the trigonal-bisectrix plane at a pressure of 1.08 kbar. The solid line is a weighted least-squares linear fit to the data points.



Frequency measurements made along several crystallographic directions by a field sweep procedure were compared with the rotation measurements, i.e. the relative measurements, to check the consistency of the results. Table 6-1 gives values of absolute and relative frequency measurements at standard atmospheric pressure (1 bar) and a pressure of 1.08 kbar. Good agreement within estimated experimental uncertainties was obtained. At this point it should be noted that the relative measurements yield about an order of magnitude better accuracy than the absolute measurements. The reason for this, is that the frequency is much greater than the magnitude of the magnetic field and accurate values of  $H$  are not as important as for absolute measurements.

In figures 6-4 and 6-5 are plotted the angular dependences of the frequencies of the de Haas-van Alphen oscillations of the hole branch in the trigonal-bisectrix crystallographic plane at pressures of 1 bar and 1.08 and 3.89 kbar. At  $P = 1.08$  kbar, all frequencies in the angular region from  $10^\circ - 110^\circ$  are decreased below their values at standard atmospheric pressure, while in the angular region from  $150^\circ - 180^\circ$  they are increased above their values at standard atmospheric pressure. At a pressure of 3.89 kbar, all frequencies are decreased below their values at  $P = 1$  bar. At standard atmospheric pressure the frequencies associated with the minimum and maximum sections of the hole branch were determined to be  $(61.8 \pm 0.1)$  Tesla and  $(196 \pm 2)$  Tesla, respectively. Their tilt angles occurred at  $(52.5^\circ \pm 1^\circ)$  and  $(150^\circ \pm 2^\circ)$ , respectively. These angles were measured from the trigonal axis in the sense of a rotation from  $\overline{111}$  towards  $\overline{110}$ .



Table 6-1

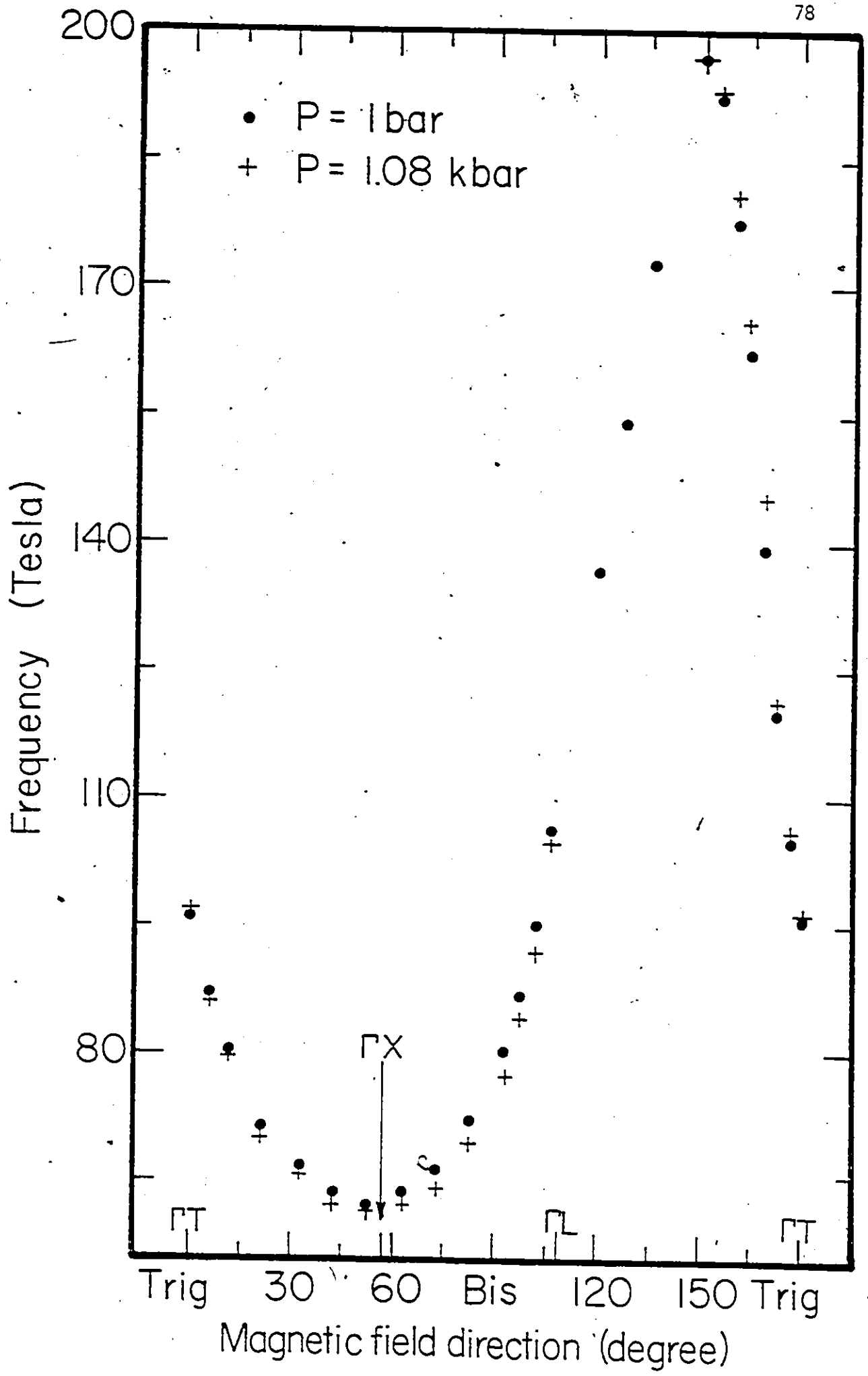
Absolute and relative frequency measurements of the principal hole branch at various angles in the trigonal-bisectrix plane at pressures of 1 bar and 1.08 kbar.

P = 1 bar		P = 1.08 kbar			
$\theta^0$ <sup>(1)</sup>	F(abs) <sup>(2)</sup>	F(rel) <sup>(3)</sup>	$\theta^0$	F(abs)	F(rel)
2.5	91.8±1.5	92.3±0.2	65	95.9±1.5	95.5±0.2
12.5	78.0±1.0	78.2±0.2	171	124.0±4.0	121.5±0.2
81.5	72.0±0.6	72.1±0.2	176	106.0±3.0	106.9±0.1
166	133.6±1.6	135.2±0.2	178	102.0±2.0	101.9±0.1
171	116.6±1.6	116.8±0.2			

(1) Angle  $\theta$  is measured from the trigonal axis in the sense of a rotation from IT toward IX.

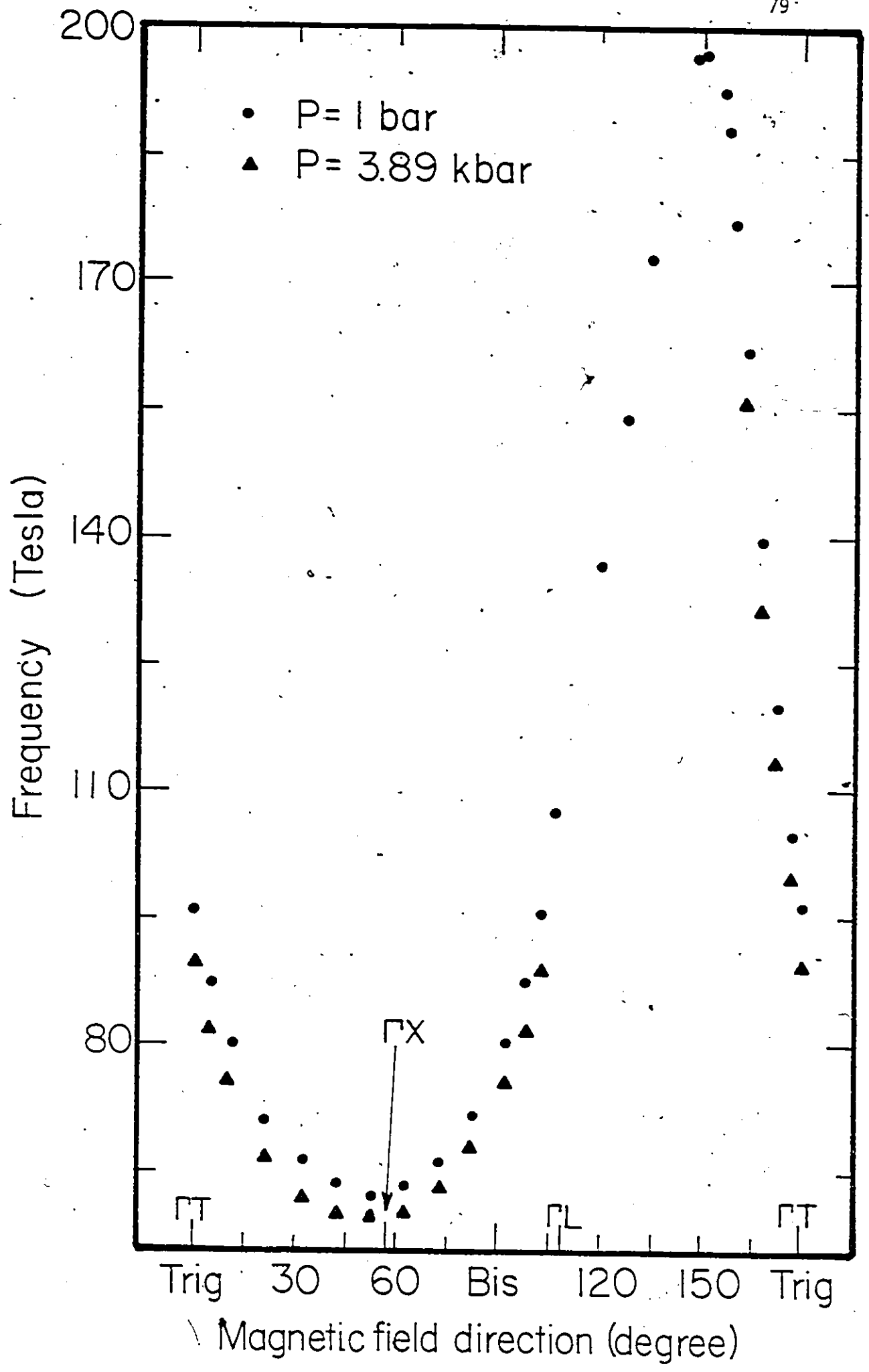
(2 & 3) F(abs) and F(rel) stand for absolute and relative frequency measurements in Tesla.

Figure 6-4 A plot of the angular dependences of the de Haas-van Alphen frequencies of the principal hole branch in the trigonal-bisectrix plane at pressures of 1 bar (●) and 1.08 kbar (+).



(2)

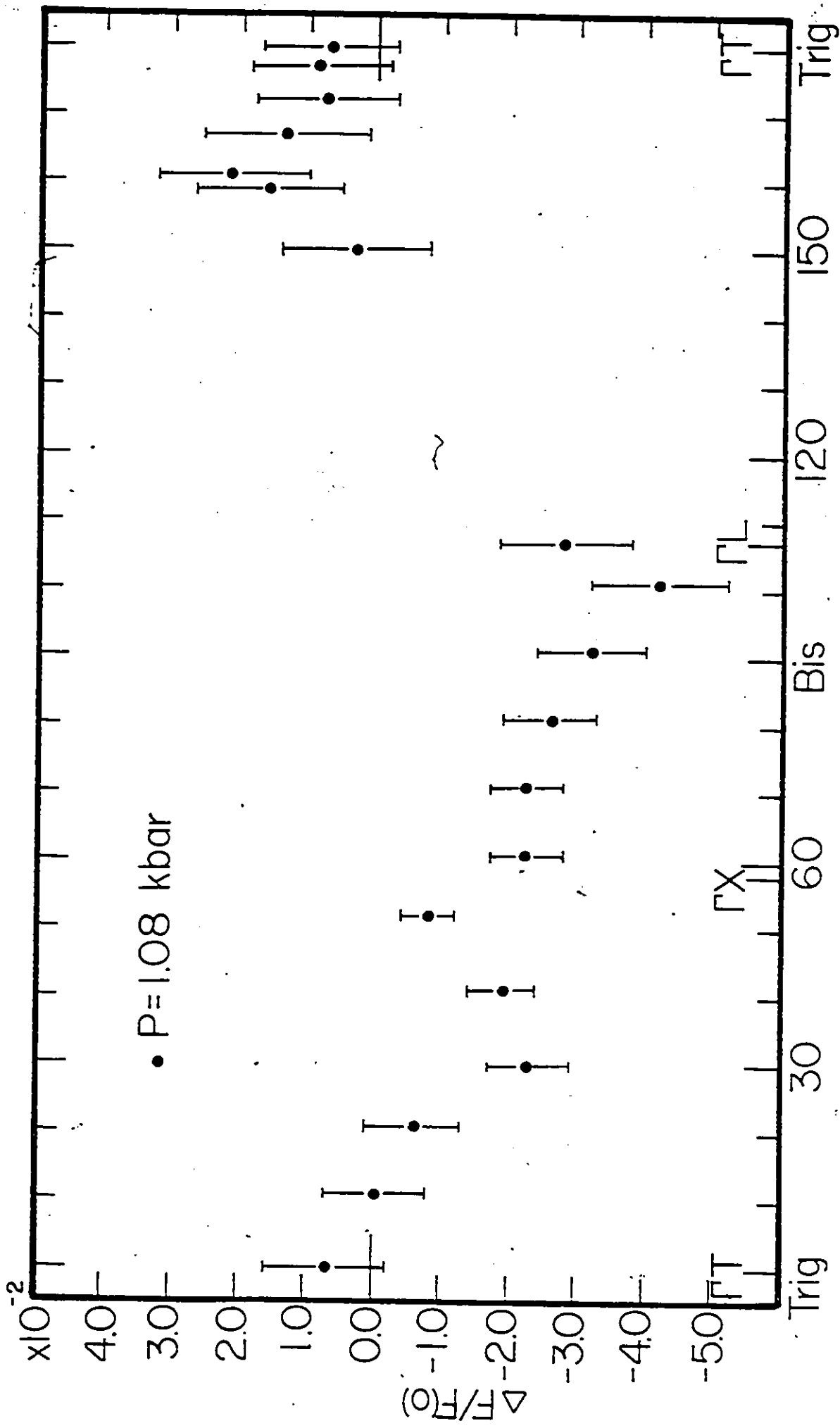
Figure 6-5 A plot of the angular dependences of the de Haas-van Alphen frequencies of the principal hole branch in the trigonal-bisectrix plane at pressures of; 1 bar (●) and 3.89 kbar (▲).



At this stage it should be pointed out that before the application of pressure the observed de Haas-van Alphen amplitudes in the angular region from  $110^\circ - 150^\circ$  were considerably smaller than those observed in the angular region from  $150^\circ - 180^\circ$ . This is due to the occurrence of two spin splitting zeros at about  $116^\circ$  and  $147^\circ$  measured from  $\Gamma$  in the sense toward  $\Gamma X$  (Windmiller 1966). Also, a slight decrease in the amplitudes of the signals was observed between successive pressure measurements. This indicated that the crystal quality decreased between different measurements at various pressures. The observed decrease in the amplitudes was most likely to be caused by sample strain produced during the process of freezing the helium in the pressure cell or cooling of the sample. The reduction in the amplitude did not affect significantly the overall quality of the data except in the angular region around the two spin splitting zeros where the amplitudes of the signals dropped to below the noise level. Also, we were not able to observe the maximum frequency of the branch at pressures greater than 1.08 kbar. Primarily, this is due to the fact that the size of the signal associated with the maximum section of the branch is the smallest, because of a relatively large effective mass.

The spectrometer techniques used to resolve and record separately the desired oscillatory component helped a great deal to accurately study the specific behaviour of the anisotropy of the hole Fermi surface. Figures from 6-6 to 6-9 demonstrate the influence of pressure up to approximately 4.2 kbar on the anisotropy of the rate of change of the extremal frequencies,  $\Delta F/F(0)$ : Here  $\Delta F$  is the difference between the measured frequency at a certain pressure,  $F(p)$ , and the observed one

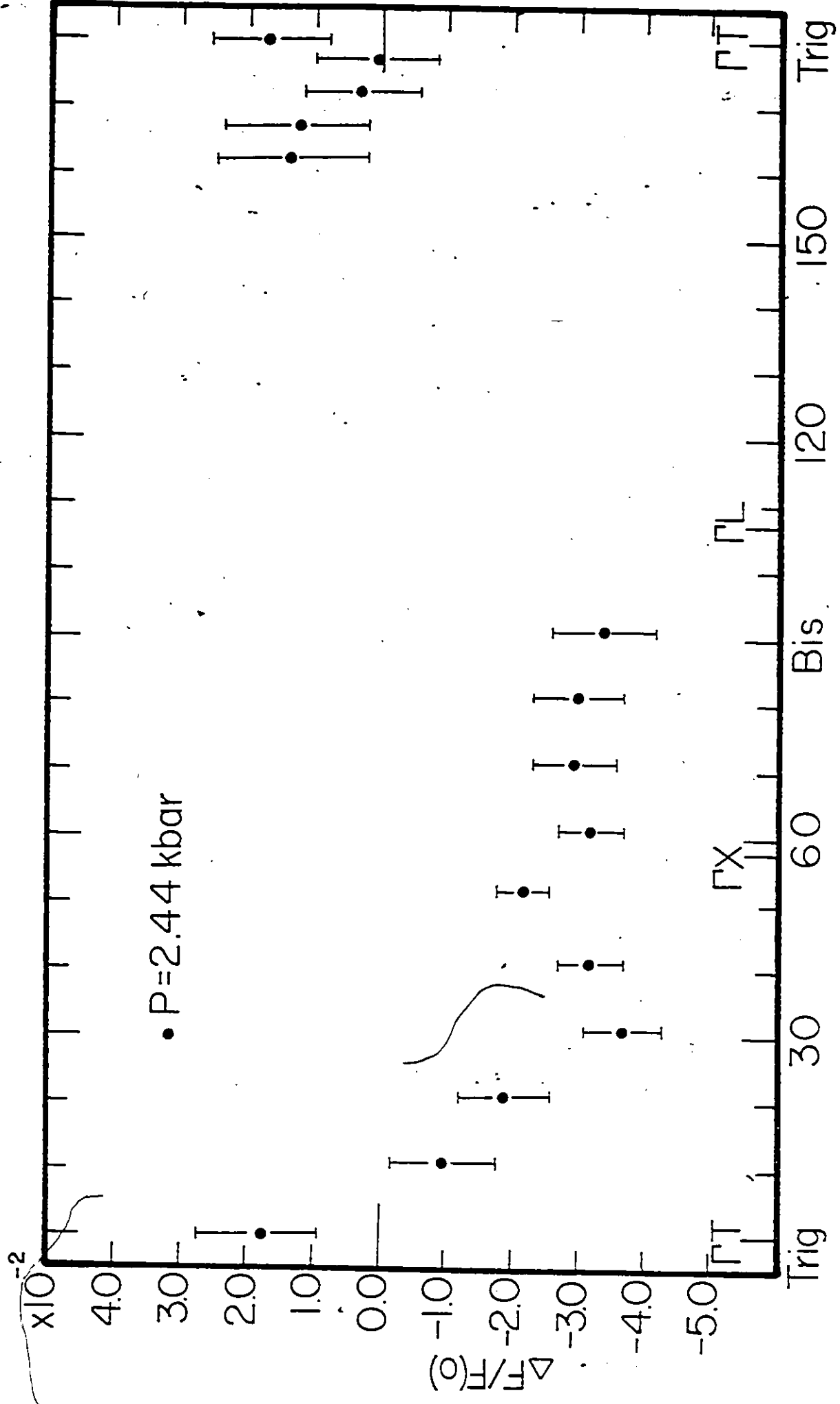
Figure 6-6 A plot of the angular dependences of the rate of change of the extremal frequencies,  $\Delta F/F(0)$ , of the principal hole branch in the trigonal-bisectrix crystallographic plane at a pressure of 1.03 kbar.



Magnetic field direction (degré)

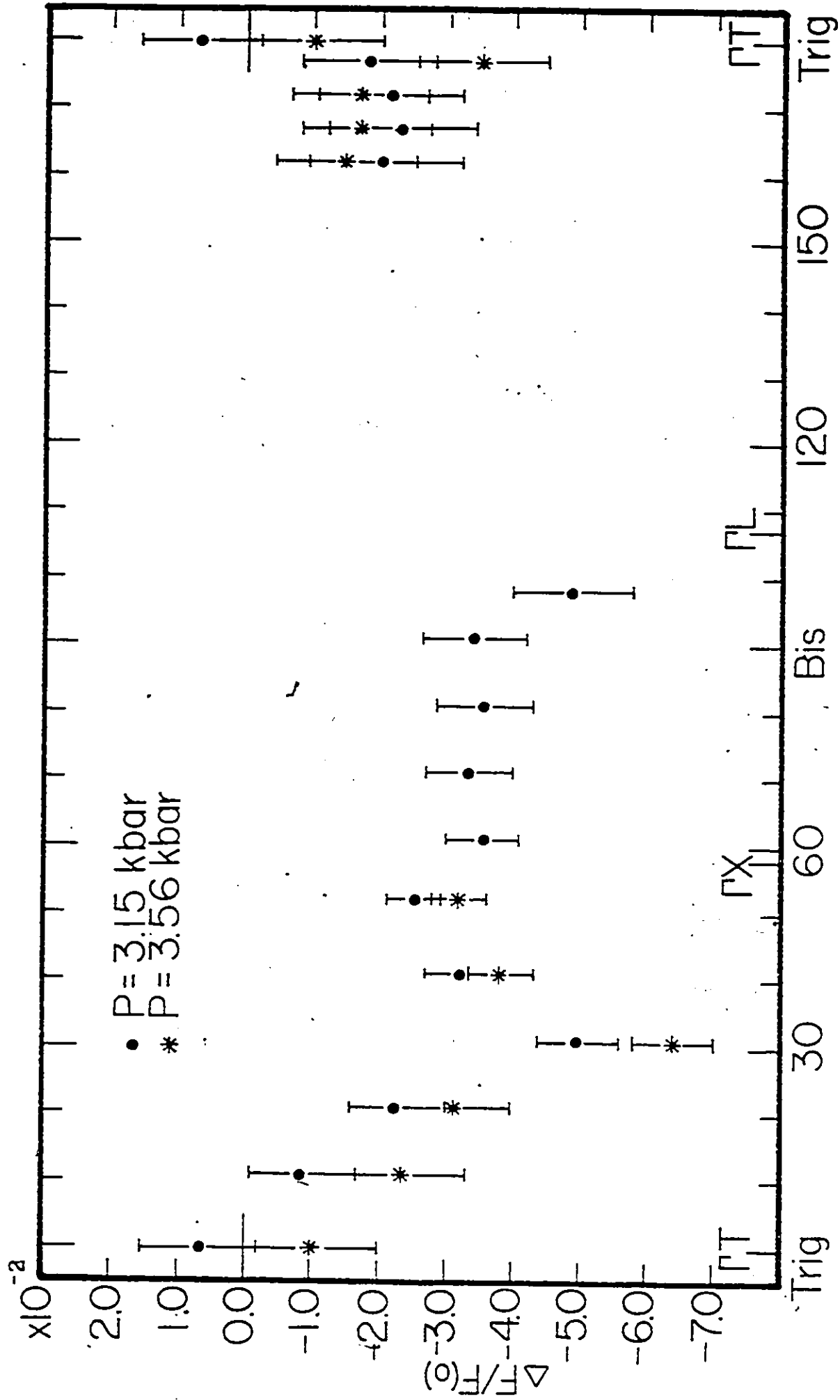


Figure 6-7 A plot of the angular dependences of the rate of change of the extremal frequencies,  $\Delta F/F(0)$ , of the principal hole branch in the trigonal-bisectrix crystallographic plane at a pressure of 2.44 kbar.



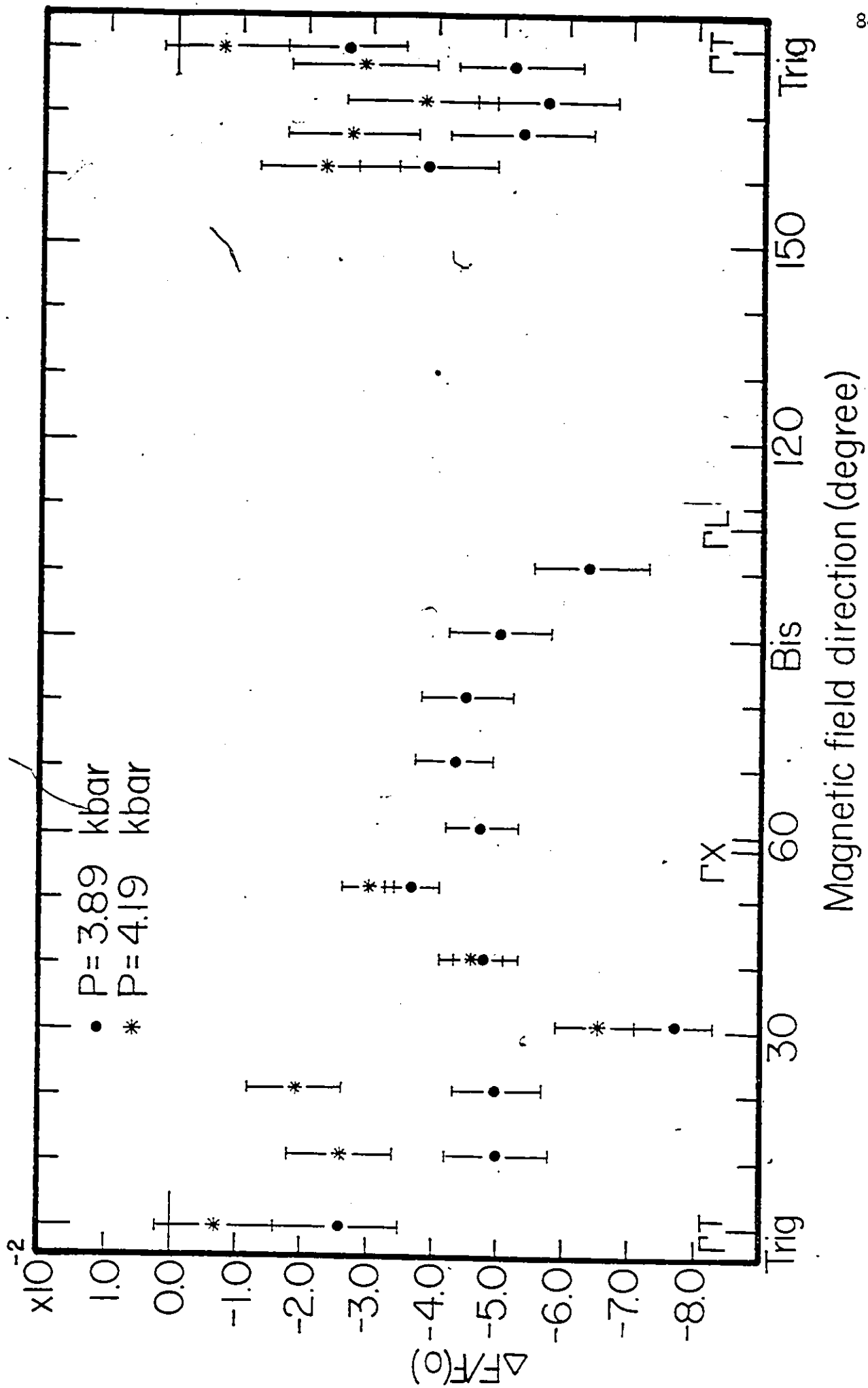
Magnetic field direction (degree)

Figure 6-8 A plot of the angular dependences of the rate of change of the extremal frequencies,  $\Delta F/F(0)$ , of the principal hole branch in the trigonal-bisectrix crystallographic plane at pressures of 3.15 (●) and 3.56 (★) kbar.



Magnetic field direction (degree)

Figure 6-9 A plot of the angular dependences of the rate of change of the extremal frequencies,  $\Delta F/F(0)$ , of the principal hole branch in the trigonal-bisectrix plane at pressures of 3.89 (●) and 4.19 (\*) kbar.



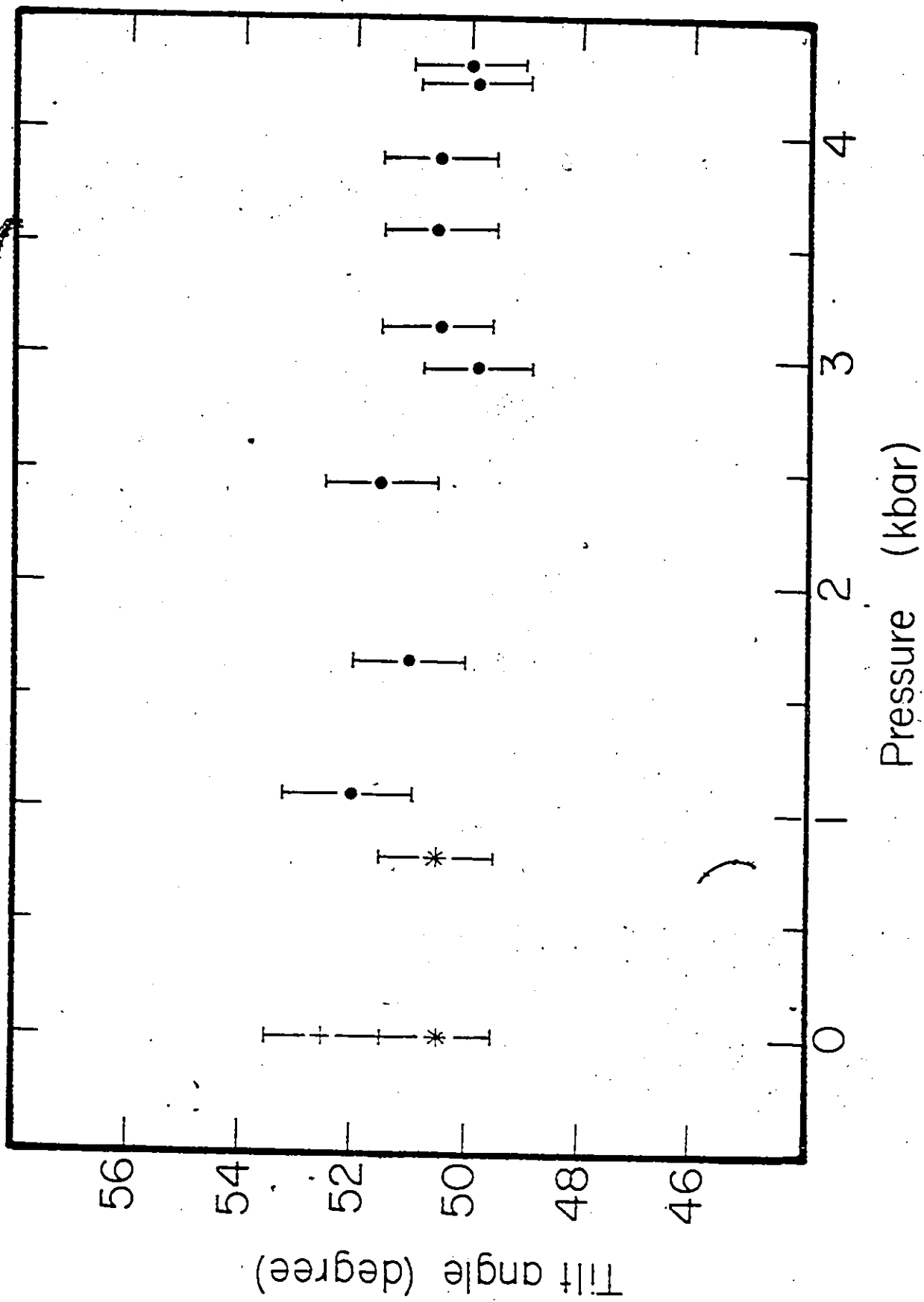
at standard atmospheric pressure,  $F(0)$ . The final analysis of these graphs will be discussed in the next chapter.

Before going on to describe our experimental results on the influences of hydrostatic pressure on the minimum section of the hole Fermi surface, it is appropriate to discuss the method used in determining the tilt angle and its pressure dependence. Here, the tilt angle is measured from the trigonal axis in the sense of a rotation from  $\Gamma T$  toward  $\Gamma X$ . In figure 6-10 is plotted the tilt angle of the hole Fermi surface in the trigonal-bisectrix plane versus pressure up to 4.3 kbar. This graph demonstrates that the tilt angle is nearly insensitive to pressure within quoted experimental errors ( $< \pm 1^\circ$ ). A  $2.5^\circ$  difference between the determined angle before the application of pressure and the one measured after the application of a pressure of 4.3 kbar, appeared to be caused by slight crystal misorientations which arose from the application of pressure. This was proven by redetermining the tilt angle at pressures of 0.8 kbar and 1 bar after gradual removal of pressure.

The tilt angle was determined carefully from rotation diagrams and also from absolute frequency measurements versus angle. The rotation speed of the electromagnet was adjusted to be at its slowest possible speed. This way it was possible to map out clearly the change of the de Haas-van Alphen phase as a function of the magnetic field direction,  $\theta$ , as it was rotated in the trigonal-bisectrix plane, which was rather flat around the minimum section. The mid point of the flat portion, that is at which  $dF/d\theta$  is expected to vanish, was a measure of the tilt angle. To check the accuracy of the rotation diagram measure-

Figure 6-10 A plot of the tilt angle of the principal hole branch in the trigonal-bisectrix crystallographic plane ver-  
sus pressure up to 4.5 kbar.





ments, about five absolute frequency measurements at  $1^\circ$  steps at each side of the determined minimum section were made. From a graph of the measured  $F$  versus  $\theta$ , we were able to specify the tilt angle with an accuracy of better than  $\pm 1^\circ$ . Note that the plot of  $F$  versus  $\theta$  was useful in estimating the angular error in the measured tilt angle.

The hydrostatic pressure dependence of the minimum frequency of the hole Fermi surface is shown in figure 6-11. All measurements were made with the magnetic field along the direction of the minimum section. The data points indicate that the frequency decreases with increasing pressure in a nonlinear fashion up to 3.8 kbar. However, when we made a linear fit to this region, a weighted least squares fit to all data points yielded

$$\frac{1}{F} (dF/dP) = - (0.91 \pm 0.07) \times 10^{-2} \text{ kbar}^{-1}$$

It is also evident that the rate of change of the frequency with pressure becomes significantly slower in the pressure region from 3.4 kbar. The pressure derivative of the frequency reached its minimum value at  $(3.7 \pm 0.3)$  kbar and then started to change sign with further increase in pressure.

The pressure dependence of the de Haas-van Alphen frequency at  $161^\circ$  measured from  $\Gamma T$  in the sense toward  $\Gamma X$ , that is  $11^\circ$  from the maximum of the branch, was determined. In figure 6-12 is plotted the de Haas-van Alphen frequency versus pressure up to 4.2 kbar. It is evident that the frequency increases with increasing pressure up to 1.08 kbar and then started to decrease with further increase in pressure up to approximately 4 kbar. The linear least squares fit to the data points up to


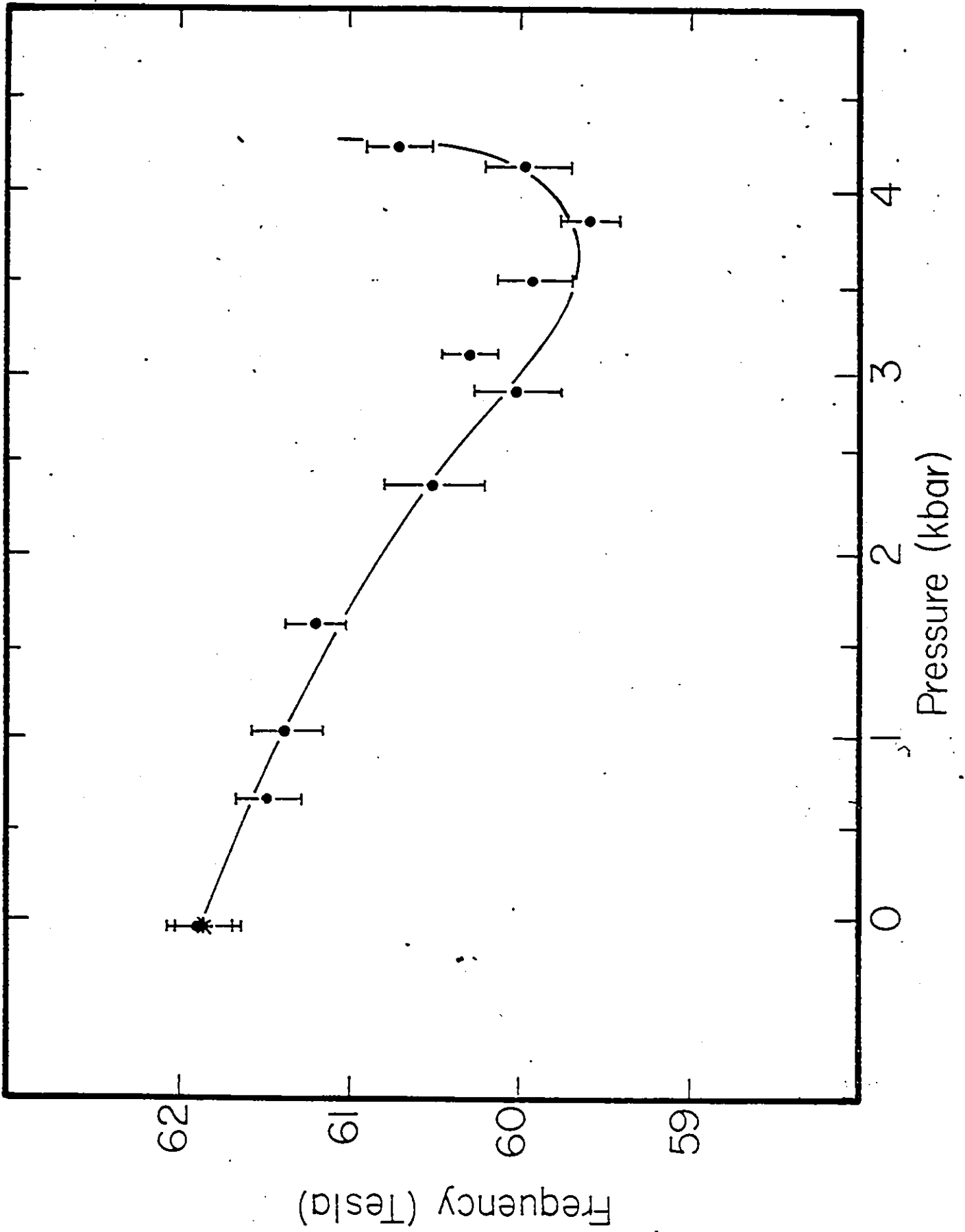


Figure 6-11 A plot of the minimum frequency of the principal hole branch, in the trigonal bisectrix plane versus pressure up to 4.3 kbar, with magnetic field along the minimum cross-sectional area of the branch. \* is a point taken after removal of pressure.

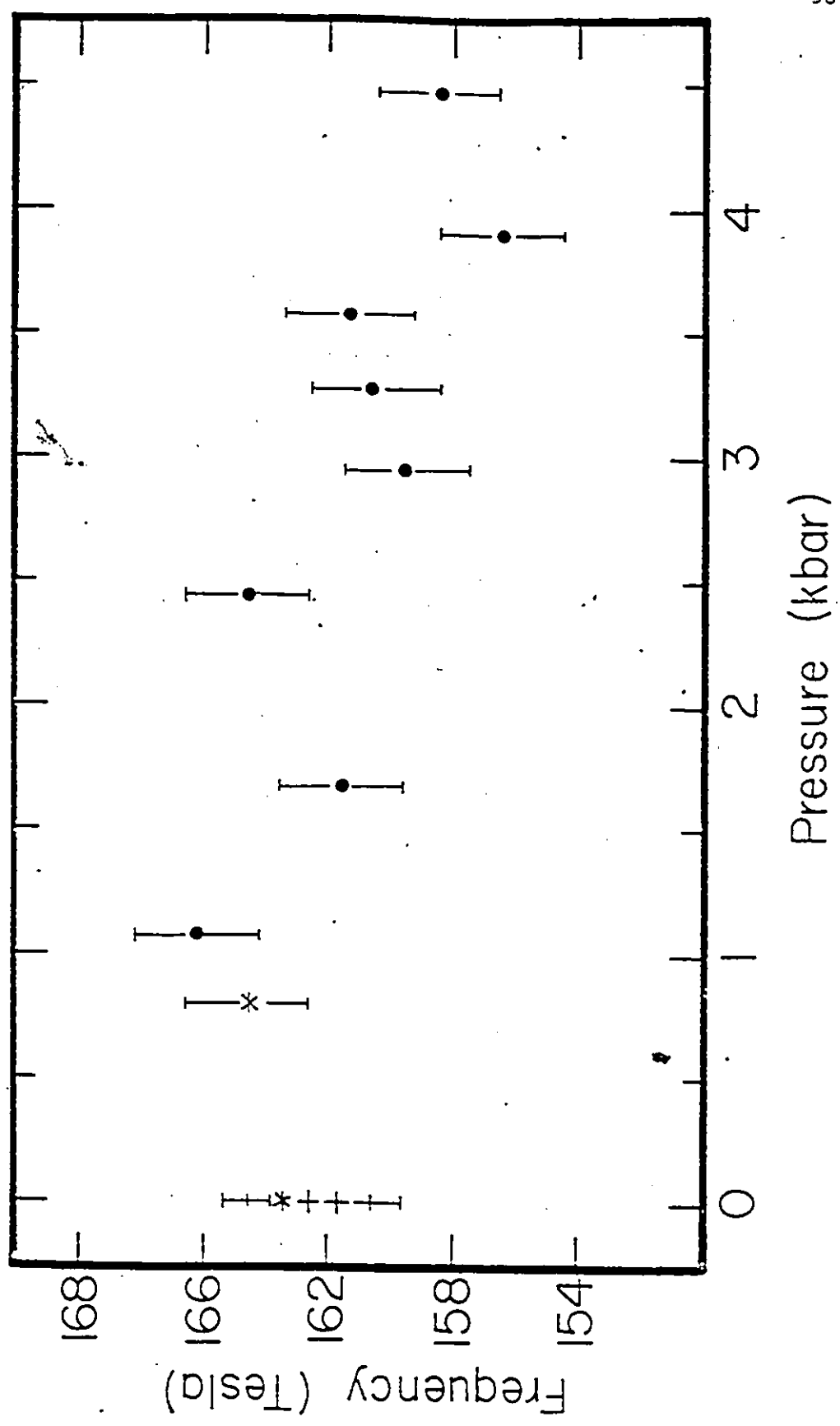


1.08 kbar yielded a pressure derivative,  $(1/F)dF/dP$ , of  $(2.3 \pm 0.1) \times 10^{-2}$   $\text{kbar}^{-1}$ . As can be seen from figure 6-12 and at pressures above 1.08 kbar the frequency is not a linear function of pressure. However, when we made a linear fit in this region, a weighted least squares fit yielded,  $(1/F)dF/dP = - (1.4 \pm 0.3) \times 10^{-2}$   $\text{kbar}^{-1}$ .

The frequencies presented in figure 6-12 were estimated from rotation diagrams taken at various pressures and at constant magnetic field by counting the number of oscillations as a function of magnetic field direction with respect to the reference frequency. At this point it should be pointed out that the high frequency measurements can be subject to a significant error associated with a possible slight misorientation of the sample due to the application of subsequent pressure. This is true, because the phase of the de Haas-van Alphen oscillation is a rapidly changing function of angle in the neighborhood of the maximum of the branch. Therefore, the sample alignment was checked thoroughly through careful determination of the tilt angle, as explained before. We observed a small upward or downward shift in the tilt angle with pressure (figure 6-10). For this reason, it was necessary to remove any relative offset between various experiments before evaluating the frequencies from the rotation diagrams. The measurements presented in figure 6-10 were useful in estimating the angular uncertainty. The standard deviation (which is taken to be the angular error) of the data points shown in this figure was calculated to be  $0.64^\circ$ . This caused an error of about 1.2% in the high frequency region at magnetic field of 1 Tesla. It should be noted, however, that the uncertainty in the frequency measurements

---

Figure 6-12 A plot of the de Haas-van Alphen frequency at  $11^\circ$  from the maximum of the principal hole branch in the trigonal-bisectrix plane versus pressure.



caused by a slight crystal misorientation decreases as the frequency decreases and becomes insignificant at the minimum frequency of the branch.

## 2. Pressure dependence of the cyclotron effective mass

The cyclotron effective mass,  $m^*$ , measurements right at the minimum cross-sectional area of the principal hole branch in the trigonal-bisectrix crystallographic plane were derived from the temperature dependence of the oscillatory magnetization amplitude,  $A(T)$ , at a fixed magnetic field strength of 1 Tesla, provided by an electromagnet, and covered temperature range of 1.2-4.2°K. These measurements were performed using the conventional field modulation technique introduced in chapter 4 with second harmonic detection.

Referring back to equation (5.2), it is clear that the amplitude of the oscillatory magnetization,  $A(T)$  is proportional to

$$T \left( \sinh 14.69 \frac{m^* T}{m_0 H} \right)^{-1} \quad (6-2)$$

Since  $m^*/m_0 < 0.1$ , in the case of antimony, therefore, it was necessary to use the full expression for the de Haas-van Alphen amplitude in determining  $m^*$ . Expressing the hyperbolic sine function in equation (6-2) in terms of its two exponentials, that is  $\sinh x = (e^x - e^{-x})/2$ , the above proportionality can be written as

$$\ln \left\{ \frac{A}{T} \left[ \exp \left( -2 \times 14.69 \frac{m^* T}{m_0 H} \right) \right] \right\} = -14.69 \frac{m^* T}{m_0 H} + \text{constant} \quad (6-3)$$

Therefore, a plot of  $\ln \{ A/T [\exp(-2 \times 14.69 (m^* T / m_0 H))] \} \equiv \ln Y$  versus  $T$  will yield a straight line of slope  $-14.69 (m^*/m_0 H)$ , where  $m^*/m$  is the



cyclotron mass normalized to the free electron mass. Since  $m^*/m_0$  is not initially known, a first approximation to it was obtained from the slope of  $\ln(A/T)$  against  $T$  at fixed magnetic field strength using the method of least squares. This approximate value of  $m^*/m_0$  was used in a plot of  $\ln Y$  against  $T$ . From this slope a second approximation to  $m^*/m_0$  was obtained. Thus, the iterations were performed until this slope became constant. Three examples of the least squares sinh fits to experimental data points of  $\ln(A/T)$  versus  $T$  for a magnetic field of 1 Tesla and pressures of 1 bar, 1.65 and 3.2 kbar are shown in figure 6-13, with cyclotron effective masses of  $(0.0635 \pm 0.0002)m_0$ ,  $(0.0645 \pm 0.0004)m_0$  and  $(0.0644 \pm 0.0005)m_0$ , respectively.

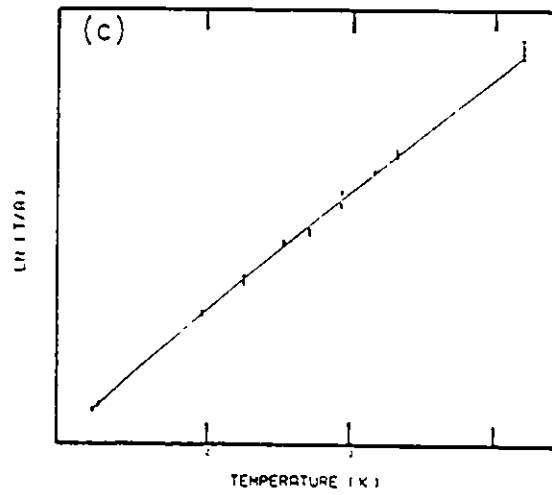
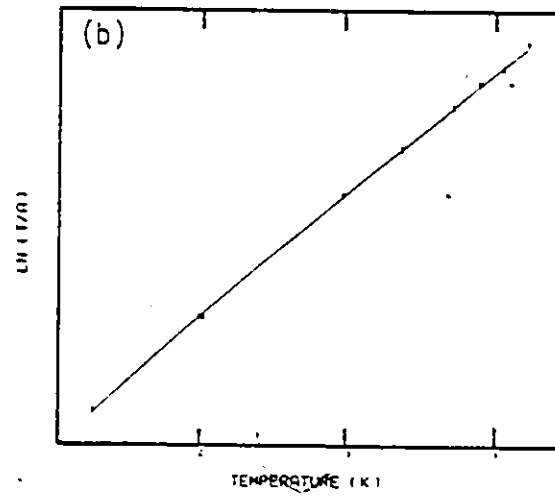
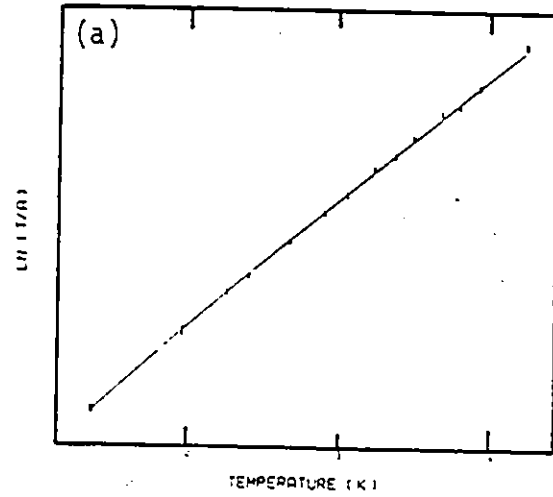
The measured hydrostatic pressure dependence of the cyclotron effective mass in the pressure range from 0 to 4 kbar is presented in figure 6-14. The weighted least squares fit to all data points yielded  $dm^*/dP = (0.1 \pm 0.2) \times 10^{-3} m_0 \cdot \text{kbar}^{-1}$  and we found that

$$\frac{1}{m^*} \frac{dm^*}{dP} = (0.16 \pm 0.39) \times 10^{-2} \text{ kbar}^{-1}.$$

The intercept of  $m^*$  versus  $P$  graph corresponds to a standard atmospheric pressure mass of  $(0.0635 \pm 0.0006)m_0$ . The cyclotron effective mass at standard atmospheric pressure was estimated before applying pressure and after removal of pressure. The measured values were  $(0.0635 \pm 0.0002)m_0$  and  $(0.0641 \pm 0.0009)m_0$ . An average of these two values along with the intercept at  $P = 1$  bar yielded

$$m^* = (0.0637 \pm 0.0006)m_0.$$

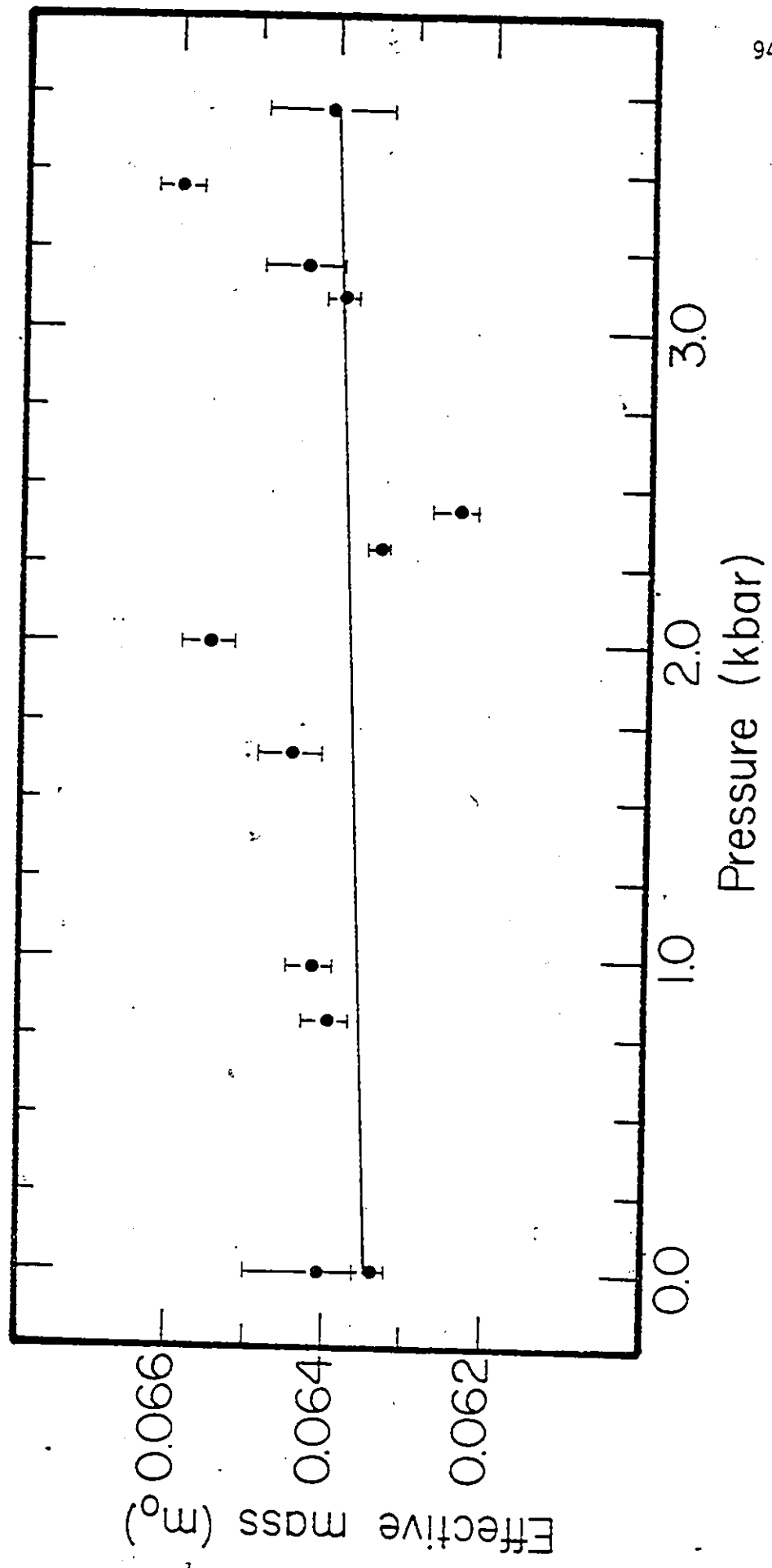
Figure 6-13 Logarithmic plots for the determination of the cyclotron effective mass associated with the principal hole branch in the trigonal-bisectrix crystallographic plane at pressures of; a) 1 bar, b) 1.65 kbar, and c) 3.2 kbar. The solid lines are the least squares sinh fits to the experimental data points of  $\ln(A/T)$  versus temperature, T, at a magnetic field of 1 Tesla.



U

C

Figure 6-14. A plot of the cyclotron effective mass ( $m^*/m_0$ ) associated with the minimum cross-sectional area of the principal hole branch in the trigonal-bisectrix crystallographic plane versus pressure up to 3.7 kbar. The line is a least squares linear fit.



## CHAPTER 7

### DISCUSSION: PRESSURE DEPENDENCE OF THE HOLE FERMI SURFACE AND CYCLOTRON EFFECTIVE MASS OF ANTIMONY

#### 1. Pressure dependence of the hole Fermi surface anisotropy and shape

The response of the hole Fermi surface anisotropy to the influence of hydrostatic pressure can be divided into two regions as follows.

##### i) The pressure region from 1 bar to 2.44 kbar

This region was investigated by determining the anisotropy of  $\Delta F/F(0)$ ,  $\Delta F = F(P) - F(0)$ , at pressures of 1.08 and 2.44 kbar. Figure 6-6 in Chapter 6, indicates that  $\Delta F/F(0)$  is strongly angular dependent. For small cross-sections, i.e. from  $10^\circ \approx 100^\circ$ , the average of  $\Delta F/F(0) = -1.8\%$ , while for large cross-sections, i.e. from  $150^\circ - 180^\circ$ , the average of  $\Delta F/F(0) = +1.2\%$ . The corresponding average logarithmic pressure derivatives,  $(1/F)dF/dP$ , are  $-1.7\% \text{ kbar}^{-1}$  and  $1.1\% \text{ kbar}^{-1}$ , respectively. The anisotropy of  $\Delta F/F(0)$  at a pressure of 2.44 kbar, figure 6-7, is qualitatively similar, but of different magnitude to that observed at  $P = 1.08 \text{ kbar}$ . The average  $\Delta F/F(0)$  for small ( $10^\circ \approx 100^\circ$ ) and large ( $150^\circ - 180^\circ$ ) sections for a pressure of 2.44 kbar is  $-2.5\%$  and  $+0.9\%$ , respectively. The corresponding average logarithmic pressure derivatives,  $(1/F)dF/dP$ , are  $-1\% \text{ kbar}^{-1}$  and  $+0.9\% \text{ kbar}^{-1}$ , respectively. The significant change with magnetic field direction in the magnitude and sign of the pressure derivatives suggests that the surface changes anisotropy and shape under pressure; It elongates along and near its maximum prin-

principal axis and shrinks along and near its minimum principal axis in this pressure region.

It is of interest to investigate to what extent the shape of the hole Fermi surface changes with pressure. This was done by explicitly determining the deviation of the surface from an ellipsoidal shape (which is a reasonable approximation to the actual shape) at standard atmospheric pressure and at a pressure of 1.08 kbar. These calculations were made on the basis of an ellipsoidal model using the formula

$$F(\theta) = (A \cos^2 \theta + B)^{-3/2} \quad (7.1)$$

where  $\theta$  is measured from the principal axis (Windmiller, 1966). The present experimental results for  $P = 1.08$  kbar and for standard atmospheric pressure were used to determine the origin of  $\theta$  and the parameters  $A$  and  $B$ . The origin of the angular orientation,  $\theta$ , and the value of  $(A+B)$  were calculated from the direction and magnitude of the minimum frequency of the hole branch, respectively. The parameter  $B$  was deduced from the magnitude of the maximum frequency. Fits of equation (7.1) to the data for standard atmospheric pressure and a pressure of 1.08 kbar can be expressed as

$$F(\theta) = (239.9 \cos^2 \theta + 26.19)^{-3/2} \times 10^4 \quad \text{at } P = 1 \text{ bar} \quad (7.2)$$

$$F(\theta) = (234.9 \cos^2 \theta + 26.33)^{-3/2} \times 10^4 \quad \text{at } P = 1.08 \text{ kbar} \quad (7.3)$$

In figure 7-1 is plotted the angular dependence of the deviation of the shape of the hole surface from a perfect ellipsoid at pressures of 1 bar and 1.08 kbar in the trigonal-bisectrix crystallographic plane. The

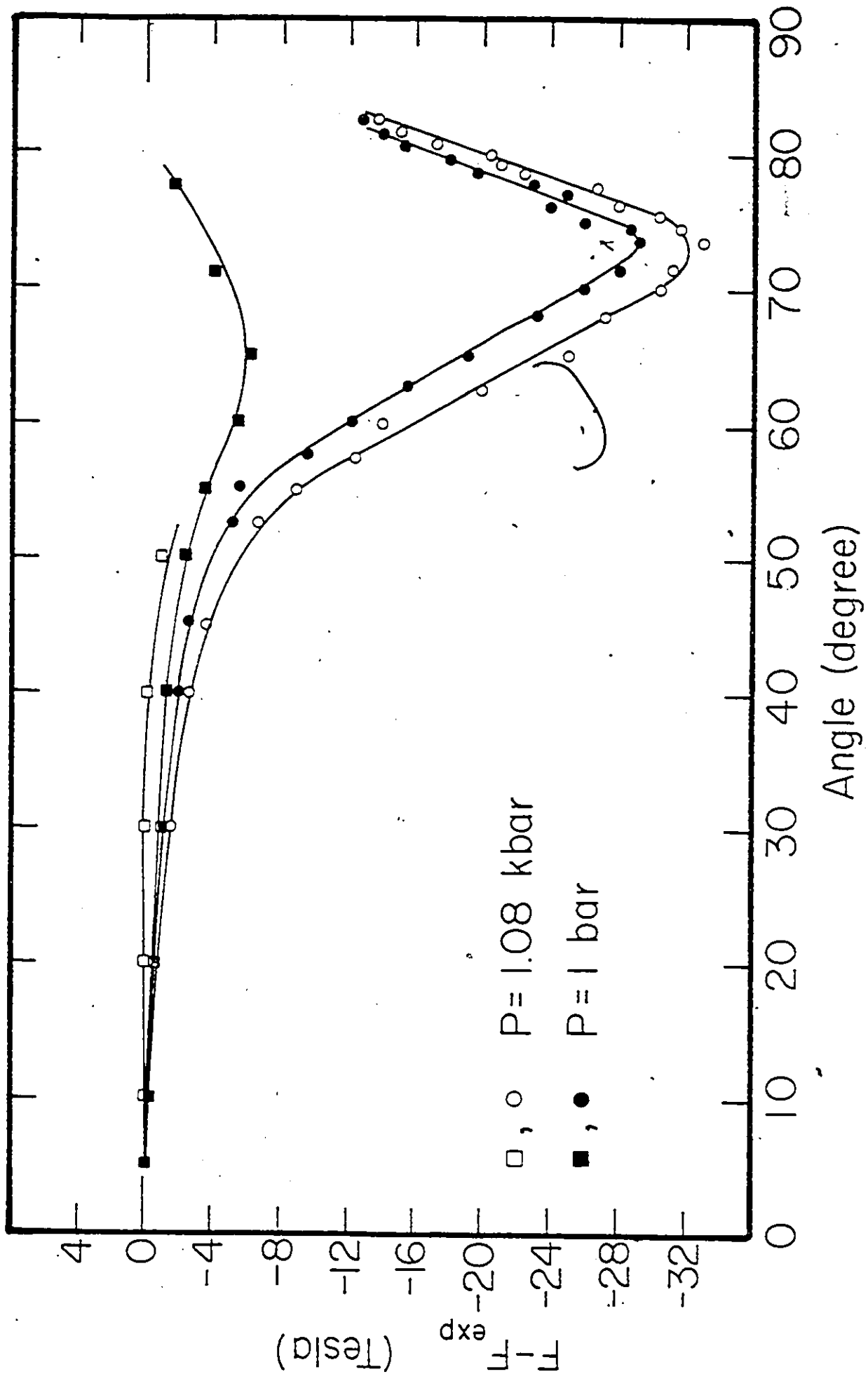
deviation  $F(\theta) - F_{\text{exp}}(\theta)$ , is the difference between the calculated frequency  $F(\theta)$  based on the ellipsoidal model, and the observed frequency  $F_{\text{exp}}(\theta)$ . It should be noted that in figure 7-1, the angle  $\theta$  is measured from the minimum section of the hole surface.

The total deviation from an ellipsoidal shape at standard atmospheric pressure and a pressure of 1.08 kbar was determined to be 8% and 9%, respectively. Based on this, it can be stated that the hole surface in the trigonal bisectrix plane changes shape and deviates even more from an ellipsoidal shape under pressure. The calculated increase in the total deviation from an ellipsoidal shape also suggests the possibility that the tilt angle of the maximum section of the hole Fermi surface is shifted slightly under pressure. However, experimentally we were not able to single out this shift, since the de Haas-van Alphen oscillation beyond the direction of the maximum section at a pressure of 1 bar, i.e.  $150^\circ$  from the trigonal axis, could not be observed for the reason mentioned in the previous chapter. Brandt *et al* (1978) have reported a change in the direction of the maximum frequency of the Shubnikov-de Haas oscillations of the hole branch in the trigonal-bisectrix plane in the pressure region from 5 - 14 kbar.

The particular choice of the experimental data obtained at a pressure of 1.08 kbar to be used in the calculations explained above was made for the following reasons. Firstly, both the minimum and maximum frequencies of the branch were experimentally accessible. Secondly, the alignment of the crystal did not change appreciably at this pressure (see figure 6-10). This minimized the error in calculating the para-



Figure 7-1 Influence of pressure of 1.08 kbar on the deviation of the observed frequencies of the principal hole branch from an ellipsoidal model in the trigonal-bisectrix plane. The deviation  $F - F_{\text{exp}}$  is plotted versus angle at a pressure of 1 bar ( $\bullet, \blacksquare$ ) and a pressure of 1.08 kbar ( $\circ, \square$ ).  $\bullet$  and  $\circ$  refer to the angular region from  $52.5^\circ$  (minimum frequency direction) -  $0^\circ$  (trigonal direction) -  $148.5^\circ$ , while  $\blacksquare$  and  $\square$  refer to the angular region from  $52.5^\circ$  -  $90^\circ$  (bisectrix direction) -  $148.5^\circ$  of the hole branch. The direction of the minimum section ( $52.5^\circ$ ) is taken to be the origin of angle.



meters A and B and simultaneously overcame any possible conflict in describing the response of the shape to pressure. This is of critical importance since the effect of pressure of 1.08 kbar is expected to be small and comparable to the systematic error which could be caused by slight crystal misorientation.

It is quite clear from the foregoing discussion, and also from the previous studies made on the Fermi surface of antimony (see for example Brandt, 1967) that the energy dispersion of the hole Fermi surface deviates from the ellipsoidal-parabolic nature. The ellipsoidal-parabolic approximation can only be considered as a first approximation to the actual Fermi surface. This model presents simple analytic expressions for the constant-energy surface which enables one to determine in a clear and simple way a variety of general features such as the carrier concentration, and the shift in the Fermi energy due to the application of pressure. According to this model, the cyclotron effective mass is energy independent, and the energy is a quadratic function of wave vector. In the principal axis system of the ellipsoid, it is expressed as

$$E(\vec{k}) = \frac{\hbar^2 k_1^2}{m_1} + \frac{\hbar^2 k_2^2}{m_2} + \frac{\hbar^2 k_3^2}{m_3} \quad (7.4)$$

$E$  is the Fermi energy,  $k_{1,2,3}$  are the wave vector components along the major (1,2) and minor (3) axes of the ellipsoidal and  $m_1, m_2$  and  $m_3$  are the energy independent components of mass tensor along the principal axes. Also, based on this model, the ratios of the extremal cross-sectional areas of the ellipsoid to their associated cyclotron effective mass,

$S(\theta)/m^*(\theta)$ , are equal for all crystallographic orientations. Thus any departure from equality specifies the extent of any deviation from a parabolic nature.

The availability of precise experimental information on the magnitude of the cyclotron effective mass (Datars and Vanderkooy, 1964) along with the present results of the extremal frequencies of the hole Fermi surface permitted us to estimate the quantity  $(\hbar^2 S/2\pi m^*)$  along the crystal axes (trigonal, bisectrix and binary) and the principal axes of the ellipsoid (1, 2 and 3); 1, 2 and 3 refer to the principal axis parallel to the crystal axis of the two-fold symmetry (binary-axis), the principal axis parallel to the maximum section of the branch in the trigonal-bisectrix plane which is tilted  $150^\circ$  from the trigonal-axis and the principal axis parallel to the minimum section of the surface which is tilted  $52.5^\circ$  from the trigonal-axis in the same crystallographic plane, respectively. Table 7-1 presents our calculated values of  $\hbar^2 S/2\pi m^*$ . As can be seen, the maximum departure from equality occurs at axis 2. The largest percentage deviation was determined to be 37%. When experimental values of the anisotropy of  $m^*$  as a function of pressure become available it will be possible to make judgements about the changes (if any) in the energy dispersion,  $E(\vec{k})$ , in relation with pressure.

ii) The pressure region from 3 to 4.2 kbar

The experimental data shown in figures 6-8 and 6-9 describe the anisotropy of  $\Delta F/F(0)$  at pressures of 3.15 and 3.56 kbar and 3.89 and 4.19 kbar, respectively. The data presented in Figure 6-8 indicate that

Table 7-1

Calculated values <sup>(1)</sup> of  $(\hbar^2 S/2\pi m^*)$ 

Crystal and ellipsoidal axes	$S$ in $10^{13}$ $\text{cm}^{-2}$	$(m^*/m_0)$	$(\hbar^2 S/2\pi m^*)$ in $10^{-2}$ eV Present work	$(\hbar^2 S/2\pi m^*)$ in $10^{-3}$ eV Brandt et al (1967) <sup>(2)</sup>
Trigonal-axis	$(9.17 \pm 0.05)$	$(0.10 \pm 0.01)$	$(11.1 \pm 1.2)$	
Bisectrix-axis	$(7.88 \pm 0.03)$	$(0.075 \pm 0.010)$	$(12.4 \pm 1.6)$	
Binary-axis (Axis 1)	$(20.59 \pm 0.07)$ <sup>(3)</sup>	$(0.215 \pm 0.010)$	$(11.6 \pm 0.6)$	11.7
Axis 2	$(18.7 \pm 0.2)$	$(0.25 \pm 0.01)$	$(9.1 \pm 0.5)$	} 9.06
Axis 3	$(5.90 \pm 0.01)$	$(0.062 \pm 0.010)$	$(11.5 \pm 1.9)$	
		$(0.0637 \pm 0.0005)$ <sup>(4)</sup>	$(11.2 \pm 0.1)$	

(1) All tabulated values of  $S$  and  $(m^*/m_0)$  were measured at standard atmospheric pressure. The extremal area  $S$  is related to the de Haas-van Alphen frequency,  $F$ , according to  $S = \frac{2\pi}{4} \frac{e}{hc} F$  where  $F$  is in Gauss.

(2)  $\hbar^2 S/2\pi m^*$  quoted in this column were calculated from the values of  $S$  and  $(m^*/m_0)$  tabulated by Brandt et al (1967).

(3) This value was estimated from the de Haas-van Alphen frequency measured by Windmiller (1966).

(4) This is our present measured de Haas-van Alphen cyclotron effective mass. The full expression for the de Haas-van Alphen amplitude as a function of temperature was used to determine  $m^*/m_0$  accurately.

all extremal sections of the hole Fermi surface decrease with increasing pressure, except at the trigonal axis, and the relative decrease of the small sections ( $10^\circ \approx 100^\circ$ ) is higher than for the large sections ( $160^\circ - 180^\circ$ ). The averages of  $\Delta F/F(0)$  and  $(1/F)dF/dP$  in the angular region from  $10^\circ \approx 100^\circ$  were estimated to be  $-2.8\%$  and  $-0.9\% \text{ kbar}^{-1}$ , respectively. Thus, the rate of decrease of  $\Delta F/F(0)$  for these small sections decreases appreciably in comparison with its rate at lower pressure, particularly at the smallest cross-sectional area of the branch. On the other hand, the major change at this particular pressure is the change in the sign of the pressure derivative of the large sections ( $160^\circ - 177^\circ$ ). To our present knowledge this is the first observation of a change in sign of the pressure derivatives of the large sections in this angular region. For these large sections, the average  $\Delta F/F(0)$  along with  $(1/F)dF/dP$  are estimated to be  $-2.1\%$  and  $-0.7\% \text{ kbar}^{-1}$  respectively.

Figure 6-9 shows the angular dependence of  $\Delta F/F(0)$  at pressures of 3.89 and 4.19 kbar. At  $P = 3.89$  kbar, all indicated extremal sections of the branch continue to decrease, while at  $P = 4.19$  kbar, all cross-sectional areas of the hole Fermi surface show an apparent tendency to increase with further increase in pressure. Qualitatively, this connects with the high pressure work done by Brandt *et al.* (1978) on the angular dependences of the Shubnikov-de Haas oscillations in the pressure region from 5-11 kbar. Their results indicate that all extremal sections of the branch increase with pressure.

Table 7-2 summarizes the results obtained on the hydrostatic pressure dependence of the hole Fermi surface anisotropy in the trigonal-

bisectrix plane. In no previous measurements has the pressure dependence of the anisotropy of the entire hole Fermi surface been measured specifically in the pressure range covered in the present experiment. However, there exists experimental information on the behaviour of the two cross-sectional areas at the minimum and maximum sections of the branch with pressure. Also, to our present knowledge no theoretical predictions exist for the pressure dependence of the anisotropy of the Fermi surface of pure antimony.

## 2 - Pressure dependence of the minimum frequency

The results of our careful study of the influence of pressure up to 4.5 kbar on the minimum frequency of the hole Fermi surface in the trigonal-bisectrix plane were shown graphically in the previous chapter in figure 6-11. A nonmonotonic change in the frequency with increasing pressure up to 4.5 kbar is clearly evident. It follows from the analysis presented in Chapter 6 of the experimental data in figure 6-11 that the weighted least squares fit to all data points up to 3.89 kbar yields a pressure derivative of  $-(0.91 \pm 0.07) \times 10^{-2} \text{ kbar}^{-1}$ . Because of the observed nonlinear feature, we have determined the weighted least squares linear fits to the data points up to 1.67 and 3.15 kbar. This was done in order to make a consistent comparison with the results of other investigators in different pressure regions. This analysis yielded pressure derivatives of  $-(0.72 \pm 0.04) \times 10^{-2} \text{ kbar}^{-1}$  and  $-(0.84 \pm 0.07) \times 10^{-2} \text{ kbar}^{-1}$  at 1.67 and 3.15 kbar; respectively. Also, it is apparent from figure 6-11 that the pressure derivative reaches its

Table 7-2

Summary of results of the pressure dependence of the anisotropy of the hole Fermi surface in the trigonal-bisectrix plane of antimony.

Pressure (kbar)	Minimum frequency direction	Maximum frequency direction	Trigonal axis	Bisectrix axis	Average $\Delta F/F(0)$ in the angular region from $10^0 - 100^0$ in $10^{-2}$	Average $\Delta F/F(0)$ in the angular region from $160^0 - 180^0$ in $10^{-2}$
1.08	$-(0.807 \pm 0.004)$	$+(0.260 \pm 0.005)$	$+(0.68 \pm 0.01)$	$-(3.24 \pm 0.07)$	-1.8	+1.2(1)
2.44	$-(2.199 \pm 0.004)$	-	$+(1.78 \pm 0.04)$	$-(3.42 \pm 0.08)$	-2.5	+0.9
3.15	$-(2.553 \pm 0.004)$	-	$+(0.70 \pm 0.01)$	$-(3.40 \pm 0.07)$	-2.8	-2.1
3.56	$-(3.162 \pm 0.004)$	-	$-(1.07 \pm 0.02)$	-	-3.6(2)	-
3.89	$-(3.682 \pm 0.004)$	-	$-(2.60 \pm 0.05)$	$-(5.06 \pm 0.11)$	-5.2	-4.5
4.19	$-(3.086 \pm 0.004)$	-	$-(0.67 \pm 0.01)$	-	-3.7(3)	-2.5
4.30	$-(1.871 \pm 0.004)$	-	-	-	-	-

(1) This average corresponds to the angular region from  $150^0 - 180^0$ .

(2 and 3) These averages correspond to the angular region from  $0^0 - 52.5^0$ . Angles are measured in the sense of rotation from  $\Gamma T$  to  $\Gamma X$  as in figure 6-6.



lowest value at  $(3.7 \pm 0.3)$  kbar and then the frequency starts to increase fairly rapidly with pressure. An extrapolation of the data points obtained at pressures greater than 3.89 kbar indicates that the frequency approaches its initial standard atmospheric pressure value at a pressure of approximately 5kbar.

Table 7-3 presents a comparison of the experimental values of the pressure derivatives of the minimum frequency obtained by various authors using different methods. Schirber and O'Sullivan (1969), studied the hydrostatic pressure dependence of the minimum section in the trigonal-bisectrix plane by means of the de Haas-van Alphen effect. They determined  $(1/F)dF/dP$  to be  $-(0.30 \pm 0.15) \times 10^{-2} \text{ kbar}^{-1}$ , in solid helium up to 3 kbar and  $-(0.6 \pm 0.2) \times 10^{-2} \text{ kbar}^{-1}$  in fluid helium up to 24 bars using the phase shift technique. The figure obtained using the solid helium technique does not agree with our measured value in the same pressure range. The difference is significantly larger than the quoted experimental error associated with either measurement. On the other hand their measured value using the phase shift method is in good agreement with our estimated pressure derivative at 1.67 kbar. The nonmonotonic feature of the pressure dependence of the frequency along with the change of sign of the pressure derivative were first observed by Schirber and O'Sullivan (1970). They reported that the minimum section returns to its initial value at approximately 5 kbars, and continues to increase with further increase in pressure at a rate  $(1/F)dF/dP \approx 1\%$ . This is consistent with the present measurements. However, our results, whether for the magnitude of the pressure derivative or for the shape of the

frequency versus pressure, are specified with significantly improved precision.

Tanuma et al (1970) reported an experimental study of the pressure dependence of the de Haas-van Alphen oscillations associated with the minimum section of the hole Fermi surface using a mixture of kerosene and oil as a pressure transmitting medium. They reported a continuous decrease in the frequency with increasing pressure up to 6 kbar at a rate  $(1/F)dF/dP = -0.82 \times 10^{-2} \text{ kbar}^{-1}$ . The rate of decrease they reported is in agreement with our measurements up to 3.89 kbar. However, we see discrepancy at pressures greater than 4 kbar in which they showed 0.82% decrease and we have observed a definite increase with increasing pressure.

Brandt et al (1978) studied the influence of hydrostatic pressure on the Fermi surface of pure antimony using the kerosene-oil method in the pressure range from 5 - 14 kbar by means of the Shubnikov-de Haas effect. They reported that the minimum section of the hole Fermi surface passes through its zero pressure value at 5 kbars and increases linearly with pressure up to 14 kbars at a rate  $(1/F)dF/dP = +(1.0 \pm 0.15) \times 10^{-2} \text{ kbar}^{-1}$ . This rate of increase is in reasonable agreement with extrapolation of our measurements. The measurements made by Brandt et al (1978) supported an investigation made by Minina and Lavrova (1969) on the pres-

Table 7-3

Comparison of the reported values of the pressure derivatives  $1/F(dF/dP)$  of the minimum cross-sectional area of the hole Fermi surface in the trigonal-bisectrix plane of pure antimony.

$1/F(dF/dP)$ in $10^{-2}$ kbar $^{-1}$	Pressure Range	Investigator
$-(0.6 \pm 0.2)$	0 - 25 bar	Schirber and O'Sullivan (1969)
$-(0.30 \pm 0.15)$	0 - 3 kbar	Schirber and O'Sullivan (1969)
$+ \approx 1$	5 - 8 kbar	Schirber and O'Sullivan (1970)
$+ 0.7$	9 - 14 kbar	Minina <u>et al</u> (1969)
$- 0.82$	0 - 6 kbar	Tanuma <u>et al</u> (1970)
$+(1.0 \pm 0.15)$	5 - 14 kbar	Brandt <u>et al</u> (1978)
$-(0.91 \pm 0.07)$	0.389 kbar	Present work
$-(0.72 \pm 0.05)$	0-1.67 kbar	Present work
$-(0.84 \pm 0.07)$	0-3.15 kbar	Present work
Positive	3.9 - 4. kbar	Present work

sure dependence (9-14 kbar) of the Shubnikov-de Haas oscillations of the minimum section using the same pressure technique.

We now turn to our measurements on the pressure dependence of the tilt angle of the minimum section of the hole Fermi surface which is presented in the previous chapter in figure 6-10. The present measured tilt angle ( $52.5 \pm 1.0$ ) is in excellent agreement with the atmospheric pressure results of both Windmiller (1966) and Herrod et al (1971) within combined experimental error. It is evident from this figure that the tilt angle does not change appreciably with pressure within our quoted experimental error,  $< \pm 1^\circ$ . Experimentally this agrees well with both low and high pressure investigations made by Schirber and O'Sullivan (1970) and Brandt et al (1978), who reported no significant change in the tilt angle with pressure up to 8 and 14 kbar, respectively. On the other hand, a computer analysis based on the relaxation time approximation of the pressure dependence of the galvanomagnetic coefficients up to 10 kbar, carried out by Kechin (1968) indicates a change in the tilt angle of  $\approx -3\%$  and  $-5\%$  measured in the sense from  $\Gamma T$  towards  $\Gamma X$  at pressures of 4 and 10 kbar, respectively. Such change is large enough to be detected easily from our rotation diagrams, since our angular sensitivity is good enough to detect a change much less than their prediction. Thus, the prediction of Kechin is not confirmed by our measurements.

We have calculated the hole Fermi energy,  $E_F^h$ , as a function of pressure by employing the ellipsoidal-parabolic model and by using experimentally determined pressure dependences of the cyclotron effective mass and the de Haas-van Alphen frequency at the minimum of the hole

branch. However, based on the illustration made in the previous section, it is obvious that the use of the ellipsoidal-parabolic model will give only approximate values. In this model the Fermi energy,  $E_F$ , is related to the cyclotron effective mass,  $m^*$ , and the de Haas-van Alphen frequency,  $F$ , by

$$E_F = \frac{e\hbar}{m^*C} F \quad (7.5)$$

Since the cyclotron effective mass is almost insensitive to pressure (see Figure 6-14), the change of  $E_F^h$  with pressure is mainly influenced by the pressure dependence of the de Haas-van Alphen frequency in the pressure region investigated. Table 7-4 shows the calculated pressure dependence of the hole Fermi energy up to approximately 4 kbar. The weighted least squares fit to  $E_F^h$  as a function of pressure up to 3.89 kbar yields

$$\frac{dE_F^h}{dP} = -(1.02 \pm 0.08) \text{ meV.kbar}^{-1} \quad (7.6)$$

### 3. Pressure dependence of the cyclotron effective mass

A comparison of experimental and calculated values of the cyclotron effective mass at standard atmospheric pressure, determined by various investigators using different methods, is presented in table 7-5. Values by Brandt et al (1966), Windmiller (1966), Dunsworth and Datars (1973), and Altounian and Datars (1975), were derived from the temperature dependence of the de Haas-van Alphen effect. The effective mass determined from the measurement of the cyclotron resonance frequency was obtained by Datars and Vanderkooy (1964). The theoretical value of  $m^*/m_0$  was estimated by Pospelov and Grachev (1983), who carried out a calculation

Table 7-4

Calculated values of the pressure dependence of the hole Fermi energy,  $E_F^h$ , based on the ellipsoidal-parabolic approximation.

Pressure (kbar)	Frequency (Tesla)	$(m^*/m_0)$	Hole Fermi energy, $E_F^h$ , (MeV)
0.0	(61.9±0.1)	(0.064±0.0005) (2)	(111.7±0.9)
	(61.3±0.1) (1)		(110.5±0.8)
1.08	(61.4±0.1)		(110.8±0.9)
1.67	(61.2±0.1)		(110.5±0.9)
2.44	(60.5±0.2)		(109.3±1.0)
2.95	(60.0±0.2)		(108.4±1.0)
3.15	(60.3±0.1)		(108.9±0.9)
3.56	(59.9±0.2)		(108.2±0.9)
3.89	(59.6±0.1)		(107.6±0.9)
4.19	(60.3±0.3)		(108.3±0.9)
4.31	(60.7±0.1)		(109.6±0.8)

(1) This value is measured by Windmiller(1966). Experimental technique: de Haas-van Alphen effect.

(2) This is an average value of the present measured cyclotron effective mass over the pressure region investigated.

Table 7-5

Reported values of the calculated and experimental cyclotron effective mass associated with the minimum section of the hole Fermi surface of pure antimony in the trigonal-bisectrix plane at standard atmospheric pressure.

	$m^*/m_0$	Investigator
Calculation	0.06	Pospelov and Grachev (1983)
Experiment	$0.062 \pm 0.01$	Datars and Vanderkooy (1964)
	0.058	Brandt <u>et al.</u> (1966)
	$0.069 \pm 0.002$	Windmiller (1966)
	0.063	Dunsworth and Datars (1973)
	0.063	Altounian and Datars (1975)
	$0.0637 \pm 0.0005$	Present work

of cyclotron masses in antimony using the pseudopotential scheme of Falicov and Lin (1966), which does not take into account explicitly many-body effects.

Our present result is in good agreement with other measurements within combined experimental errors, wherever they are quoted, except for the value reported by Windmiller. The difference between our estimated value and Windmiller's result is significantly outside combined experimental error. He used the first approximation of the expression of the de Haas-van Alphen amplitude as a function of temperature. The mass was deduced from the logarithmic fit of the de Haas-van Alphen amplitude versus temperature. A least squares fit of the present experimental data points of a plot of  $\ln(A/T)$  against  $T$  yields  $m^* = (0.069 \pm 0.001)m_0$  which is in agreement with Windmiller's value. Thus, the discrepancy is due to his use of the first approximation.

The pressure dependence of  $m^*$  associated with the minimum section of the hole Fermi surface was studied by Brandt et al (1978) using the Shubnikov-de Haas effect. In their work, the temperature dependence of the oscillation amplitude was measured only at temperatures of 4.2K and 2.1K. From these two measurements  $m^*$  was deduced. Their tabulated data of  $m^*$  versus pressure showed rather poor precision in comparison with the precision achieved in the present measurements. At pressures of 0.4 kbar and 4.5 kbar, they reported  $m^*$  to be  $(0.075 \pm 0.004)m_0$  and  $(0.081 \pm 0.006)m_0$ , respectively. This indicated that  $dm^*/dP = + (1.9 \pm 3.3) \times 10^{-2} m_0 \cdot \text{kbar}^{-1}$ , which is approximately two orders of magnitude larger than the value obtained in the present experiment.



There is no pressure dependence of cyclotron mass in the ellipsoidal-parabolic model. The next available model which has a pressure dependence of the cyclotron effective mass is the ellipsoidal-nonparabolic model proposed by Kane (1957). For this model, the energy dispersion relation has the form

$$\frac{\pi^2 k_1^2}{m_1} + \frac{\pi^2 k_2^2}{m_2} + \frac{\pi^2 k_3^2}{m_3} = E + \frac{E^2}{E_g} \quad (7.7)$$

where 1, 2 and 3 refer to the principal axes of the ellipsoid and the  $m_i$ 's are the band-edge effective mass components along the principal axes. The surfaces of constant energy for this model are still ellipsoidal, but the energy dependence is modified by the term  $E^2/E_g$ .  $E_g$  is the energy gap separating this band from another band near it. The non-parabolic energy surface leads to the energy dependence of the cyclotron effective mass,  $m^*$ . The cyclotron mass for an orbit in the trigonal-bisectrix plane is given by

$$m^* = m_b (1 + 2E/E_g) \quad (7.8)$$

where  $m_b$  is the band-edge mass in units of free electron mass. The extremal cross-sectional area is

$$S = \frac{2\pi}{h^2} m_b (1 + E/E_g) E \quad (7.9)$$

Equations (7.8) and (7.9) can be combined to give

$$m^{*2} = m_b^2 + (4/\pi)(m_b/E_g)S \quad (7.10)$$

Since  $S$  is directly proportional to the de Haas-van Alphen frequency,  $F$ , therefore

$$m^{*2} = m_b^2 + 0.46(m_b/E_g)F \quad (7.11)$$

where  $F$  is in units of Tesla, and  $E_g$  is in meV. The validity of this equation was tested by Dunsworth and Datars (1973), and Altounian and Datars (1975). They interpreted their experimental results for the cyclotron effective mass as a function of the de Haas-van Alphen frequency in tin and tellurium doped antimony in terms of the nonparabolic, but ellipsoidal energy surface. Their results lend support to equation (7.11) and permitted them to deduce the parameter  $E_g/m_b$ . They obtained  $E_g/m_b = 7.3$  and 7.1 eV for antimony-tin and antimony-tellurium alloys, respectively for the minimum section of the hole Fermi surface. The average value for the two alloys will be used in the following analysis.

Now we test the extent of the validity of equation (7.11) as a function of pressure. If we assume, for a moment at least in the pressure region investigated, that the parameters  $m_b$  and  $m_b/E_g$  are insensitive to pressure, the derivative of equation (7.11) with respect to pressure yields

$$\frac{dm^*}{dP} = (0.23/m^*)(m_b/E_g) \frac{dF}{dP} \quad (7.12)$$

On the basis of Dunsworth (1973) and Altounian's (1975) average value of  $E_g/m_b = 7.2$  eV, and the present experimental values of  $dF/dP = -(0.56 \pm 0.04)$  Tesla.kbar<sup>-1</sup> and  $m^* = (0.0637 \pm 0.0005)m_b$ , it follows from equation (7.12) that,

$$\frac{dm^*}{dP} = - (0.28 \pm 0.02) \times 10^{-3} m_0 \cdot \text{kbar}^{-1} \quad (7.13)$$

It should be noted that the estimated uncertainty in the calculated value of  $dm^*/dP$  come from approximately 7% and 0.8% errors in the measured values of  $dF/dP$  and  $m^*$ . This calculated value predicts a small change in  $m^*$  with pressure which cannot be distinguished because of the scatter of the data points in figure 6-14. Thus, the observed value of  $dm^*/dP$  of  $(0.1 \pm 0.2) \times 10^{-3} m_0 \cdot \text{kbar}^{-1}$  is in reasonable agreement with the predicted value.

Finally, it is interesting to compare the pressure dependence of  $m^*$  for antimony to that obtained for potassium. For potassium, we have seen that the contribution to the mass from the electron-phonon interaction has the dominant influence on the magnitude of the mass enhancement. This is in contrast with antimony, where the electron-phonon interaction is expected to be negligible. In fact the measured  $m^*$  at standard atmospheric pressure,  $(0.0637 \pm 0.0005) m_0$ , is only a few percent ( $\approx 6\%$ ) larger than the calculated band structure mass,  $0.06 m_0$ , (Pospelov and Grachev 1983). The experimentally determined logarithmic pressure derivative of the cyclotron mass,  $(1/m^*)dm^*/dP$ , for potassium was found to be  $-(0.71 \pm 0.15) \times 10^{-2} m_0 \cdot \text{kbar}^{-1}$ , which is approximately five times larger than the value for antimony. The theoretical analysis made in connection with the pressure dependence of  $m^*$  for potassium showed that the observed decrease of  $m^*$  with increasing pressure is mainly affected by the pressure dependence of the electron-phonon interaction and the

pressure dependence of the band structure mass and the electron-electron renormalization are insignificant. In contrast and on the basis of this analysis, a small enhancement of  $m^*$  with pressure is expected to be seen in antimony, that is the pressure derivative of  $m^*$  should be influenced by just the band structure effect. In fact, the present measurements confirmed this view. Thus, investigating the effect of pressure on the cyclotron effective mass of antimony helped naturally to exclude the contribution from the electron-phonon interaction and to identify separately the pressure dependence of the band structure mass which turns out to be nearly insensitive to pressure as predicted from band theory.

## CHAPTER 8

### CONCLUSIONS

Detailed investigations of the hydrostatic pressure dependence of the de Haas-van Alphen effect in potassium and antimony were carried out using the helium freezing method up to 4.4 kbar. These measurements were made using the field modulation measuring technique at magnetic fields of up to 5.54 Tesla in potassium and 1.9 Tesla in antimony and at temperatures between 1.2 and 2.2 K in potassium and 1.2 and 4.2 K in antimony.

The temperature dependence of the dHvA oscillation amplitude was used to determine the cyclotron effective mass,  $m^*$ , in potassium. The logarithmic pressure derivative of the cyclotron effective mass was found to be  $-(0.71 \pm 12) \times 10^{-2} \text{ kbar}^{-1}$  with a standard atmospheric pressure effective mass of  $(1.211 \pm 0.005)m_0$ . The observed enhancement of  $m^*$  with pressure was explained and analyzed by calculating the pressure dependence of the electron-phonon mass renormalization parameter,  $\lambda_{ep}$ , which is expected to be the dominant term responsible for the mass enhancement in a simple metal such as potassium. These calculations were made on the basis of a theory proposed by Trofimenkoff and Carbotte (1970). According to their theory,  $\lambda_{ep}$  is related to the Grüneisen parameter,  $\gamma_G$ , and the volume change,  $\Delta V/V$  with pressure through equation (5.7). The pressure dependence of  $\gamma_G$  and the change of volume with pressure were determined from recent experimental studies made by Boehler (1983) and

Anderson and Swensen (1983), respectively. On the basis of this analysis, the calculated logarithmic pressure derivative of the electron-phonon mass renormalization parameter,  $(T/m_{ep})dm_{ep}/dP$ , was found to be  $-0.62 \times 10^{-2} \text{ kbar}^{-1}$  in good agreement with the measured logarithmic pressure derivative of  $m^*$  within quoted experimental uncertainty. This suggested that the pressure dependence of the electron quasiparticle mass is significantly influenced by the pressure dependence of the electron-phonon mass renormalization parameter. Simultaneously, this analysis confirmed that the changes of the band structure mass and the electron-electron mass enhancement parameter with pressure are small and are of negative sign. This is the first reported measurement of this pressure dependence and provides experimental evidence for the electron-phonon mass enhancement and its response to hydrostatic pressure (Abd El-Rahman et al 1985).

A separate experimental identification of the pressure dependence of the band structure mass was made possible by studying the influence of hydrostatic pressure on the cyclotron effective mass of antimony. The many-body effects are expected to be insignificant in antimony, and on the basis of band theory the band structure mass is expected to be insensitive to pressure. The present measurements of the hydrostatic pressure dependence of  $m^*$  and its magnitude at standard atmospheric pressure confirmed this view. The observed difference between the measured  $m^*$  at pressure of 1 bar,  $(0.0637 \pm 0.0006)m_0$ , and the calculated band structure mass (Pospelov and Grachev 1983) was found to be less than 6%, indicating small many-body effects in comparison with that found in simple metals such as potassium. It should be noted however, that if the error in the

calculated value could be taken into account the observed difference of 6% might become less significant. The logarithmic pressure derivative of  $m^*$  was found to be  $+(0.16 \pm 0.39) \times 10^{-2} \text{ kbar}^{-1}$  indicating a very small change with pressure as predicted from band theory, and provides evidence for the insignificance of the electron-phonon many-body interactions in antimony.

The field modulation technique modified to optimize the selectivity and sensitivity of the dHvA spectrometer was successfully applied and used to study the effect of pressure on the hole Fermi surface of antimony. It was shown that the dominant oscillatory component can be eliminated by a proper choice of modulation angle allowing the observation of weaker signals. A second oscillatory component can be rejected by arranging to have the axis of the detection coil lie in the plane perpendicular to the undesired oscillatory component. The use of these spectrometer techniques provided a good quality single dHvA oscillation resulting in no ambiguity or complication in the analysis.

The pressure dependence of the anisotropy of the entire hole branch in the trigonal-bisectrix plane was determined specifically up to 4.2 kbar. These measurements showed that the rates of change of the extremal frequencies,  $\Delta F/F(0)$ , of the entire hole branch with pressure are strongly angular dependent. In the pressure region from 1 bar to 2.44 kbar, the pressure derivatives of the extremal frequencies were found to differ in sign and magnitude for different field directions. In the pressure region from 3-4 kbar, all extremal frequencies decreased below their values at standard atmospheric pressure. The effect

of pressure on the shape of the hole Fermi surface was determined through accurately calculating the departure of the surface from an ellipsoid using the ellipsoidal-parabolic approximation at standard atmospheric pressure and at a pressure of 1.08 kbar. The total deviation was calculated to be 8% and 9%, respectively. Based on these observations it can be asserted that the anisotropy and shape of the hole Fermi surface in the trigonal-bisectrix plane is greatly influenced by pressure.

The pressure dependence up to 4.3 kbar of the minimum frequency of the hole Fermi surface was found to decrease with increasing pressure in a nonlinear fashion up to 3.89 kbar at an average rate  $(1/F)dF/dP = (0.91 \pm 0.07) \times 10^{-2} \text{ kbar}^{-1}$ . The pressure derivative of the frequency reaches its minimum value at  $(3.7 \pm 0.3) \text{ kbar}$  and then changes sign with further increase in pressure. For pressures up to 4.3 kbar the tilt angle of the hole Fermi surface was found to be insensitive to pressure within quoted experimental error. This result agrees with previous experimental investigations devoted to the oscillatory properties of antimony under pressures of up to 14 kbar (see for example Brandt *et al* 1978), but disagrees with the analysis of the galvanomagnetic measurements (Kechin 1968).

The hole Fermi energy was found to decrease with increasing pressure up to 3.89 kbar at a rate of  $dE_F^h/dP = - (1.02 \pm 0.08) \text{ meV.kbar}^{-1}$ . This was calculated on the basis of the ellipsoidal-parabolic model using experimentally measured pressure dependences of the dHVA frequency and the cyclotron effective mass associated with the minimum section of the hole Fermi surface. This model can only be considered as a first



approximation to the actual Fermi surface and so yields just approximate values.

Detailed studies at higher pressures on the specific changes of the anisotropies of the extremal cross-sectional areas of the Fermi surface and their associated cyclotron effective masses with pressure are needed in order to clarify the response of the energy band structure to pressure. These will provide valuable information which might be useful in developing an analytical expression for the energy dispersion relation,  $E(k)$ , and its pressure dependence. The development of such more comprehensive band models is of critical importance in order to explain the effect of pressure on the electronic band structure in antimony.

## REFERENCES

- Abd El-Rahman A A, Elliott M and Datars W R 1985 J. Phys. F: Metal Physics 15 859
- Altounian Z and Datars W R 1980 Can. J. Phys. 58 370
- Altounian Z and Datars W R 1975 Can. J. Phys. 53 459
- Anderson M S and Swenson C A 1983 Phys. Rev. B 28 5395
- Ashcroft N W 1963 Phil. Mag. 8 2055
- Boehler R 1983 Phys. Rev. B 27 6754
- Brandt N B, Bogdanov E V and Minina N Ya 1978 Sov. Phys. Solid State 20 77
- Brandt N B, Minina N Ya and Pospelov Yu A 1969 Sov. Phys. JETP 28 869
- Brandt N B, Minina N Ya and Chen-Kang Chu 1967 Sov. Phys. JETP 24 73
- Cohen M and Blount E I 1960 Phil. Mag. 5 115
- Cracknell A P and Wong K C 1973 The Fermi Surface (Oxford: Clarendon)
- Datars W R and Vanderkooy J 1964 IBM J. Res. Dev. 8 247
- Davis H L, Faulkner J S and Joy H W 1968 Phys. Rev. 167 601
- Dingle R B 1952 Proc. Roy. Soc. (London) A 211 500
- Dresselhaus M S 1970 Proc. Intern. Conf. on Physics of Semimetals and Narrow-Gap Semiconductors (Dallas, Texas) ed. Carter D L and Bate R T pp 3-33
- Dunsworth A E and Datars W R 1973 Phys. Rev. B 7 3435
- Dunifer G L, Mace D A H and Gambles J R 1984 J. Phys. F: Metal Physics (to be published)
- Elliott M and Datars W R 1982 J. Phys. F: Metal Physics 12 465
- Falicov L M and Golin S 1965 Phys. Rev. 137 A871
- Gold A V 1968 Solid State Physics ed. Cochran J F and Breach Vol. 1 pp 39-126

- Grimes C C and Kip A F 1963 Phys. Rev. 21 691
- Harrison W A 1965 Proceedings of the First International Conference on The Physics of Solids at High Pressures (University of Arizona, Tucson, Arizona)
- Herrod R A, Cage C A and Goodrich 1971 Phys. Rev. B 4 1033
- Ishizawa Y 1968 J. Phys. Soc. Japan 25 150
- Jennings L D and Swenson C A 1958 Phys. Rev. 112 31
- Kanè E O 1957 J. Phys. Chem. Solids 1 249
- Kechin V V 1968 Sov. Phys. Solid State 9 2828
- Knecht B 1975 Low Temp. Phys. 21 691
- Landweher G 1969 Physics of Solids in Intense Magnetic Fields ed. Haidemenakis E D
- Leavens C R and Carbotte J P 1973 Can. J. Phys. 57 398
- Leavens C R, MacDonald A H and Taylor R 1983 Phys. Rev. B 27 1352
- Lee M J G 1970 Phys. Rev. B 2 250
- Lee M J G and Falicov L M 1968 Proc. R. Soc. A 304 319
- Lifshitz I M and Kosevich A M 1955 Zh. Eksperim. Theor. Fiz. 29 730 [English translation: Sov. Phys. JETP 2 636 (1956)]
- MacDonald A H, Dharmawardana M W C and Geldart D J W 1980 J. Phys. F: Metal Physics 10 1719
- Martin D L 1970 Can. J. Phys. 48 1327
- Minina N Ya and Lavrova V V 1969 Zh. Eksp. Theor. Fiz. 57 354
- Monfort C E and Swenson C A 1965 J. Phys. Chem. Solids 26 291
- Morosin B and Schirber J E 1969 Phys. Letters A 30 512
- Morosin B and Schirber J E 1972 Solid State Communications 10 249
- Moss J S 1968 Ph.D. Thesis McMaster University
- Onsager L 1952 Phil. Mag. 43 1006

- Paul D McK and Springford M 1978 J. Phys. F: Metal Physics 8 1713
- Pospelov Yu A and Grachev G S 1983 J. Phys. F: Metal Physics 13 1179
- Rakhmanina A V, Venttsel V A, Likhter A I and Rudney A V 1978 Sov. Phys. Solid State 20 1835
- Rice T M 1968 Phys. Rev. 175 858
- Rose J and Schuchardt R 1983 Phys. Status Solidi (Germany) b 117 no. 1 213
- Schirber J E and O'Sullivan W J 1969 Solid State Commun. 7 709
- Schirber J E and O'Sullivan W J 1970 Proc. Intern. Conf. on Physics of Semimetals and Narrow-Gap Semiconductors (Dallas, Texas) ed. Carter D L and Bate R T pp. 57-61, in J. Phys.Chem. Solids 32 Suppl. 1 57 1971
- Schirber J E and Van Dyke J.P 1971 Phys. Rev. Lett. 26 246
- Seiden P E 1969 Phys. Rev. 179 458
- Shoenberg D and Stiles P J 1964 Proc. Roy. Soc. A 281 62
- Shoenberg D 1969 Phys. Kondens. Materie 9 1
- Slavin A J and Datars W R 1974 Can. J. Phys. 52 1622
- Spain I L and Segall S 1971 Cryogenics 11 26
- Stark R W and Windmiller L R 1968 Cryogenics 8 272
- Tanuma S, Minomura S, Fujii G and Datars W R 1970 Proc. Twelfth Intern. Conf. on Low Temperature Physics (Kyoto, Japan), Acad. Press of Japan Tokyo (1970) p. 597
- Tay C Y and Priestley M G Actes. Colloq. Int. No. 188 139
- Templeton I M 1974 Can. J. Phys. 52 1628
- Timbie J P and White R M 1970 Phys. Rev. B 1 2409
- Trofimenkoff P N and Carbotte J P 1970 Phys. Rev. B 1 1136
- Walsh M 1984 (unpublished).

Wilk L, MacDonald A H and Vosko S H 1979 Can. J. Phys. 57 1065

Windmiller L R 1966 Phys. Rev. 149 472

Ziman J M 1972 Principles of the Theory of Solids Second Edition  
(Cambridge University Press, Cambridge)